Spin Polarised Heusler Compounds

Dissertation
zur Erlangung des Grades
"Doktor der Naturwissenschaften"
am Fachbereich Chemie, Pharmazie und Geowissenschaften
der Johannes Gutenberg-Universität Mainz

vorgelegt von
Sabine Wurmehl
geboren in Worms

Mainz, Juli 2006

Contents

1 Introduction.

The Heusler compounds [1] were discovered in 1901. Remarkably, the first one to be reported (Cu_2MnAl) [1], is a ferromagnet made from non ferromagnetic constituents. Heusler compounds are ternary intermetallic X_2YZ-compounds. Most of the Co_2YZ Heusler compounds are predicted to be half-metallic ferromagnets. An example of a Density of States (DOS) of a half-metallic ferromagnet was first shown by Kübler *et al.* [2] for Co_2MnAl and Co_2MnSn pointing on peculiar transport properties. The concept of a half-metallic ferromagnet was presented by de Groot [3], predicted for the C_{1b}-Heusler compound NiMnSb. The density of states of a half-metallic ferromagnet shows a gap for minority electrons at the Fermi energy (ϵ_F). Thus, these materials are supposed to be 100% spin polarised at ϵ_F. Only the other spin direction contributes to electronic conductivity. The scheme of the density of states (DOS) for a half-metallic ferromagnet is shown in Figure 1.1. Nevertheless, the half-metallic ferromagnetism in NiMnSb is still controversially discussed [4, 5, 6, 7, 8]. Up to now, about 500 Heusler compounds X_2YZ have been already reported [9, 10]. The half-metallic ferromagnetic character of Co_2MnZ compounds was first reported by Ishida *et al.* [11]. Recently, Co_2MnSi [12] and Co_2MnGe [13] were used to build first thin film devices. So far, most of the predicted half-metallic ferromagnets belong to the class of Heusler compounds [1]. Beside Heusler compounds, there are only few other materials being predicted to be half-metallic ferromagnets, like some oxides. Most of the predicted compounds with Zincblende structure are chemically uncharacterisable, at least up to now. However, the discovery of half-metallic ferromagnetism led also to a new research area, namely the spintronics [14, 15, 16]. This research area was established by the discovery of the Giant Magneto Resistance effect (GMR) [17, 18]. The GMR effect appears in structures build of alternating layers of magnetic and nonmagnetic materials. These layers are antiferromagnetically coupled without application of a magnetic field. Thus the electrons in alternating layers bear opposite spins and are not allowed to change between layers. This results in a high resistivity. The electrons can be forced to a ferromagnetic coupling by applying a magnetic field, which leads to an oppression of the scattering between layers. Thus the resistivity decreases.

Spintronics uses the spin of electrons, in contrast to the conventional information carrier, which uses the charge of electrons. The proposed advantages of so called spintronics are non volatility of the data, large storage density and lower energy consumption. Potential applications for spintronics are magnetic hard discs, magnetic random access memories (MRAMS) as well as angle and field dependent sensors.

Apart from the search of new candidates for half-metallic ferromagnetism and spintronics, some practical aspects have to be considered before the development of new materials with a high degree of spin polarisation for technical applications.

Firstly, samples without disorder are an experimental challenge, because disorder-order phenomena strongly depend on the preparation conditions. Recently band struc-
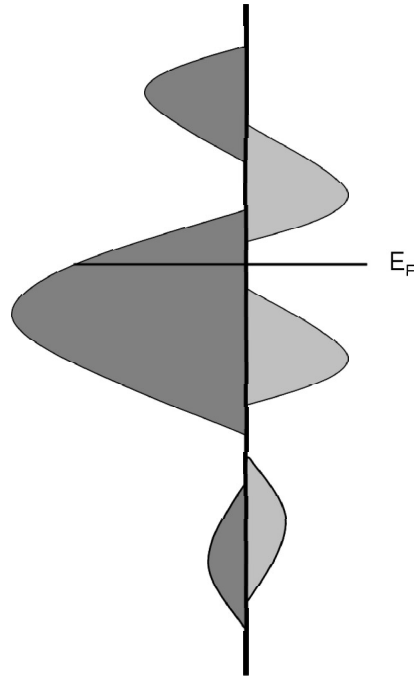
Figure 1.1: Schematic DOS of a half-metallic ferromagnet.
One spin direction exhibits a gap at ϵ_F, while the other exhibits electronic states at ϵ_F.

ture calculations revealed a decrease in spin polarisation and magnetic moment if some types of disorder occur on certain atomic positions [19, 20].

Complete disorder in the X_2YZ Heusler compounds between all sites results in the $A2$ structure-type with reduced symmetry $Im\overline{3}m$. The X, Y and Z sites become equivalent leading to a body-centered cubic lattice (see Figure 1.2), also known as the tungsten structure-type. This type of disorder has some strong effects on the properties of the investigated materials [21, 22].

It turned out that the mainly occurring type of disorder is of $B2$ type. This disorder arises in the simplest form by mixing of Y and Z atoms. Thus the Y and Z sites become equivalent, which leads to a CsCl lattice with X on the center of the cube randomly surrounded by Y and Z atoms (Figure 1.2). The symmetry is reduced and the resulting spacegroup is ($Pm\overline{3}m$). The lattice constant is the same as for the $A2$ type structure. According to electronic structure calculations, $B2$-type disorder effects the spin polarisation not as strong as other types of disorder, at least in the $Co_2Cr_{1-x}Fe_xAl$ system [23, 24] as well as for Co_2CrGa [25].

Miura et $al.$ [23, 24] reported, that a mixing of X and Y atoms, DO_3-type disorder, is unlikely due to energetic reasons. Nevertheless, Zhang et $al.$ [26] estimated the Co-(Cr,Fe) (DO_3 type) disorder in $Co_2Cr_{1-x}Fe_xAl$ compounds to be about 30%. This kind of disorder reduces the spin polarisation [23, 24]. The ordered Heusler compounds are ternary X_2YZ-compounds and crystallise in the $L2_1$ structure (see Figure 1.2). X and Y are usually transition metals while Z is a main group element. The related spacegroup
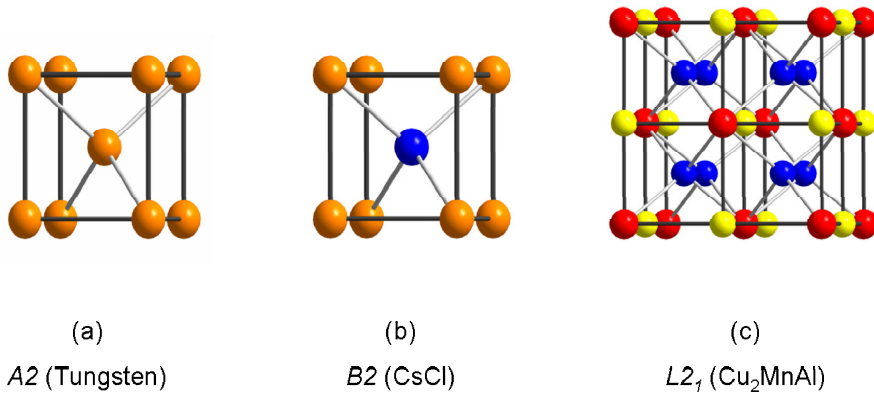
(a)   (b)   (c)

A2 (Tungsten)   *B2* (CsCl)   *L2₁* (Cu₂MnAl)

Figure 1.2: Crystal structure of a Heusler compound X_2YZ (a) $A2$, (b) $B2$ and (c) $L2_1$. The related spacegroup is $Fm\bar{3}m$.

is $Fm\bar{3}m$. X occupies the Wykhoff position $8c$ $(\frac{1}{4}\frac{1}{4}\frac{1}{4})$, Y is on $4b$ $(\frac{1}{2}\frac{1}{2}\frac{1}{2})$ and Z is on $4a$ (0 0 0). The structure can be described as a superstructure of a CsCl lattice, in which the lattice parameter of the CsCl lattice is doubled in all three dimensions. This leads to a cell consisting of eight cubes with one atom in each center. The 16 atoms in this supercell may be divided in four groups consisting of four atoms. The atoms in the center of each cube are the X atoms, while the Y and Z atoms occupy the corner of the eight cubes. Each Each atom is face centered cubic ordered, leading to four interpenetrating face centered cubic lattices. In case of only half filled centers of the eight cubes, the C_{1b}-Heusler structure is obtained.

Figure 1.3 shows the theoretical powder pattern of a Heusler compound X_2YZ in (a) $A2$, (b) $B2$ and (c) $L2_1$ type structure. The corresponding hkl value is given on top of the reflections of the $L2_1$ structure type. The hkl values correspond to the indices in the reciprocal space. The most pronounced differences in the theoretical powder pattern for ordered and disordered Heusler compounds are shown in Figure 1.3. The $L2_1$ pattern shows some additional reflections, in particular the (111) reflex at a scattering angle of 12° indicates the $L2_1$ type order.

It should be noted that some types of disorder cannot be detected easily by X-ray powder diffraction as the scattering coefficients of the $3d$-transition metals are very similar. The same applies for neutron diffraction. Due to the nearly equal scattering length of Cr and Al for neutrons, it is not possible to distinguish between ordered $L2_1$ and disordered $B2$ structures.

In particular, the $Co_2Cr_{1-x}Fe_xAl$ Heusler compounds are reported to show disorder. Co_2CrAl is predicted to be a half-metallic ferromagnet. In experiments, the compound reveals a magnetic moment of $1.55\mu_B$ [27]. This value corresponds to half of the value obtained from calculations and no integer value. This reduction of the magnetic moment might originate from an interchange of Cr and Co sites, as proposed by Miura *et al.* [23, 24]. This type of disorder leads to an antiferromagnetic coupling of the antisite - Cr with the nearest neighbour ordinary site - Cr atoms and degrades the half-metallic
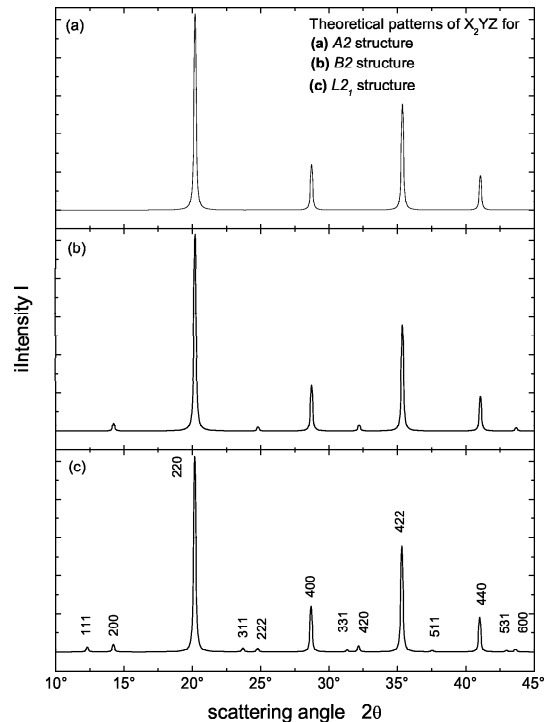
Figure 1.3: Theoretical powder pattern of a Heusler compound X_2YZ in (a) $A2$, (b) $B2$ and (c) $L2_1$ with indicated hkl values.

The diffraction pattern was calculated for excitation by Mo-K_α radiation.

character. The Heusler compounds $Co_2Cr_{1-x}Fe_xAl$ also show a magnetic moment, which is significantly too low in bulk materials [27, 28, 29, 23, 24, 30, 21, 26] and in tunnel junctions [31, 32, 33, 34] compared to the value [35, 36, 37] expected from the Slater-Pauling rule. This points to disorder effects and selective oxidation of Cr [38, 39, 40]. Nevertheless, pressed powder samples of $Co_2Cr_{0.6}Fe_{0.4}Al$ showed a very high magnetoresistance ratio (30%) at room temperature [28, 29] in bulk material and large tunneling magnetoresistance between 19% [31, 32, 33] and 42% [41, 34] in tunnel junctions.

The $Co_2Cr_{1-x}Fe_xGa$ compounds crystallise in the ordered $L2_1$ structure and the magnetic moments for the compounds with lower concentration x are in good agreement with predictions [42, 43]. Therefore, a careful sample preparation is essential, followed by a demanding structural characterisation. In order to investigate order disorder phenomena and in particular to exclude disorder a combination of diffraction and spectroscopic methods is required.

It is also possible, that also in completely ordered samples a full spin polarisation might not be detectable due to surface states [44]. The properties of the surface might differ from the bulk properties, due to altered coordination on the surface. Webster *et al.* [45] and Pierre *et al.* [46] reported segregation on surfaces for some Heusler compounds.

In addition, oxidation of the surfaces may reduce the spin polarisation. Nevertheless, the Heusler compounds seem to be promising candidates for spin dependent technical applications. In particular it should be noted that the Co_2YZ Heusler compounds exhibit the highest Curie temperature (985K, Co_2MnSi [47]) and the highest magnetic moment (5.9μ_B per unit cell, Co_2FeSi [48]) being reported so far, as well as varying magnetic moments ranging from 0.3 μ_B to 1.0 μ_B at the Co site depending on the constituents Y and Z [49, 50, 51, 52]. High Curie temperatures, magnetic moments, thermal and chemical stability and large minority gaps are desirable for various applications. Thus, these Heusler compounds are the most interesting ones for technical applications.

In 1991, de Groot [53] predicted the Heusler compound MnCrSb to exhibit ferrimagnetic coupling with compensating magnetic moments and 100 % spin polarisation at ϵ_F. This class of material was, unfortunately, called half-metallic antiferromagnets. In the following, the class of ferrimagnetic materials with complete spin polarisation at ϵ_F and a ground state with compensated magnetic moments will be refered to the following: half-metallic completely compensated-ferrimagnets (HMCCF). In addition, half-metallic completely compensated-ferrimagnets are supposed to have a potential advantage over half-metallic ferromagnets for some technical applications because they do not have a stray field and are much less affected by external magnetic fields. They could be used as sensors in spin polarised scanning tunnelling microscopes for measuring the spin polarisation of samples without perturbing the domain structures [53]. In particular, half-metallic materials with full spin polarisation and without stray magnetic fields may be useful for advanced 'spin electronic' devices [53, 54]. The half-metallic completely compensated-ferrimagnets were also predicted as a base for a new type of superconductor that has only one superconducting spin channel, the so-called single spin superconductor [55].

In the following text, a simple concept was used for a systematic search for new materials with high spin polarisation. It is based on two semi-empirical models. Firstly, the Slater-Pauling rule was used to estimate the magnetic moment. Slater [35] and Pauling [36] found that the magnetic moments (m) of $3d$ elements and their binary alloys can be described by the mean number of valence electrons per atom (n_V). The rule distinguishes the dependence of the magnetic moment m as a function of the number of valence electrons (n_V) into two regions (Figure 4.1) (Figure 1.4). In the second part ($n_V \geq 8$), one has closed packed structures (fcc, hcp) and m decreases with increasing n_V. This is called the region of itinerant magnetism. According to Hund's rule, it is often favorable that the majority d states are fully occupied ($n_{d\uparrow} = 5$). The magnetic valence is defined by $n_M = 2n_{d\uparrow} - n_V$, whereby the magnetic moment per atom is given by $m = n_M + 2n_{sp\uparrow}$. A plot of m versus magnetic valence ($m(n_M)$) is called the generalised Slater-Pauling curve (Figure 1.4 ([56, 37]). In the first region ($n_V \leq 8$), m increases with increasing n_V. This part is attributed to localised moments, where Fe (bcc) is a borderline case. Here, the Fermi energy is pinned in a deep valley of the minority electron density. This constrains $n_{d\downarrow}$ resulting in $m = n_V - 2n_\downarrow$. For Fe and its binary alloys one has an average of approximately three minority electrons with the result $m \approx n_V - 6$. Many Heusler compounds exhibit an increase of m with increasing n_V, and thus they belong to the first region of the Slater-Pauling curve. This model is confirmed
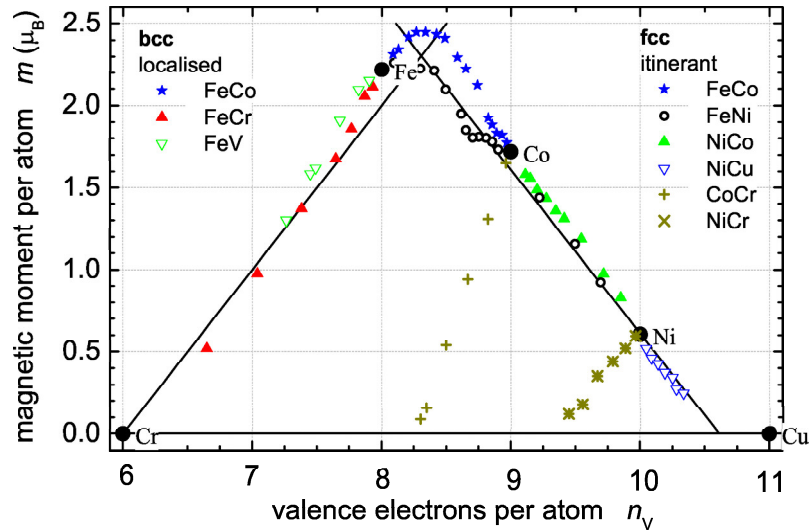
Figure 1.4: Generalised Slater Pauling curve.

by electronic structure calculations [57]. The second model was found to fit particularly well for Co_2YZ Heusler compounds when comparing their magnetic properties. It turned out that these compounds seemingly exhibit a linear dependence of the Curie temperature as function of the magnetic moment. Stimulated by these models, Co_2FeSi was revisited. The compound was investigated in detail concerning its geometrical and magnetic structure by means of X-ray diffraction, extended X-ray absorption fine structure (EXAFS), X-ray absorption- and Mößbauer spectroscopy as well as high and low temperature magnetometry, X-ray magnetic circular dichroism and difference scanning calometry. The measurements revealed that it is currently the material with the highest magnetic moment (6 μ_B) and Curie-temperature (1100 K) in the classes of Heusler compounds as well as half-metallic ferromagnets [58, 59, 60, 61]. The experimental findings are supported by detailed electronic structure calculations [57]. The same concepts were used to predict the properties of the Heusler compounds $Co_2Cr_{1-x}Fe_xAl$ [29]. The corresponding quaternary Heusler compounds $Co_2Cr_{1-x}Fe_xAl$ with varying Cr to Fe ratio x were investigated experimentally and theoretically and will be presented in the following text. The structural and chemical properties of the quaternary Heusler compounds $Co_2Cr_{1-x}Fe_xAl$ were investigated comparing powder and bulk samples [62, 63, 64]. The long range order was determined by means of X-ray diffraction and neutron diffraction, while the site specific (short range) order was proved by the extended X-ray absorption fine structure method (EXAFS). The magneto-structural properties were measured with [57]Fe Mößbauer spectroscopy in transmission mode as well as in X-ray scattering mode in order to compare powder and bulk properties. The chemical composition was analysed by means of X-ray photoemission spectroscopy (XPS). The results from these methods

are compared to get an insight in the differences between surface and bulk properties and the appearance of disorder in such alloys. The electronic structure and spectroscopic properties were calculated using the full relativistic Korringa-Kohn-Rostocker method with coherent potential approximation to account for the random distribution of Cr and Fe atoms as well as random disorder. Magnetic effects are included by the use of spin dependent potentials in the local spin density approximation. Magnetic circular dichroism in X-ray absorption was measured at the $L_{3,2}$ edges of Co, Fe, and Cr of the pure compounds and the $x = 0.4$ alloy in order to determine element specific magnetic moments. Calculations and measurements show an increase of the magnetic moments with increasing iron content. Resonant (560 eV - 800 eV) soft X-ray as well as high resolution - high energy (3.5 keV) hard X-ray photoemission was used to probe the density of the occupied states in $Co_2Cr_{0.6}Fe_{0.4}Al$ [21]. This work presents a further compound in the class of Heusler compounds. Co_2CrIn is $L2_1$ ordered. The geometrical properties were obtained from the XRD data using the Rietveld method. The magnetic properties of Co_2CrIn were measured by means of SQUID magnetometry. The material turns out to be a soft magnet with a saturation moment of 1.2 μ_B at 5 K. In contrast to Co_2YZ Heusler compounds as mentioned above, Co_2CrIn is no half-metallic ferromagnet [65].

In this work, a rule for predicting half-metallic compensated-ferrimagnets in the class of Heusler compounds will be described. This concept results from combining the well known Slater-Pauling rule with the Kübler rule. The Kübler rule states, that Mn on the Y position in Heusler compounds tends to a high localised magnetic moment. When strictly following this new rule, some candidates in the class of Heusler compounds are expected to be completely compensated-ferrimagnetic but with a spin polarisation of 100 % at the Fermi energy. This rule is applied to three examples within the class of Heusler compounds. All discussion of the materials is confirmed by electronic structure calculations.

In summary, this work will present a comprehensive characterisation of some selected Heusler compounds.

2 Calculational Details.

Self-consistent band structure calculations were carried out using the spin polarised Korringa-Kohn-Rostocker method (KKR) provided by H. Akai [66] or for full relativistic calculations by Ebert *et al.* [67, 68]. This program allows calculations in the muffin tin (MT) and the atomic sphere (ASA) approximations. Additionally, it provides the coherent potential approximation (CPA) to be used for disordered systems. This method was used to estimate the influence of disorder on the magnetic structure.

The full potential linear augmented plane wave (FLAPW) method as provided by WIEN2K [69] was used to exclude that the observed deviations are due to the spherical approximation for the potential (MT or ASA) as used in the above mentioned methods.

The tight binding (TB-) linearised muffin tin orbital (LMTO) method within the atomic sphere approximation (ASA) was used as provided by Andersen *et al.* [70].

All Brillouin zone integrations were performed on a $22 \times 22 \times 22$ mesh of k-points resulting in 256 k-points in the irreducible part of the Brillouin zone. Only in case of the HMCCF Heusler compounds, another approach was used: The self-consistent calculations employed a grid of 455 k points from a $25 \times 25 \times 25$ mesh in the irreducible part of the Brillouin zone. A $22 \times 22 \times 15$ mesh was used for integration of the tetragonal cells leading to 528 irreducible k points. A similiar mesh leads to 968 irreducible k points for the orthorhombic cell. The energy convergence criterion was set to 10^{-5} eV in all cases. Simultaneously, the charge convergence was monitored and the calculation was restarted if it was larger than 10^{-3}. In cases of doubt about convergence or quality of the integration, the number of irreducible k-points was doubled. An imaginary part of 0.002 Ry was added to the energy when calculating the density of states. It should be noted that care has to be taken while initialisation of the calculations. Slight differences of the initial spin polarisation parameter cause that the calculations converge into a not appropriate minimum of the total energy. This may result in wrong conclusions about the ground state.

The calculations were started with the most common parameterizations of the exchange-correlation functional as given by Moruzzi, Janak, and Williams [71] (MJW), von Barth and Hedin [72] (vBH), and Vosco, Wilk, and Nussair [73, 74, 75] (VWN). The generalized gradient approximation (GGA) was used in the form given by Perdew *et al* [76]. To include non-local effects, the VWN parametrization with additions by Perdew *et al* [77, 78, 79] was used (PYVWN). The so-called exact exchange is supposed to give the correct values for the gap in semi-conductors using local density approximation. Here it was used in the form given by Engel and Vosko [80] (EV).

Usually, Heusler compounds are attributed to exhibit localized moments. In that case, electron-electron correlation may play an important role. The LDA+U scheme [81] was used for calculations of the electronic structure to find out whether the inclusion of correlation resolves the discrepancy between the theoretical and measured magnetic moment. In Wien2k, the effective Coulomb-exchange interaction ($U_{eff} = U - J$, where U

and J are the Coulomb and exchange parameter) is used to account for double-counting corrections.

Several types of disorder in $Co_2Cr_{1-x}Fe_xAl$ compounds have been considered. It turned out that the mostly occurring type of disorder is $B2$ like. This type is a result of disorder in the YZ (Y=Cr, Fe, Z=Al) planes. It is found by setting the $F\,m\overline{3}m$ site occupations of the $4a$ and $4b$ sites equally to $1/2$ for Y and Z (assigned as $B2a$ in [82]). The resulting structure with reduced $P\,m\overline{3}m$ symmetry was used for the calculations. The lattice parameter is $a_{B2} = a_{L2_1}/2$. X was placed at the $1a$ site (origin of the cube) and the site occupations for Y and Z at $1b$ (center of the cube) were set equally to $1/2$. For the mixed Fe-Cr systems, the site occupation factors for Y and Y' have to be weighted by x and $(1-x)$, respectively. Complete disorder between all sites results in the $A2$ structure with reduced symmetry $I\,m\overline{3}m$.

3 Experimental Details.

All polycrystalline samples were prepared by arc-melting of stoichiometric quantities of the constituents in an argon atmosphere (10^{-4} mbar). Homogeneous samples were obtained by re-melting for several times. This procedure leads to polycrystalline ingots. Care was taken to avoid oxygen contamination. This was established by evaporation of Ti inside of the vacuum chamber before melting the compound. The weight loss was monitored to be less than 0.5%. In particular, the polycrystalline ingots of Co_2FeSi were annealed in evacuated quartz tubes at 1300 K for 20 days. This procedure resulted in samples exhibiting the correct Heusler type $L2_1$ structure. Some samples of $Co_2Cr_{1-x}Fe_xAl$ were annealed at 1273 K for several days.

Flat disks were cut from the ingots and polished for spectroscopic investigations at bulk samples. For powder investigations, the remaining part was crushed by hand using a mortar. It should be noted that pulverisation in a steel ball mill results in strong perturbation of the crystalline structure.

X-ray photo emission (ESCA) was used to verify the composition and to check the cleanliness of the samples. The spectra were excited by Al-K_α or Mg-K_α radiation to discriminate the Auger electrons from core level emission. No impurities were detected in case of Co_2FeSi by means of ESCA after removal of the native oxide from the polished surfaces by Ar^+ ion bombardment. In case of the $Co_2Cr_{1-x}Fe_xAl$ compounds, electron excited Auger electron spectroscopy (AES) was used for depth profiling. The surface of the bulk samples was removed by sputtering the polished surfaces to depth up to 0.5 μm by means of Ar^+ ion bombardment at 4keV ion energy and 25 μA target current.

The long range order of the system was investigated by means of X-ray diffraction (XRD). Powders were measured using Mo-K_α radiation (Stoe, STADIP) or Cu-K_α (Bruker, AXS D8). The measurements were performed in reflection geometry in a $\theta - \theta$ scanning mode. Bulk samples were analysed in a Philips XPert MRD diffractometer (Cu-K_α radiation) using a parallel beam geometry equipped with a long Soller-slit to enhance the resolution. In particular asymmetric diffractograms were measured at an angle of incidence of 0.5^o in order to obtain the surface contribution to the diffraction spectra. All measurements were performed at room temperature. The structural parameters were obtained from Rietveld refinement of the XRD data using the FULLPROF program [83] or the Jana 2000 program package [84].

Additionally, the geometrical structure of $Co_2Cr_{0.6}Fe_{0.4}Al$ powder samples was investigated by means of neutron diffraction at the Institute Laue-Langevin (Grenoble, France). The measurements were performed at the D1A monochromator using a neutron wavelength of 1.909 Å.

Extended X-ray absorption fine structure (EXAFS) measurements were performed at the *XAS* beamline of LNLS (Campinas, Brazil) for additional structural investigation, in particular to explain the site specific short range order. The powders (20 μm) were additionally mixed with BN and pressed to thin pellets. Powder samples were investi-

gated in transmission mode using two ion chambers, bulk samples were investigated by the total electron yield technique (TEY). The spectra were taken at the Cr, Fe, and Co K edges. The EXAFS spectra $\chi(k)$ were extracted using the AUTOBK program [85]. The ATOMS program [86] was used to prepare the structural input for FEFF6 [87]. The final data analysis was performed using the IFEFFIT program package [88, 89].

Magneto-structural investigations were carried out by means of ^{57}Fe Mößbauer spectroscopy using a constant acceleration spectrometer. A ^{57}Co(Rh) source with a line width of 0.105 mm/s was used for excitation. All powder samples were measured in transmission mode in order to investigate the bulk properties (10^6 Å). The surface properties were determined in X-ray scattering mode using 6.3 keV secondary X-ray Fe-K-α radiation with a penetration depth of around (10^4 Å). There secondary X-rays appear together with fluorescence γ-radiation after Mößbauer resonance absorption by ^{57}Fe nuclei. All isomer shift values reported below are quoted relative to α-Fe at 293 K. The Recoil 1.02 Mößbauer analysis software was used to fit the experimental spectra [90].

The magnetic properties were investigated at low temperatures using a super conducting quantum interference device (SQUID, Quantum Design MPMS-XL-5) in the temperature range $4\ K \leq T \leq 300\ K$. The high temperature magnetic properties were investigated by means of a vibrating sample magnetometer (Lake Shore Cryotronics, Inc., VSM Model 7300) equipped with a high temperature stage (Model 73034).

For site specific magnetometry, X-ray Magnetic Circular Dichroism (XMCD) in photo absorption (XAS) was performed at the *First Dragon* beamline of NSRRC (Hsinchu, Taiwan) [91, 92]. The entrance and exit slits of the monochromator were set symmetrically in the range from 10 μm to 25 μm resulting in a resolution of about 50meV at the different absorption edges. The XAS spectrum was obtained by the TEY-method, measuring directly the sample current while scanning the photon energy. The helicity of the light was fixed while two spectra with opposite directions of the external field, defined as μ^+ and μ^-, were acquired consecutively. The magnetic field applied in situ to the sample (up to 0.8 Tesla) was aligned along the surface normal and at an angle of 30 degrees with respect to the incident photon direction.

Spectra obtained for opposite field directions may exhibit different re-absorption effects of emitted electrons [93]. This effect is less prominent when the sample is oriented with the field applied perpendicular to the surface because in this case the Lorentz force causes even low energy electrons to leave the surface following a screw line. In addition, an electric field to extract electrons from the sample surface was applied. The photon flux onto the sample surface was measured by the electron yield of a Au grid positioned in the photon path. The electron yield of the Au grid showed an (unexplained) systematic dependence on the applied field H which could be phenomenologically described by an energy independent correction factor $f(H)$ ($0.98 < f(H) < 1.02$). In the following, the electron yield of the sample was normalized by the signal from the Au grid and by $f(H)$. This data correction results in a vanishing of the dichroism signal for photon energies smaller than the L_3-edge.

Soft X-ray excited photoemission was performed at the UE 56/1 PGM beamline of BESSY (Berlin, Germany). The resolution of the beamline was set to $E/\Delta E = 8000$ in the energy range from 600 eV to 800 eV with a resolution better than 100 meV. The

spectra were taken by means of a hemispherical analyser (VG ESCA-Lab). The analyser slits were set to 200 μm and a pass energy of 20 eV was used. High resolution - high energy photoemission excited by hard X-rays [94] was performed at the BL22XU beamline of SPRING-8 (Hyogo, Japan) using a Gammdata Scienta R4000-10 keV analyser [95]. For high resolution (better than 250 meV), the pass energy was set to 200 eV and the entrance slit to 0.5 mm. A 1.5 mm slit was used for spectra with lower resolution (about 500 meV), in particularly at the 8 keV photon energy were the valence band emission has a very low cross section.

Before taking the spectra excited by synchrotron radiation, the samples were scratched in situ with a diamond file in order to remove the native oxide layer from the surface. ESCA and Auger electron depth profiling revealed a thickness of the oxide layer of up to 0.5 μm depending on the sample history.

4 The Heusler Compound Co_2FeSi.

4.1 Introduction.

Several rules are used to predict the magnetic moments in Heusler compounds from the number of valence electrons. These rules are based on valence electron counting starting with the semi-conducting compounds where one has 18 valence electrons in C_{1b} compounds [19], or 24 in Heusler compounds. Rules that are not general but depend on the composition of the sample are, somehow, not satisfactory. Therefore, it may be helpful to start more basically.

As already pointed out in chapter 1, many Heusler compounds exhibit an increase of m with increasing mean number of valence electrons per atom (n_V), and thus belong to the first region of the Slater-Pauling curve.

Half-metallic ferromagnets are supposed to exhibit a real gap in the minority density of states and the Fermi energy is pinned inside the gap. Therefore, this gap leads to an integer magnetic moment. From this point of view, the Slater-Pauling rule is strictly fulfilled with

$$m_{HMF} = n_V - 6 \qquad (4.1)$$

for the magnetic moment per atom, as the number of minority electrons $n_\downarrow$ has to be integer, too. The distribution of the 6 minority electrons, however, has to be found from electronic structure calculations.

For ordered compounds with different kinds of atoms it is more convenient to work with all atoms of the unit cell. In the case of 4 atoms per unit cell, as in Heusler (FH) compounds, one has to subtract 24 (six times the number of atoms) from the accumulated number of valence electrons N_V (s, d electrons for the transition metals and s, p electrons for the main group element) to find the magnetic moment per unit cell

$$m_{FH} = N_V - 24. \qquad (4.2)$$

.

This *valence electron rule* [1] is strictly fulfilled for half-metallic ferromagnets only, as was first noted in [37] for C_{1b} Heusler (HH) compounds with 3 atoms per unit cell ($m_{HH} = N_V - 18$). In both cases the magnetic moment per unit cell becomes strictly integer (in multiples of Bohr magnetons) for half-metallic ferromagnets, what may be seen as an advantage of the *valence electron rule* compared to the original Slater-Pauling rule (Equation 4.1) although it suggests the existence of different rules.

The Slater-Pauling rule relates the magnetic moment to the number of valence electrons per atom [35, 36], but does not, per se, predict a half-metallic behavior. The gap in

---

[1]This term is used in the following to distinguish the rule derived from the overall number of valence electrons in the unit cell from the more general Slater Pauling.

the minority states of Heusler compounds has to be explained by details of the electronic structure (for examples see [2] and references there).

Self consistent field calculations were performed in order to investigate the Slater-Pauling like behaviour of Heusler compounds in more detail. The electronic structure of most known Heusler compounds were calculated in order to find their magnetic moments and type of magnetic structure. The calculations were performed for overall 107 reported Heusler compounds from which 59 are based on X and Y being $3d$ metals, 17 with only X and 28 with only Y being a $3d$ metal. The remaining ones contain $4d$ and $4f$ metals on the X and Y sites, respectively. In addition calculations were performed for 50 reported C_{1b} Heusler compounds

It turned out that nearly all Co$_2$YZ compounds (if not simple metals) should exhibit half-metallic ferromagnetism. It is also found that the calculated magnetic moments of the Co$_2$ based compounds follow the Slater-Pauling curve as described above (see Figure 4.1a). Some small deviations are possibly caused by inaccuracies of the numerical integration.

Inspecting the other transition metal based compounds, one finds that compounds with magnetic moments above the expected Slater-Pauling value are X=Fe based. Those with lower values are either X=Cu or X=Ni based, with the Ni based compounds exhibiting higher moments compared to the Cu based compounds at the same number of valence electrons. Moreover, some of the Cu or Ni based compounds are not ferromagnetic independent of the number of valence electrons. Besides Mn$_2$VAl, only compounds containing both, Fe and Mn, were found to exhibit half-metallic ferromagnetic character with magnetic moments according to the Slater-Pauling rule. No attempts have been made to perform calculations for compounds that turn out to be chemically uncharacterizable.

Inspecting the magnetic data of the known Heusler compounds in more detail (see data and references in [9, 10]), one finds a very interesting aspect. Seemingly, a linear dependence is obtained for Co$_2$YZ Heusler compounds when plotting the Curie temperature (T_C) of the known, $3d$ metal based Heusler compounds as function of their magnetic moment (see Figure 4.1b). According to this plot, T_C is highest for those half-metallic compounds that exhibit a large magnetic moment, or equivalent for those with a high valence electron concentration as derived from the Slater-Pauling rule. T_C is estimated to be above 1000K for compounds with 6 μ_B by an extrapolation from the linear dependence.

Co$_2$FeSi was revisited as a practical test for the findings above. Niculescu et $al.$ reported in [48]: $a = 5.66$ Å, $T_C > 980$ K and $m = 5.9$ μ_B at 10 K; the lattice parameter (5.64 Å) found here agrees with the one reported in [48] for Fe$_2$CoSi; values for a and m reviewed later [10, 96] are considerably different, for unknown reasons. In addition, this compound was previously reported to have a magnetic moment of only 5.18 μ_B per unit cell and a Curie temperature of above 980 K [48, 96]. One expects, however, $m = 6$ μ_B and T_C to be above 1000 K, from the estimates given above.
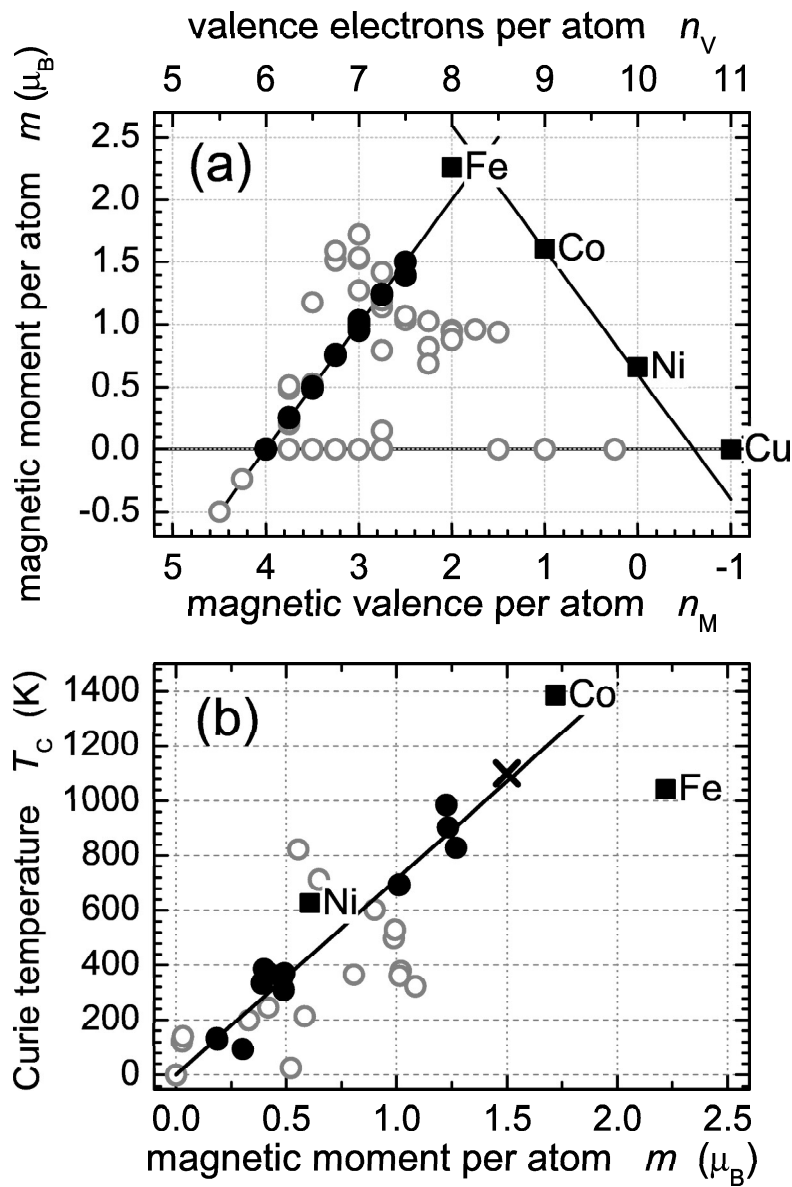
Figure 4.1: Magnetic moments (a) and Curie temperature (b) of Heusler compounds. The heavy $3d$ transition metals are given for comparison. Full dots assign Co_2YZ and open circles assign other Heusler compounds. The lines in (a) assign the Slater-Pauling curve. The line in (b) is found from a linear fit for Co_2YZ compounds. The cross in (b) assigns Co_2FeSi as measured in this work.

KKR	MT			ASA		
	m_{tot}	m_{Co}	m_{Fe}	m_{tot}	m_{Co}	m_{Fe}
MJW	5.03	1.19	2.69	5.17	1.27	2.68
vBH	4.88	1.15	2.64	5.03	1.22	2.62
VWN	4.99	1.18	2.68	5.15	1.26	2.67
GGA	5.22	1.22	2.85	5.18	1.27	2.69
EV	5.19	1.24	2.77	5.15	1.26	2.68
PYVWN	5.03	1.19	2.72	5.67	1.25	3.23

Table 4.1: Magnetic moments of Co$_2$FeSi calculated for spherical potentials.
The calculations were carried out by means of KKR in muffin tin (MT) and atomic sphere
(ASA) approximations for a=5.64 Å. All values are given in μ_B. Total moments are given
per unit cell and site resolved values are per atom.

4.2 Electronic Structure

As starting point, self consistent first principle calculations were performed using the
linearized muffin tin orbital (LMTO) method [97], as this method is very fast. Using
the experimental lattice parameter (a_{exp}=5.64 Å, see Section 4.3), the results predicted
Co$_2$FeSi to be a regular ferromagnet with a magnetic moment of 5.08 μ_B per formula
unit. The latter value is much too small compared to the experimental one of 6 μ_B (see
Section 4.4).

More detailed calculations were performed to check if the too low value is the result
of a particular method or the parameterization of the energy functional.

The results of the calculations using different approximations for the potential as well
as the parameterization of the exchange-correlation part are summarized in Table 4.1.
The calculated total magnetic moments range from ≈ 4.9 μ_B to ≈ 5.7 μ_B, thus they are
throughout too low compared to the experiment. They include, however, the value of
5.27 μ_B found in reference [98] by means of the full potential KKR method.

The calculated magnetic moments for most known Heusler compounds are summarized
in Figure 4.1 and discussed in Section 4.1. It turned out, however, that the magnetic
moment of Co$_2$FeSi is still too small compared to the experimental value.

Comparing the results for Co$_2$FeSi, the magnetic moments found by the different
calculational schemes are very similar (compare Table 4.1 and 4.2), implying that Co
and Fe atoms are aligned parallely independent of the method used. The small, induced
moment at the Si atom (not given in Table 4.1) is aligned anti-parallely to the magnetic
moment at the transition metal sites. As for KKR, the use of the EV parameterization
of the energy functional did not improve the magnetic moment, the result was only
5.72 μ_B.

Other than the LMTO or KKR methods (spherical potentials), the (full symmetry
potential) FLAPW calculations revealed a very small gap in the minority states, but
being located below ϵ_F. Figure 4.2 shows the band structure and density of states
calculated by FLAPW for the experimental lattice parameter.

The electronic structure shown in Figure 4.2 reveals a very small indirect gap in the

	m_{tot}	m_{Co}	m_{Fe}	m_{Si}	m_{int}
LDA (VWN)	5.59	1.40	2.87	-0.01	-0.07
LDA (EV)	5.72	1.45	2.94	-0.003	-0.11
LDA+U	6	1.54	3.30	-0.13	-0.25

Table 4.2: Magnetic moments of Co$_2$FeSi calculated for full symmetry potentials. The calculations were carried out by means of FLAPW for $a = 5.64$ Å. All values are given in μ_B. Total moments are given per unit cell and site resolved values are per atom. m_{int} is the part of the magnetic moment that cannot be attributed to a particular site.
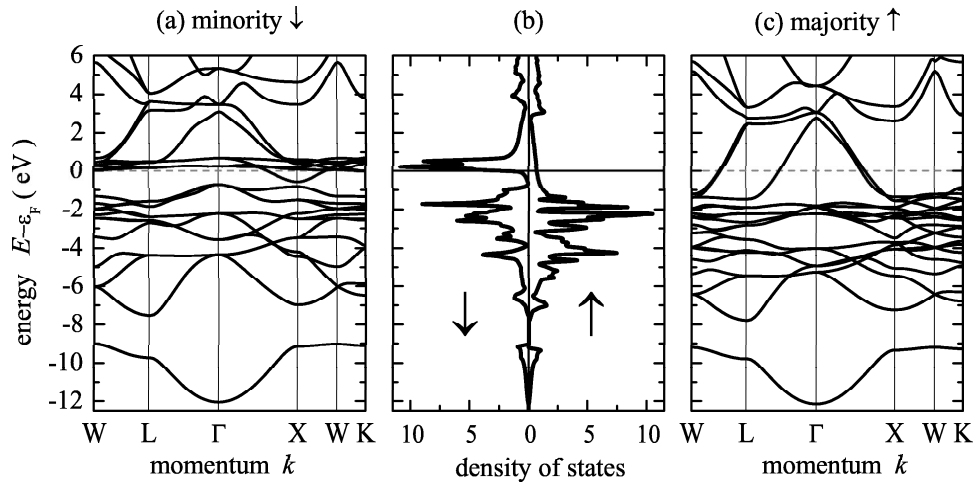
Figure 4.2: LDA band structure and DOS of Co$_2$FeSi. The calculation was performed by Wien2k using the experimental lattice parameter.
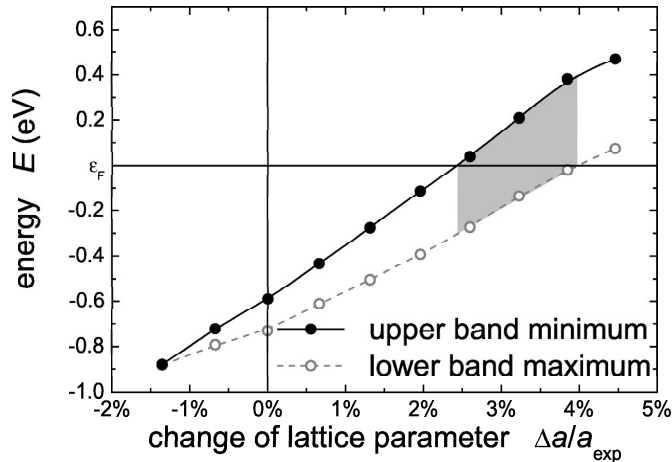
Figure 4.3: Minority gap in Co$_2$FeSi.
Shown are the positions of the extremal energies of the upper and lower bands depending on the lattice parameter ($a_{exp} = 5.64$Å). Energies are given with respect to the Fermi energy. The grey shaded area marks the domain of half-metallic ferromagnetic character (lines are drawn to guide the eye).

minority states at about 2eV below ϵ_F. The fact that the Fermi energy cuts the minority bands above the gap finally results in a magnetic moment too low and not integer, as it would be expected for a half-metallic ferromagnet.

A structural refinement was performed to check if the experimental lattice parameter minimizes the total energy. The dependence of the energy with lattice parameter a revealed that the minimum occurs at the experimentally observed lattice parameter a_{exp}. From the lattice parameter dependent calculations it showed up that the experimentally found magnetic moment appeared at larger values of a. At the same time the size of the gap increased. Inspecting the band structure, one finds that the ϵ_F is inside the gap for lattice parameters being enlarged by about 7.5% to 12.5%. Figure 4.3 shows the dependence of the extremal energies of the lower (valence) band and the upper (conduction) band of the minority states enveloping the gap.

The magnetic moment is integer ($6\mu_B$) in the region were ϵ_F falls into the gap (grey shaded area in Figure 4.3), which is the region of half-metallic ferromagnetism. The reason for the integer value is clear: the number of filled minority states is integer and thus the magnetic moment, too.

The LDA+U scheme [81] was used to approximate electron-electron correlations. It turned out that values of U_{eff} from 2.5 eV to 5.0 eV for Co and simultaneously 2.4 eV to 4.8 eV for Fe result in a magnetic moment of $6\mu_B$ and a gap in the minority states.

Figure 4.4 shows the band structure and density of states calculated using the LDA+U method. The effective Coulomb-exchange parameter were set to U$_{eff,Co} = 4.8$ eV and U$_{eff,Fe} = 4.5$ eV at the Co and Fe sites, respectively. These values are comparable to
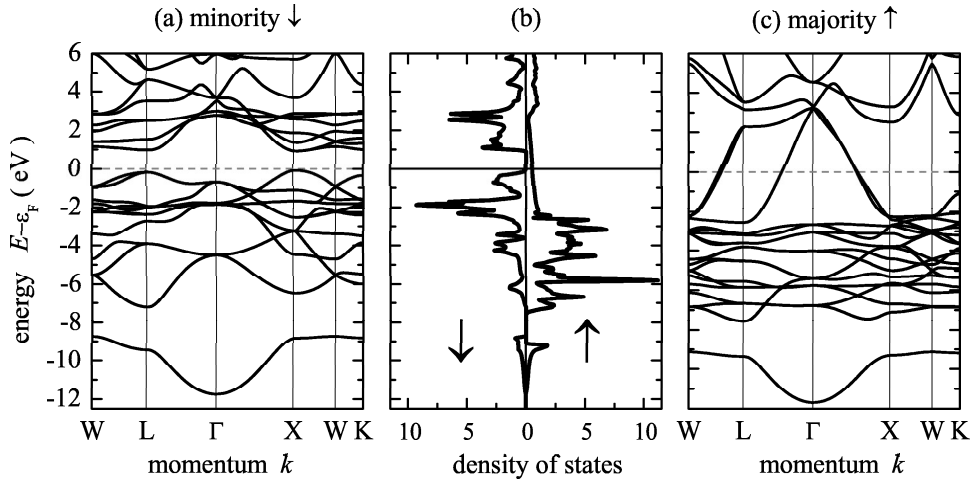
Figure 4.4: LDA+U band structure and DOS of Co$_2$FeSi.
The calculation was performed by Wien2k using the experimental lattice parameter.

	majority	minority
Co	4.887	3.343
Fe	5.063	1.766
Si	1.247	1.373
interstital	1.915	2.176
sum Co$_2$FeSi	18	12

Table 4.3: Distribution of the valence states in Co$_2$FeSi.
The number of occupied states was calculated by means of FLAPW using LDA+U for $a = 5.64$ Å. The muffin tin radii were set for all sites to $r_{MT} = 1.22$ Å. This results in a space filling of 67% by the atomic spheres, the remainder is taken as interstitial.

those found in reference [99] for bcc Fe (4.5 eV) and fcc Ni (5 eV).

The minority DOS (Figure 4.4) exhibits a clear gap around ϵ_F, confirming the half-metallic character of the material. The high density below ϵ_F is dominated by d-states being located at Co and Fe sites. Inspecting the majority DOS one finds a small density of states near ϵ_F. This density is mainly derived from states located at Co and Si sites.

The distribution of the charge density on the atoms and states with different orbital momentum is given in Table 4.3 (Note that two Co atoms count for the sum of the charge in the unit cell.).

From Table 4.3 it is found that in average three minority states per atom are occupied ($2n_\downarrow = 6$) as required by the Slater-Pauling rule for the range of increasing magnetic moments with an increasing number of valence electrons (see Section 4.1). It is worth-while to note that the same is true for the other Heusler compounds shown in Figure 4.1
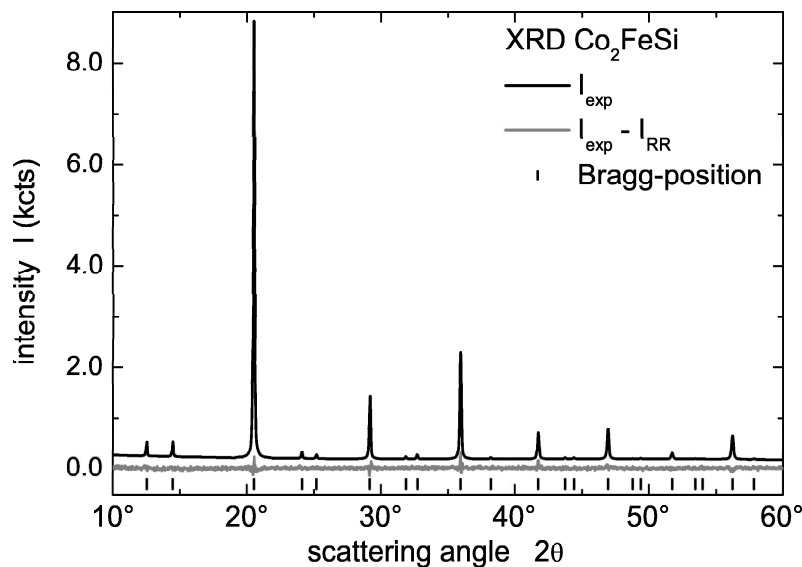
Figure 4.5: Rietveld-refinement of Co$_2$FeSi.
The black line shows the measurement. The upright bars stand for the Bragg positions and the grey line shows the difference between the calculation and the measurement.

exhibiting half-metallic ferromagnetism. However, the electrons are distributed in a different way across the X, Y, and Z sites.

4.3 Structural Properties.

The correct $L2_1$ structure Co$_2$FeSi was verified by XRD. The lattice constant was determined to be 5.64 Å. The lattice parameter is obviously smaller than the one reported before ([100]) and a lower degree of disorder is observed in the present work.

A disorder between Co and Fe atoms (DO_3 type disorder) can be excluded from the Rietveld refinement of the XRD data (see Figure 4.5), as well as from neutron scattering data (not shown here). A small disorder between Fe and Si ($B2$ type disorder) atoms ($< 10\%$) can not be excluded by neither of these methods, particularly due to the low intensities of the (111) and (200) reflections in XRD.

For further site specific structural information, EXAFS measurements were carried out. A powder sample, as used for XRD, was investigated in transmission mode.

The absorption spectra collected at the Fe and Co K-edges after removal of a constant background are shown in Figure 4.6. The best fitting of the Fourier transform modulus considering the $L2_1$ structure are also displayed in Figure 4.6. These measurements corroborate the XRD results even at the short range order for both Co and Fe. It

was not possible to fit the experimental data to a structural model including DO_3 type disorder, as expected.

The radial distribution function $\chi(R)$ is produced by forward Fourier transform of the EXAFS spectra after background subtraction. It is given as function of the effective distance R. Note that R includes the nearest neighbor distance and the scattering phase shift. The high intensity of $\chi(R)$ in the first co-ordination shell of Fe points on the cubic environment consisting of eight Co atoms, as expected for a well ordered Heusler compound. The peak of $\chi(R)$ for the first co-ordination shell of Co exhibits a clear splitting due to the different scattering phases of Fe and Si, although the distance between these atoms and Co is the same. The Fe induced intensity of $\chi(R)$ is about half of that observed in the Fe K-edge spectra. This confirms the tetragonal environment at the Co sites with respect to Fe sites, as the scattering factors for both types of atoms are nearly the same. Thus, the EXAFS measurements corroborate the XRD results even at the short range order for both Co and Fe.

For an additional magneto-structural investigation, Mößbauer spectroscopy was performed. The measurements were carried out at 85 K using powder samples. The observed 6-line pattern of the spectrum (Figure 4.7) is typical for a magnetically ordered system. The observed ^{57}Fe Mößbauer line width of 0.15 mm/s is characteristic for a well-ordered system. The value is comparable to 0.136 mm/s observed from α-Fe at 4.2 K.

In detail, the Mößbauer spectrum shown in Figure 4.7 exhibits a sextet with an isomer shift of 0.23 mm/s and a hyperfine magnetic field of 26.3×10^6 A/m. No paramagnetic line was observed. Further, no quadrupole splitting was detected in accordance with the cubic symmetry of the local Fe environment. A DO_3-like disorder (mixing of Co and Fe at X and Y sites) can be definitely excluded from a comparison of the measured (26.3×10^6 A/m) and calculated values (21×10^6 A/m for Fe in Y and 11×10^6 A/m for Fe in X positions) of the hyperfine field. This value is in agreement with the one found by Niculescu [48, 100] with spin echo nuclear magnetic resonance experiments. Niculescu *et al.* reported the hyperfine field for Fe at the 4a site to be 26.9×10^6 A/m. This observation confirms the occupation of a single site for Fe and thus a well ordered system. In addition, the values suggest that Fe in Co_2FeSi may be described as Fe^{3+}.

4.4 Magnetic Properties.

Low temperature magnetometry was performed by means of SQUID to proof the estimated saturation moment. The results are shown in Figure 4.8. The measured magnetic moment in saturation is (5.97 ± 0.05) μ_B at 5 K corresponding to 1.49 μ_B per atom. An extrapolation to 6 μ_B per unit cell at 0 K fits perfectly to the one estimated from the Slater-Pauling rule. The measurement of the magnetic moment reveals, as expected for a half-metallic ferromagnet, an integer within the experimental uncertainty. The result of the measurement (an integer) and the *valence electron rule*, sum up to an evidence for half-metallic ferromagnetism in Co_2FeSi. In more detail, Co_2FeSi turns out to be soft magnetic with a small remanence of $\approx 0.3\%$ of the saturation moment and a small coercive field of ≈ 750 A/m, under the experimental conditions used here. The magnetic
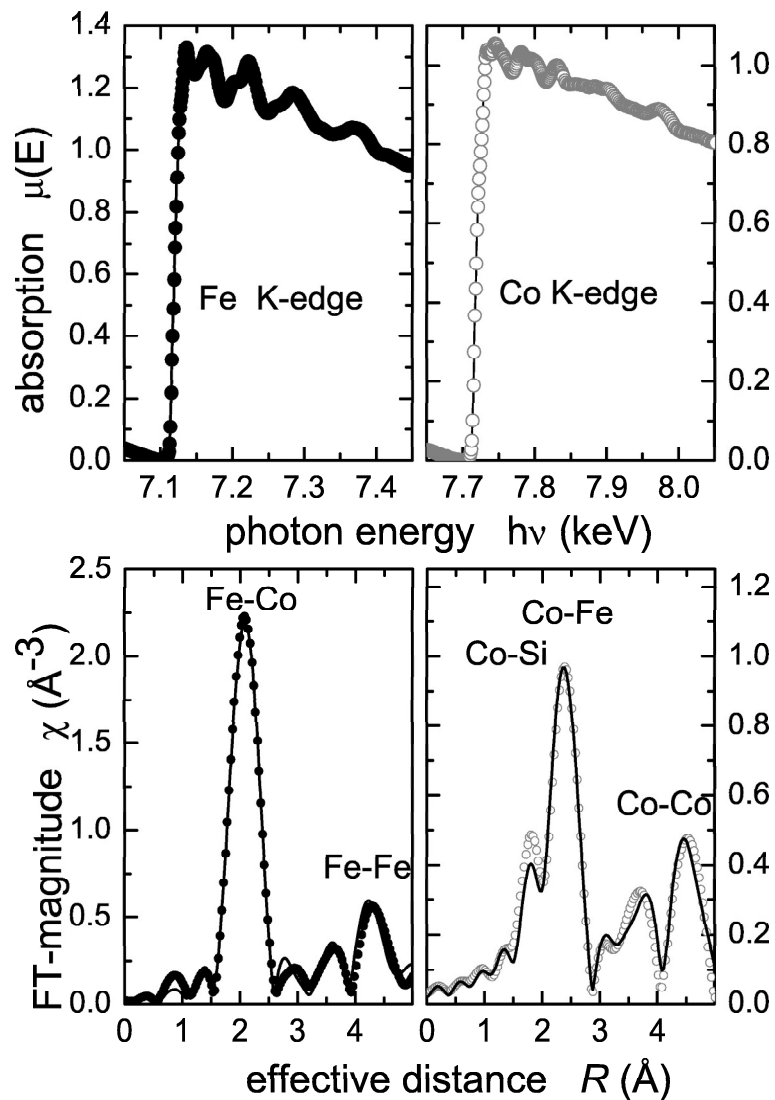
Figure 4.6: EXAFS results for Co$_2$FeSi.
The X-ray absorption spectra (with constant background removed) were taken at the K-edges of Co and Fe. The radial distribution functions derived from the spectra (symbols) are compared to the ones calculated (lines) using the best fit data.
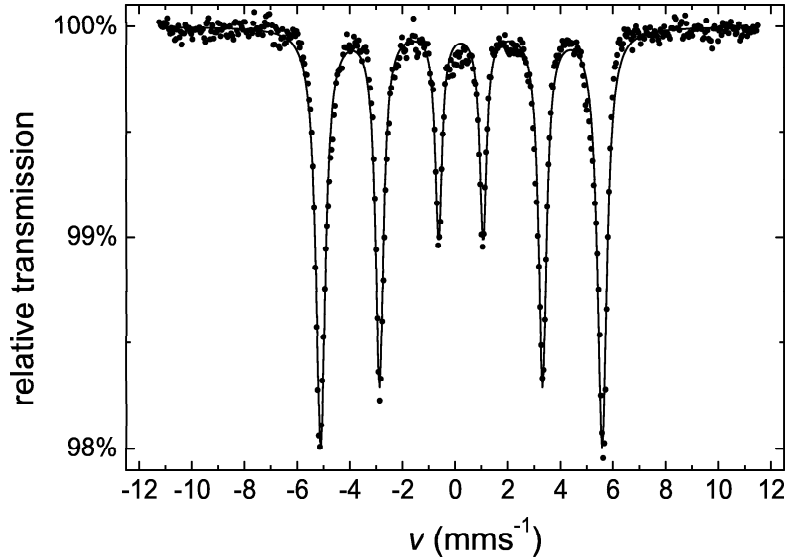
Figure 4.7: Mößbauer-spectrum of Co_2FeSi. The sample was excited by [57]Co and measured from a powder sample in transmission geometry at $T = 85$ K.

moment for Co_2FeSi was previously reported to be 5.90 μ_B [48] at 10.24 K, but with a rather high degree of disorder (11% $B2$ and 16% DO_3). Later the same group reported [100] a smaller magnetic moment ($\approx$ 5.6 μ_B interpolated to 0 K) at a lattice parameter of 5.657 Å, but still with a high degree of disorder.

The experimental magnetic moment is supported by the band structure calculations [57], revealing a half-metallic ferrromagnetic character with a magnetic moment of 6 μ_B, if using appropriate parameters in the self consistent field calculations.

XMCD in photo absorption was measured to investigate the site specific magnetic properties. The XAS and XMCD spectra taken at the $L_{3,2}$ absorption edges of Fe and Co are shown in Figure 4.9. An additional spectral feature is visible at 3 eV below the L_3 absorption edge of Co is related to the $L2_1$ structure and points on the high structural order of the sample (it vanishes for $B2$-like disorder). The magnetic moments per atom derived from a sum rule analysis [101, 102] are (2.6 ± 0.1) μ_B for Fe and $(1.2 \pm 0.1)\mu_B$ for Co, at $T = 300$ K and $\mu_0 H = 0.4$ T. The error arises mainly from the unknown number of holes in the $3d$ shell and the disregard of the magnetic dipole term in the sum rule analysis. The orbital to spin magnetic moment ratios are about 0.05 for Fe and 0.1 for Co. All values (ratio of Co and Fe moments, as well as values extrapolated to 0 K) are in good agreement to the electronic structure calculations, keeping in mind that calculated site resolved values always depend on the Muffin-Tin-radius(RMT)-settings for the integration of the charge density around a particular atom.

The high temperature magnetisation of Co_2FeSi was measured by means of VSM.
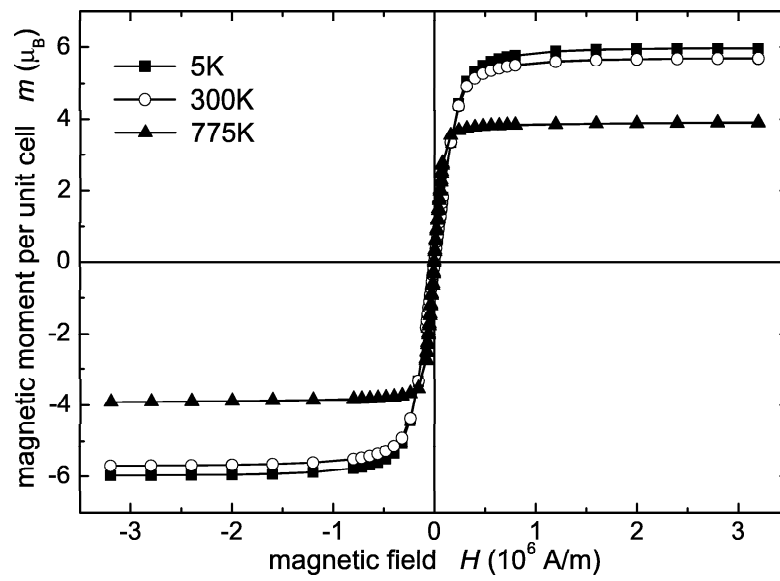
Figure 4.8: Magnetic properties of Co$_2$FeSi.
The field dependence of the magnetic moments was measured by SQUID magnetometry at different temperatures.
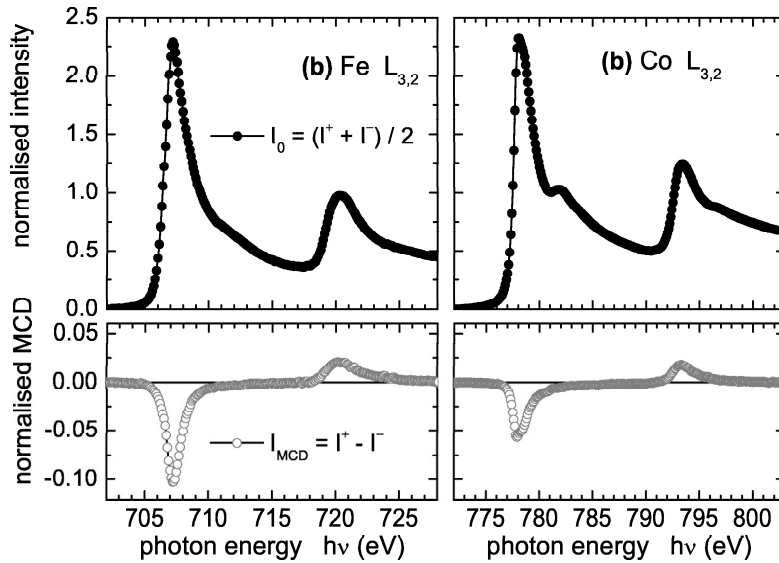
Figure 4.9: Site resolved magnetic properties of Co$_2$FeSi.
Shown are the XAS (I_0) and XMCD (I_{MCD}) spectra taken at the $L_{2,3}$ absorption edges of Fe (a) and Co (b) after subtracting a constant background.

The specific magnetisation as function of the temperature is shown in Figure 4.10. The measurements were performed in a constant induction field of $\mu_0 H = 0.1$ T. For this induction field, the specific magnetisation at 300 K is 37% of the value measured in saturation. The ferromagnetic Curie temperature is found to be $T_C = (1100 \pm 20)$ K. This value fits very well into the linear behavior shown in Figure 4.1 for Co$_2$YZ Heusler compounds.

The Curie temperature is well below the melting point being obtained by means of differential scanning calorimetry (DSC) to be $T_m = (1520 \pm 5)$ K.

The paramagnetic Curie-Weiss temperature Θ was estimated from a plot of the inverse susceptibility ($1/\chi$) as a function of temperature (Figure 4.10). The Curie-Weiss temperature is found by interpolating $1/\chi(T)$ to be (1150 ± 50) K. A true linear behavior for $1/\chi$ as a function of temperature is not observed here because the experiment was performed in a temperature range close to the Curie temperature. A linear dependence can be expected from molecular field theory only for temperatures far above T_C.

The here observed properties of Co$_2$FeSi are in agreement to those reported previously by Niculescu *et al.* [48, 100] for a higher degree of disorder (10% $B2$ plus 16% DO_3).

SQUID magnetometry often does not allow to determine high temperature magnetic phase transitions. The low temperature requirement of the instrumental set-up may not be met, in particular if T_C is very high. Differential scanning calorimetry (DSC) [43] is well established to investigate various kinds of phase transitions in solid materials.
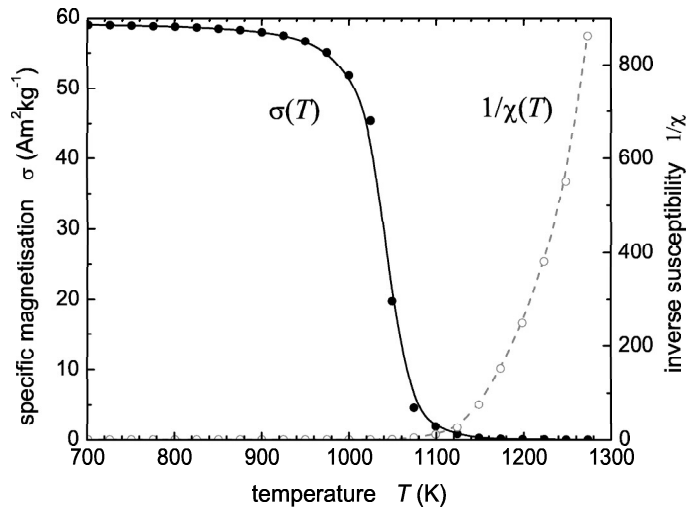
Figure 4.10: Measurement of the specific magnetisation as a function of temperature (black dots) and inverse suceptibility (white dots). (Lines are drawn to guide the eye).

Here it was used to examine the magnetic phase transition in order to support the Curie temperature received by the VSM experiments. Figure 4.11 compares the DSC signal (b) with the derivative of the specific magnetisation (a) with respect to the temperature (compare Figure 4.1b). The minimum at (1040 ± 20) K in Figure 4.10 corresponds to the maximum change of the magnetisation with temperature. With DSC, a pronounced shift of the signal is observed during cooling or heating at about 1017 K and 1037 K, respectively. This shift is due to the hysteresis of the DSC method and depends on the temperature gradient $\dot{T}(t)$. The signals might be attributed to changes of the magnetic properties. Therefore, one expects a mean value of (1030 ± 5) K for the magnetic phase transition of Co_2FeSi. The melting point was also observed by DSC and found to be $T_m = (1517 \pm 5)$ K (not shown in Figure 4.11).

The observation of the magnetic transition by DSC is verified by the comparison of the structures in DSC with the differential magnetisation. The latter is clearly observed at the point of maximum change of the magnetisation with temperature. It is seen that the value obtained by DSC is slightly lower than T_C determined from the VSM measurement. For Co_2FeSi one finds it to be only 4.5% below the Curie temperature measured by the VSM. The structural transition temperature of the $L2_1$ phase to the $B2$ phase $T_t^{B2 \leftrightarrow L2_1}$ is very close to the Curie-temperature as measured by DSC. Thus, the transition measured by DSC might be attributed to either the Curie-temperature as well as to the $T_t^{B2 \leftrightarrow L2_1}$ phase transition. Recent measurements by Balke et $al.$ [103] on the $Co_2Mn_{1-x}Fe_xSi$ serie give hint, that the transition measured with DSC is the $T_t^{B2 \leftrightarrow L2_1}$ phase transition. This order-disorder phase transition is independent of the Fe concentration x and occurs at about 1030 K.
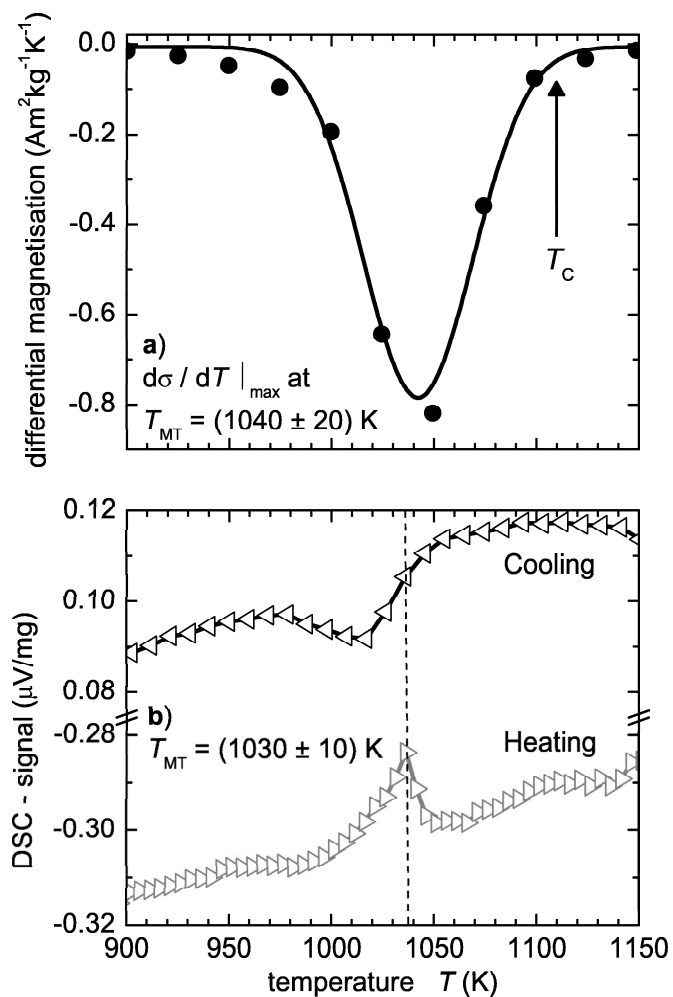
Figure 4.11: Phase transition in Co$_2$FeSi.
The differential magnetisation (a) close to T_C is compared to the measurement with the differential scanning calorimetry (b).

The highest known Curie temperature is reported for elemental Co to be 1388 K [104]. Only few materials exhibit a T_C above 1000 K, for example the Fe-Co binary alloys. With a value of $\approx$ 1100 K, Co$_2$FeSi has a higher Curie temperature than Fe and the highest of all half-metallic ferromagnets and Heusler compounds being measured up to now.

4.5 Summary for Co$_2$FeSi.

In summary, it was shown how simple rules may be used to estimate the properties of magnetic materials, in particular for those Heusler compounds exhibiting half-metallic ferromagnetism.

As practical application of these simple rules, it was found that the Heusler compound Co$_2$FeSi is a half-metallic ferromagnet exhibiting the highest Curie temperature and magnetic moment. In particular, a magnetic moment of 6 μ_B and a Curie temperature of 1100 K were found in $L2_1$ ordered samples with a lattice parameter of 5.64 Å.

The experimental findings are well supported by electronic structure calculations [57]. The comparison between experiment and calculations gives clear advise that electron-electron correlation plays an important role in Heusler compounds.

5 The Heusler Compounds $Co_2Cr_{1-x}Fe_xAl$.

5.1 Introduction.

The ferromagnetic properties of the Heusler compounds $Co_2Cr_{1-x}Fe_xAl$ have been investigated experimentally and theoretically. $Co_2Cr_{0.6}Fe_{0.4}Al$ is of special interest because a relatively high magneto-resistance ratio of up to 30% was found in powder samples in a small magnetic field of 0.1 T [29, 28]. Thin films of the compound were successfully grown by several groups [105, 106, 107, 108]. A magneto-resistance ratio of 26.5% [31] (at 5 K) and 19% [32] (at room temperature) was found for a tunnelling magnetoresistance (TMR) device of the same compound. Very recently, Marukame et al. [41] reported a TMR ratio of 74% at 55 K for a $Co_2Cr_{0.6}Fe_{0.4}Al$-MgO-CoFe magnetic tunnel junction. A spin polarisation of only less than 49% was found for polycrystalline samples by means of Andreev reflections [109]. The observation of an incomplete spin polarisation may not only be caused by the model used to interpret the data [109, 110] but also by the properties of the sample. Clifford *et al.* [111] recently reported a spin polarisation of 81% in point contacts of $Co_2Cr_{0.6}Fe_{0.4}Al$.

For Co_2CrAl a ground state magnetic moment of 1.55 μ_B/formula unit has been reported [96] and it was considered that Co atoms mainly carry the magnetic moment in this alloy whereas the contribution of Cr and Al atoms remains negligible [112]. Recent LMTO band structure calculations [28] reveal a half-metallic character of the DOS. According to our calculation all constituents of the alloy should possess a magnetic moment, 0.77 μ_B/atom for Co, 1.63 μ_B/atom for Cr and -0.10 μ_B/atom for Al. For the total moment a value of approximately 3 μ_B/formula unit is obtained, in agreement with the *valence electron rule* for the magnetic moment μ of half-metallic Heusler compounds (see equation 4.2). Experimentally determined magnetic moments for Co_2CrAl vary from 1.5 μ_B per formula unit to 3.0 μ_B per formula unit [28]. Reproducible magnetic moments could be obtained in agreement with the *valence electron rule* if Cr is partly replaced by Fe [28].

X-ray and neutron diffraction were used as a starting point for the long range order investigations on $Co_2Cr_{1-x}Fe_xAl$. Both methods are necessary, as the similar scattering coefficients of the constituents (Co, Cr, and Fe for X-rays and Cr, Al for neutrons) bear an experimental and anlytical challenge for the determination of order and disorder effects. The short range order was proved by the extended X-ray absorption fine structure method (EXAFS). The magneto-structural properties were measured by means of ^{57}Fe Mößbauer spectroscopy in transmission mode as well as in X-ray scattering mode in order to compare powder and bulk properties. The chemical composition was analysed by means of X-ray photoemission spectroscopy (XPS) combined with Auger electron spectroscopy (AES) depth profiling. The results from these methods are compared to get an insight in the differences between surface and bulk properties and the appearance of disorder in such alloys.

X-ray photoabsorption spectroscopy provides a way to study the unoccupied electronic structure of these materials. In combination with circularly polarised light it allows the determination of the element specific magnetic moments. In particular, the $L_{3,2}$ edges of the ferromagnetic $3d$ transition metals are easily accessible in the soft X-ray range (500 eV to 800 eV) as they exhibit pronounced white lines. X-ray magnetic circular dichroism (XMCD) [113, 38] was used in the present work to study the site specific magnetic moments in $Co_2Cr_{1-x}Fe_xAl$.

Photoemission spectroscopy is the method of choice to study the occupied electronic structure of materials. Excitation by low energies gives direct access to the band structure. However, low kinetic energies result in a low electron mean free path being only 6 Å at and below 100 eV (all values calculated for Co_2CrAl using the TPP2M equations [114]). Thus, resonant excitation at the M edges of the $3d$ metals may hardly be assigned as bulk sensitive because only one Heusler unit cell will contribute, for example. The situation becomes better at higher energies (18 Å at 700 eV) close to the L absorption edges of Fe and Co or for typical $Al-K_\alpha$ laboratory sources (31 Å at 1.4 keV). In the hard X-ray region above 3.5 keV one will reach true bulk sensitivity with an escape depth being larger than 65 Å for electrons emitted from the Fermi energy.

High energy photoemission (up to 15 keV excitation energy) was first performed as early as 1989 [115] using a ^{57}Co Mößbauer γ-source for excitation. However, the resolution was very low due to the limitations given by the low intense source and single channel detection of the electrons [116]. Nowadays, high energy excitation and analysis become easily feasible due to the development of high intense sources (insertion devices at synchrotron facilities) and multi-channel electron detection. Thus, high resolution - high energy photoemission (HRHEPE) was recently introduced by several groups [94, 117, 118, 119, 120, 121] as a bulk sensitive probe of the electronic structure in complex materials. In the present work, resonant photoemission (at the $L_{3,2}$-edges of the transition metals) and HRHEPE (< 3.5 keV) were used to study the density of states of $Co_2Cr_{0.6}Fe_{0.4}Al$.

The present work reports on the electronic, magnetic, and spectroscopic properties of the Heusler compound $Co_2Cr_{1-x}Fe_xAl$. The calculated properties are compared to experiments. Deviations from the $L2_1$ structure are discussed by means of disordered, random alloys. Site disorder seems to play an important role for the magnetic properties as well as the spin polarisation of $Co_2Cr_{1-x}Fe_xAl$.

5.2 Structural Properties.

5.2.1 X-ray and Neutron Diffraction.

The long range order of the materials was investigated by XRD on powders and bulk samples. The powder measurements show the bulk properties, while the bulk samples reveal the surface properties, depending on the penetration depth of the used technique. Figure 5.1 shows the powder patterns of (a) $Co_2Cr_{0.6}Fe_{0.4}Al$ and (b) Co_2FeAl samples. All reflections are indexed with their hkl-value and their intensities are normalised relative to the (110) reflex for better comparison. As can be seen from Figure 5.1 the
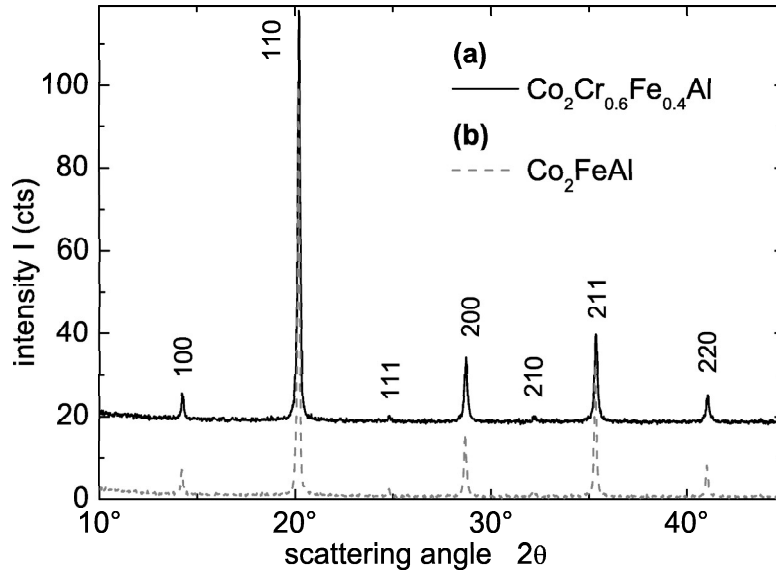
Figure 5.1: XRD from $Co_2Cr_{1-x}Fe_xAl$ powder material.
Powder XRD measurements of (a) $Co_2Cr_{0.6}Fe_{0.4}Al$ and (b) Co_2FeAl excited by Mo K_α. The samples clearly show $B2$ structure.

diffractograms of the doping serie $Co_2Cr_{1-x}Fe_xAl$ clearly show $B2$-type disorder. This can be deduced in particular from the missing of the $L2_1$ superstructure reflex at a scattering angle of $12°$ 2θ. The measured XRD data of $Co_2Cr_{1-x}Fe_xAl$ were refined by the Rietveld method using $B2$ structure (space group $P\,m\bar{3}m$) as input model. The lattice constant for all samples was determined to be 2.86 Å, as expected (this corresponds to 5.72 Å for the $L2_1$ cell of the regular Heusler structure). The fitting resulted in $R_{Bragg} \approx 5$ for the different samples.

The surface sensitive measurements as shown in Figure 5.2 reveal diffraction pattern that differ clearly from the powder pattern. Again, the intensities are normalised to the (110) reflex. It is seen that the intensity of the (100) and (200) reflections increases relatively with respect to (110). This means that the surface is still $B2$ ordered but with preferred orientation of some planes at the surface. This is a typical texture effect and points on large grained crystallites. The appearance of small, superstructure reflections in $Co_2Cr_{0.6}Fe_{0.4}Al$ point on additional disorder, most probably caused by oxidation.

As already mentioned above, some types of disorder cannot be detected easily by X-ray powder diffraction as the scattering coefficients of Co and Cr are very similar. The same applies for neutron diffraction. Due to the nearly equal scattering length of Cr and Al, in particular, it is not possible to distinguish between ordered $L2_1$ and disordered $B2$ structures. However, a combination of both methods may give the designated informations about the long range structure of $Co_2Cr_{1-x}Fe_xAl$. The results of the pow-
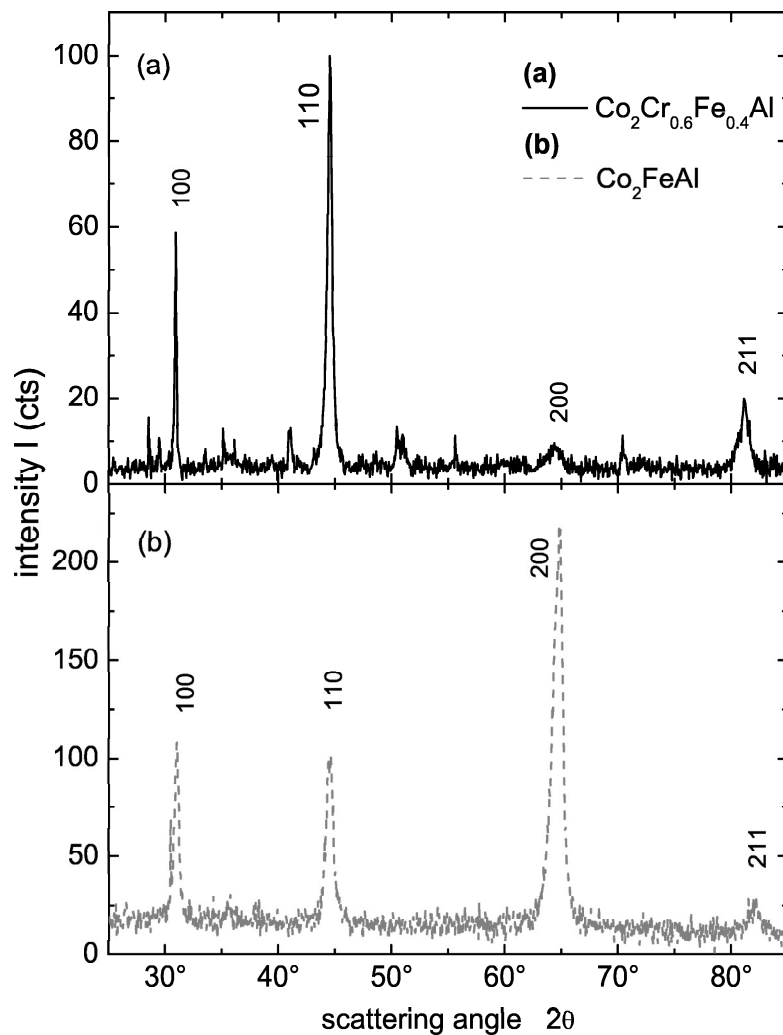
Figure 5.2: XRD from the surface of $Co_2Cr_{1-x}Fe_xAl$.
Surface sensitive XRD measurement of $Co_2Cr_{0.6}Fe_{0.4}Al$ (a) and Co_2FeAl (b) excited Cu K_α radiation. Note the different intensity scales in (a,b).
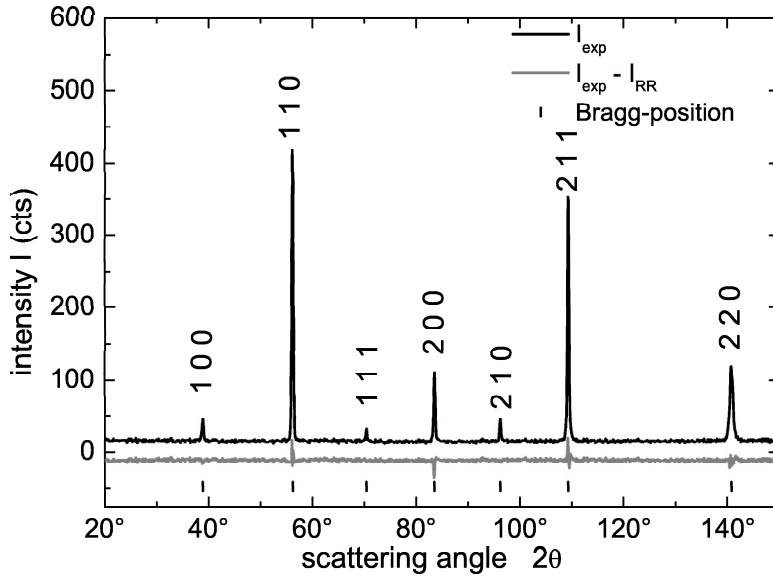
Figure 5.3: Neutron diffraction from $Co_2Cr_{0.6}Fe_{0.4}Al$.
Shown are the measured intensity (I_{exp}) and the difference compared to the Rietveld refinement (I_{RR}). Vertical bars indicate the Bragg positions of the expected diffraction reflections.

der neutron diffraction from $Co_2Cr_{0.6}Fe_{0.4}Al$ are displayed in Figure 5.3. As mentoined above, this diffractogram gives no hint on $L2_1$ ordering or $B2$-type disorder due to the similar scattering coefficients for Cr and Al for neutron diffraction. The $B2$ structure was also used to refine the crystal structure with the neutron diffraction data with the Rietveld method. The magnetic structure was not refined. The occupancy of Cr and Fe were co-refined, while the occupancy of Co and Al were fixed. The Cr to Fe ratio was estimated to be 0.6:0.4, this value was also confirmed with the refinement. The lattice constant was determined to be 2.866 Å, which is in agreement with the XRD data. The obtained R_{Bragg}-value is 3.62 and the R_F-value is 2.78.

In summary, both methods to investigate the long range order in $Co_2Cr_{1-x}Fe_xAl$ clearly point on well ordered $B2$ structure. In all cases it was possible to fit the $B2$ structure with very satisfying results (R_{Bragg}-value $\approx 3-5$). It also reveals, that the mixed compounds show the right stoichiometry.

5.2.2 Extended X-ray Absorption Fine Structure.

Investigations on disorder effects regarding the long range order may not lead to satisfying results due to the similar scattering coefficients for Co, Cr and Fe for X-ray diffraction and for Cr and Al for neutrons. Thus, short range order measurements were

performed using the EXAFS method. The absorption spectra $\mu(E)$ were taken at the Cr, Fe and Co K-edges. The resulting normalised absorption spectra $\mu(E)$ for Co_2CrAl are shown in Figure 5.4.

As the $B2$ structure was verified from XRD as well as from neutron diffraction, $B2$-type structure was used to analyse the EXAFS data. The EXAFS method depends on the scattering of the photoelectron on neighbour atoms. So, the first co-ordination shell is well described with a CsCl-lattice with Co in the center surrounded by Cr/Fe and Al. The second co-ordination shell has to be modelled by four different CsCl lattices all contributing with the factor 0.25. The lattice constant in the $B2$ structure is reduced to a = 2.86 Å. All single scattering (SS) paths were varied independently. Collinear multiple scattering (MS) paths were parametrised in terms of the SS paths with the same starting and endpoints.

In Figure 5.4 (b-d,f-h) the $B2$ fitting results in R space for Co_2CrAl bulk sample can be seen. It shows the magnitude of the Fourier transformation as well as its real and imaginary parts. The radial distribution function $\chi(R)$ is generated by forward Fourier transformation of the EXAFS spectra after background subtraction. It is given as function of the effective distance R. This effective distance R includes both the nearest neighbour distance kR_j and the scattering phase shift δ_j ($kR_j + \delta_j$). In particular the first co-ordination shell of the real and imaginary parts fit very well to the data. The fits were performed using the model described above and led to satisfying results with R-values: $R_F = 0.06$ for Co and $R_F = 0.023$ for Cr. The obtained values for the passive electron reduction factor S_0^2 are 0.730 for Co and 0.874 for Cr. Both ΔR were physically reasonable (0.008 for Co and -0.016 for Cr) as well as the E_0 values (6.582 for Co and 9.987 for Cr). The σ^2 values for the different paths are throughout small (between 0.002 and 0.02).

The same fitting procedure as for Co_2CrAl was performed for Co_2FeAl. Figure 5.5 shows the normalised absorption spectra (a,e), the magnitude of the Fourier transformation (b,f) and its real (c,g) and imaginary parts (d,h) for the Fe and Co edges of Co_2FeAl. As can be seen from Figure 5.17, the fittings are in very good agreement with the data. The R-values: $R_F = 0.015$ for Co and $R_F = 0.019$ for Fe. The passive electron reduction factor S_0^2 are 0.784 for Co and 0.967 for Fe, while the ΔR were -0.039 for Co and -0.061 for Fe. The E_0 values were assigned to be 4.97 for Co and -1.463 for Fe. The σ^2 values for the different paths are throughout small (between 0.002 and 0.008). The Fe as well as the Co edge show no additional feature at about 1.4 - 1.6 eV indicating any oxidation.

Both ternary end members of the doping serie were successfully fitted with a $B2$-type model. So, the EXAFS data are in accordance with the long range order measurements.

The parameter range for the Cr, Fe mixed compounds with B2 structure are, however, too complex for any reasonable fitting process. Therefore, only a qualitative analysis for the quaternary compounds are given. Figure 5.6 as well as Figure 5.7 compare the EXAFS measurements taken from $Co_2Cr_{0.6}Fe_{0.4}Al$ powder and bulk samples.

Figure 5.6 shows the absorption spectra taken at the Cr, Fe and Co edges of $Co_2Cr_{0.6}Fe_{0.4}Al$. The dots represent the measurements on powder sample, while the line shows the spectra taken on bulk samples. The absorption $\mu(E)$ at the Cr edge differs
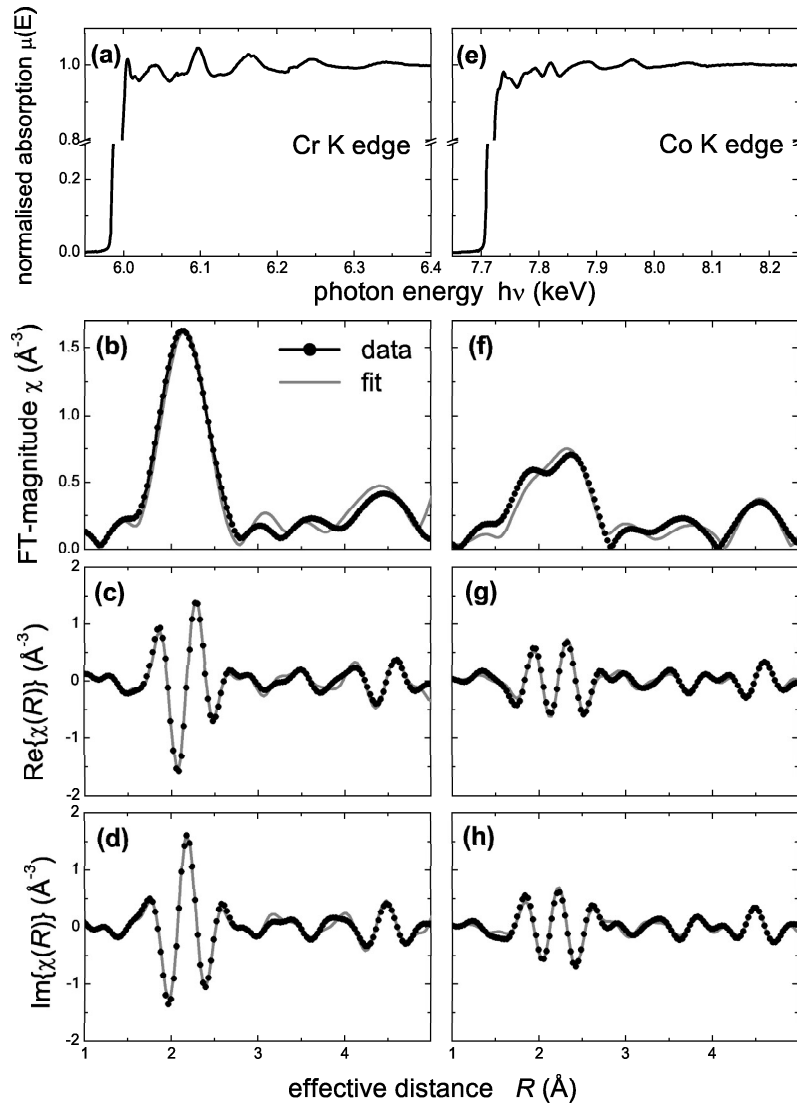
Figure 5.4: EXAFS of Co_2CrAl measured on bulk sample.
Shown are the site resolved results of the EXAFS data taken at the Cr (a-d) and Co (e-h) K edges. Displayed are the normalised absorption spectra (a,e), the Fourier transformation (b,f) and its real (c,g) and imaginary part (d,h).
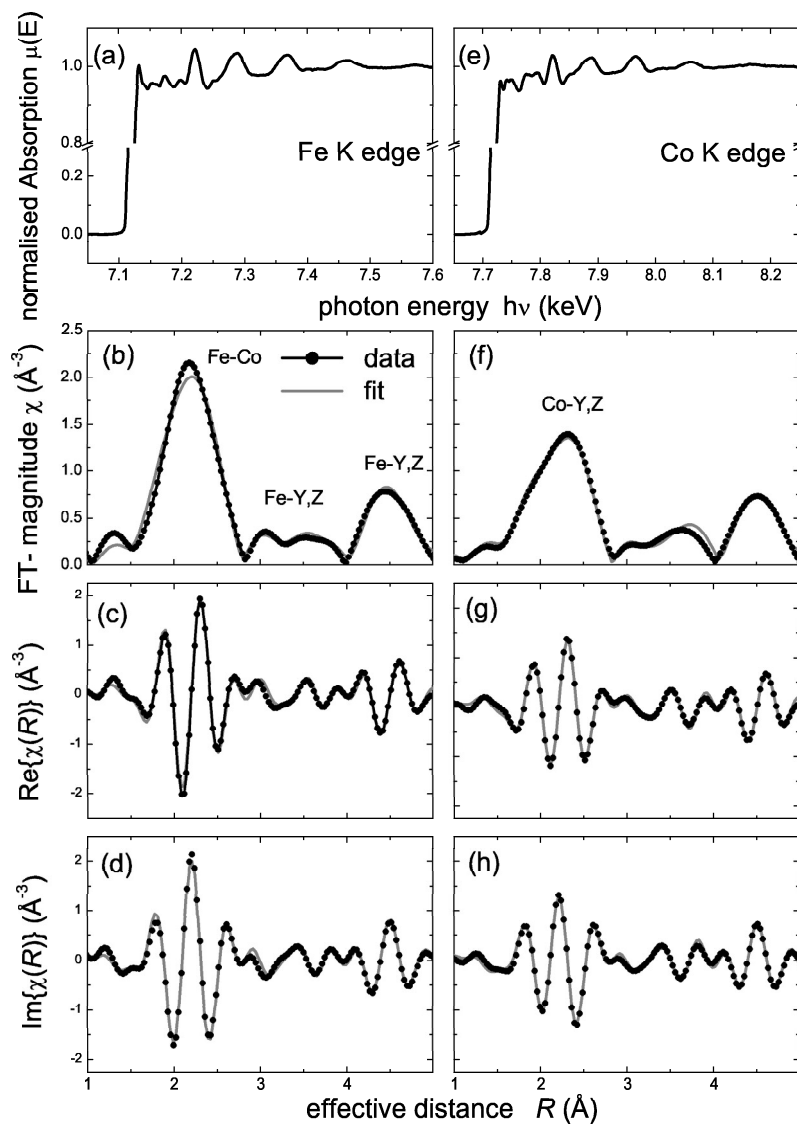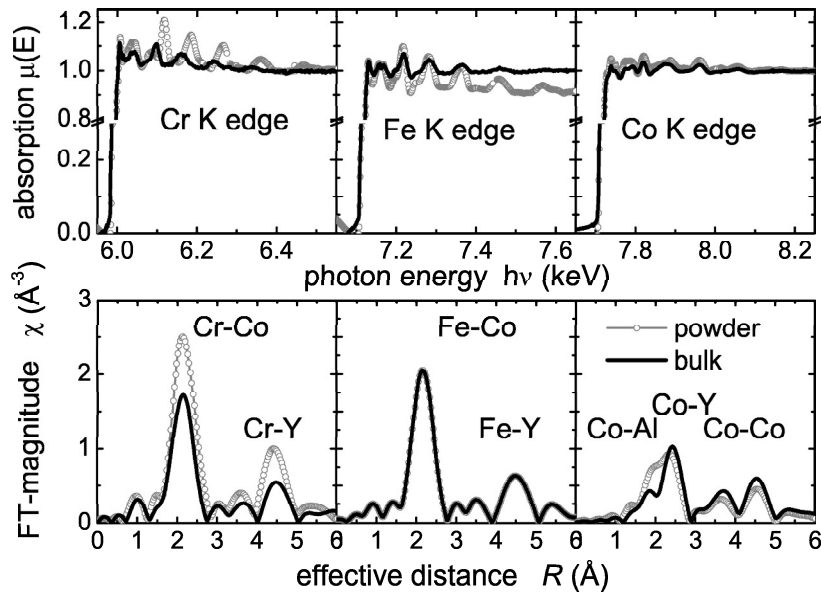
Figure 5.5: EXAFS of Co_2FeAl measured on bulk sample.
Shown are the site resolved results of the EXAFS data taken at the Fe (a-d) and Co (e-h)
K edges. Displayed are the normalised absorption spectra (a,e), the Fourier transformation
(b,f) and its real (c,g) and imaginary part (d,h).

Figure 5.6: EXAFS results of $Co_2Cr_{0.6}Fe_{0.4}Al$ comparing powder and bulk.
Spectra taken at the Cr, Fe, and Co K edges are compared for powder and bulk samples.

dramatically for the powder and bulk spectra at the different edges. The energy shift of the oscillating part of $\mu(E)$ is revealed in $\chi(R)$ as an additional structure at $R = 1.5$ Å. This additional feature is most probably caused by the selective oxidation of Cr in the compound. This difference also shows up in the $\chi(k)$ spectrum as well as in the real and imaginary parts of the Fourier transformation (Figure 5.7).

The radial distribution function $\chi(R)$ is generated by forward Fourier transformation of the EXAFS spectra after background subtraction. It is given as function of the effective distance R. The peak of $\chi(R)$ for the first co-ordination shell of Co at $1.95 Å$ exhibits a clear splitting for the bulk sample and a shoulder for the powder sample although the distance between these atoms and the Co is the same. The reason lies in the the different scattering phases of Cr, Fe and Al. The high intensity of $\chi(R)$ in the first co-ordination shell of Fe and Cr points on the cubic environment consisting of eight Co atoms. On the other side, a Co atom is surrounded by four atoms Cr or Fe and Al each. Therefore, the ratios of the intensities for $\chi(R)$ for Cr and Fe to Co are 1:2, regarding, that the back scattering factors and phases for Cr, Fe and Co are quite similar but that of Al is different. These differences occur also in $\chi(R)$ after Fourier transformation (see Figure 5.6). The effective radius for the first co-ordination shell of Cr, consisting always of eight Co atoms, is the same in powder and bulk. All next neighbour shells are clearly shifted in R by about 1% to larger distances pointing on a different neighbourhood for Cr in powder and bulk samples.

At the Fe edge, neither the absorption spectrum nor the radial distribution function
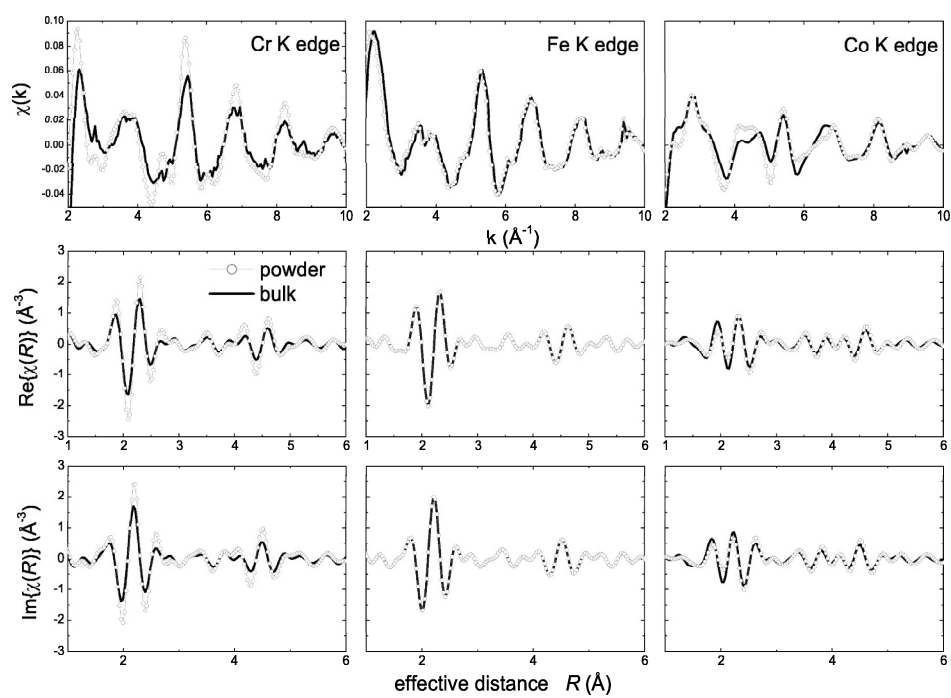
Figure 5.7: EXAFS results of $Co_2Cr_{0.6}Fe_{0.4}Al$.
        Shown are $\chi(k)$ and the real and imaginary parts of the Fourier transformation.

exhibit dramatic changes when changing from powder to bulk samples. In particular $\chi(k)$ and the real and imaginary parts of the Fourier transformation reveal no difference in powder and bulk for the Fe edge, as can be seen in Figure 5.7. The only difference between powder and bulk spectra are the different intensities in the absorption spectra $\mu(E)$ and the FT-magnitude as a function of R (Figure 5.6, mainly caused by the different methods of data collection, transmission or TEY). The oscillatory part, however, stays unaffected, which can be seen from Figure 5.7. It follows, that the co-ordination of Fe is the same in powder and bulk.

The Co absorption spectrum also shows only different intensities. This difference in intensity leads here to a different weight of the structures at different effective distances for the first co-ordination shell in Co. Note that the splitting of the peak for the first co-ordination shell of Co appears clearly in the powder spectrum only. This splitting arises from the different scattering phases of Fe/Cr and Al, although the distance between these atoms and the Co is the same. The subsequent peaks are not altered in $\chi(R)$. Also the the real and imaginary parts of the Fourier transformation reveal no difference comparing powder and bulk material. The $\chi(k)$ is also only altered in intensity. This means that Co has a different first co-ordination shell in powder and bulk samples whereas the next neighbour shells are the same.

One has to account that both, surface and bulk, contribute in the analysis of spectra obtained by the total electron yield method. As known from the XRD measurements, the surface shows no ordered $B2$ structure while the bulk is well $B2$ ordered. In the total electron yield method these two parts can not be separated easily. This means that the EXAFS signal obtained from the discs has to reveal a different structure in the different samples, as is clearly seen from Figure 5.6 and Figure 5.7.

As mentioned above, only the ternary end members of the quaternary series can be modelled.

5.2.3 Mößbauer Spectroscopy.

Mößbauer spectroscopy was performed in order to clarify the magnetic state of Fe atoms in $Co_2Cr_{0.6}Fe_{0.4}Al$ to compare bulk and surface properties. Figure 5.8 shows the resonance effect in percent of the absorption as a function of the Doppler velocity of the Mößbauer source.

CEMS studies of bulk samples based on $Co_2Cr_{0.6}Fe_{0.4}Al$ revealed unusual sensitivity of magnetic properties of this material to the disordering effects. Figure 5.8(a) shows the transmission spectrum of a powdered $Co_2Cr_{0.6}Fe_{0.4}Al$ sample. It comprises a sextet subspectrum with $H_{hf} = 22.6 \times 10^6$ A/m and a nonmagnetic central line. In temperature-dependent CEMS measurements it was found that the relative intensity of the nonmagnetic component decreases as temperature decreases (Figure 5.8 (b) and (c)). However, CEMS measurements revealed no influence on the central line of the external field of 2.4×10^6 A/m. This fact excludes a superparamagnetic nature of the central line. Furthermore, it was found that rough polishing with a sand paper destroys the magnetic ordering of the surface in depth of ca. 100 nm. Figure 5.8(a) demonstrates the surface spectrum after rough polishing. The intensity of the paramagnetic component
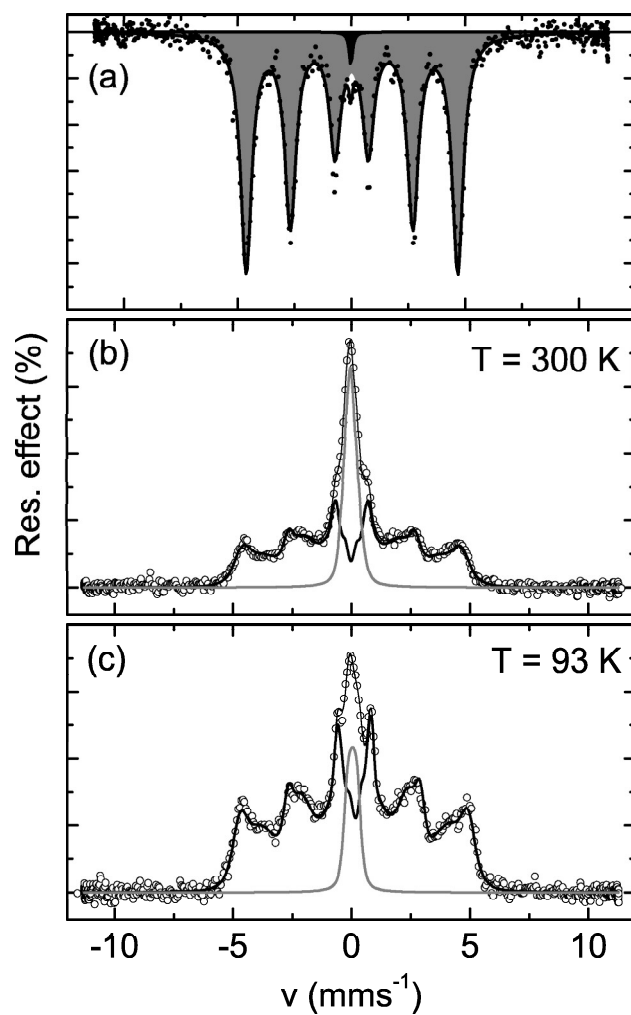
Figure 5.8: Mößbauer spectroscopy of $Co_2Cr_{0.6}Fe_{0.4}Al$.
Shown are the ^{57}Fe Mößbauer spectrum measured in transmission geometry (a) and the CEMS spectra at 300 K (b) and at 93 K (c).
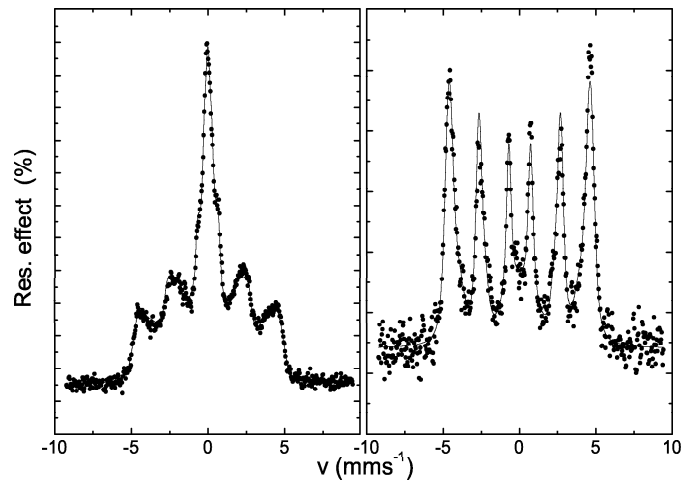
Figure 5.9: CEMS Mößbauer spectroscopy of $Co_2Cr_{0.6}Fe_{0.4}Al$ bulk material.
Shown are the ^{57}Fe Mößbauer spectrum measured after rough polishing (a) and fine polishing (b).

attains almost 40%. Subsequent polishing of the sample surface leads to vanishing of the paramagnetic component in favor of the magnetic subspectrum (Figure 5.8(b)), which can be interpreted applying a hyperfine fields distribution model.

5.2.4 Chemical Analysis.

ESCA was used to investigate the sample composition. The photoemission spectra shown in Figure 5.10 reveal the presence of oxygen in both powder and bulk even after 45 min of sputtering. However, the oxygen content is much higher in powder than in bulk material. This result can be understood regarding the much larger corroding surface in powders. Small amounts of carbon are found in powder as well as in bulk samples. AES depth profiling showed that the oxygen is still present in a depth of about 500 Å. The presence of oxygen may cause a structural transition in this material. The observed oxygen contamination was more pronounced for Cr rich compounds compared to Fe rich ones. This may explain why disorder and too low magnetic moments are found particularly in the high Cr content region. It was also found that compounds with Z=Si are much less sensitive to oxygen compared to the ones with Z=Al. As seen from XAS measurements in particular the Cr seems to oxidise [28, 38, 39, 40] The metal - oxygen bond enthalpy is larger for Cr (430 kJ/mol) than for Fe (400 kJ/mol) and Co (385 kJ/mol). Thus, Cr is selectively oxidised whereas the majority of Co and Fe remains in a metallic state. The information depth of XAS involves a surface layer of $1\ldots2$ nm thickness, i.e. 2 to 4 unit cells. Therefore, the selective oxidation of Cr involves a surface segregation process, which at least partially destroys the stoichiometry of these Heusler compounds in the surface region. From its chemical reactivity (Al-O bond enthalpy 511 kJ/mol) one might
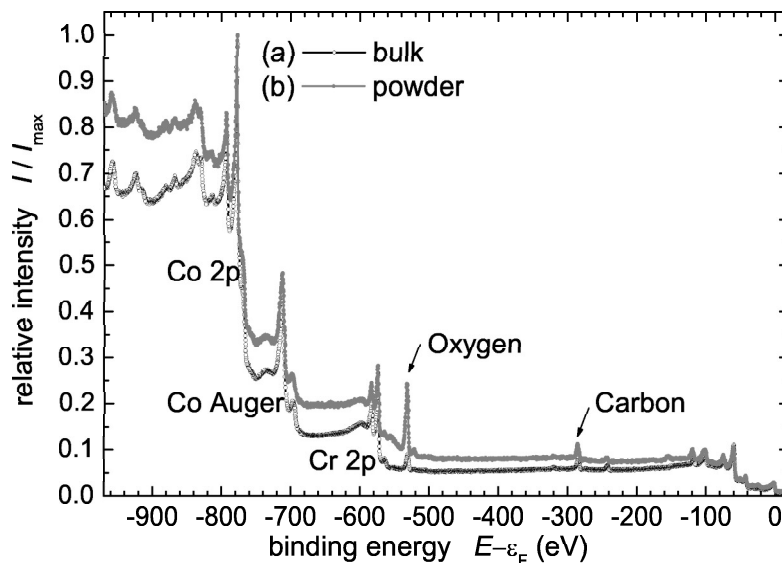
Figure 5.10: Photoemission spectra of Co_2CrAl in bulk and powder samples.

assume that Al is oxidised as well. Nevertheless, the experiment gave no advice on the oxidation of Al.

5.3 Magnetic Properties.

Figure 5.11 shows magnetisation loops as measured by SQUID magnetometry. The coercive fields as well as the remanence are very small for all investigated Heusler compounds The remanence observed for both Heusler compounds is also very small. The magnetization cycle is almost reversible. This indicates that both Heusler compounds are soft magnetic materials, which is common to Heusler compounds [96]. It may be caused by magneto-strictive interactions between adjacent grains. If magneto-striction along the easy axis is not zero, elastic interactions between the grains lead to additional conditions for the domain structure which in turn reduce the remanence below the value of 80% expected for independent randomly oriented grains [122]. Note, that the magnetisation loops are not corrected for the demagnetisation field arising from the spherical shape of the sample.

The saturation magnetisation values measured in saturation are $m(300 \text{ K}) = 3.25$ μ_B for $Co_2Cr_{0.6}Fe_{0.4}Al$ and $m(300 \text{ K}) = 5.20$ μ_B for Co_2FeAl. Slightly higher values were measured at low temperatures, i.e. $m(4 \text{ K}) = 3.49$ μ_B for $Co_2Cr_{0.6}Fe_{0.4}Al$ and $m(4 \text{ K} = 5.29$ μ_B for Co_2FeAl. The magnetisation at room temperature for $Co_2Cr_{0.6}Fe_{0.4}Al$ is slightly larger than for similar samples measured previously [39, 40] ($m(300K) = 3.2$ μ_B).
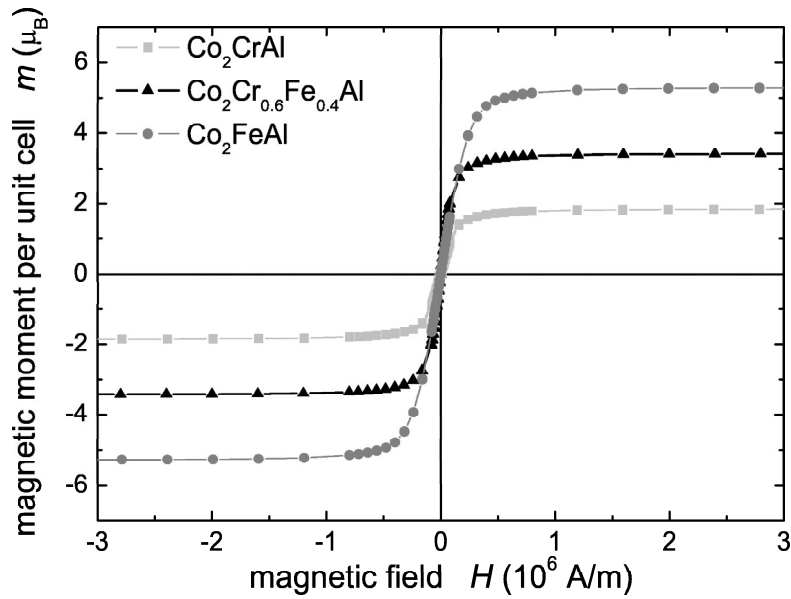
Figure 5.11: Magnetisation curves measured by SQUID for the Heusler compounds Co_2CrAl (dark grey), $Co_2Cr_{0.6}Fe_{0.4}Al$ (black) and Co_2FeAl (bright grey).

While the latter value for Co_2FeAl is in agreement with calculations (5.0 μ_B [28]) considering that orbital magnetic moments are not included in the theoretical value, the measured magnetic moment for $Co_2Cr_{0.6}Fe_{0.4}Al$ is significantly smaller than predicted by theory (3.8 μ_B [28]). Element specific moments measured by XMCD [39, 40] indicate that the reduced magnetic moment is mainly due to the too small magnetic moment at the Cr site.

Thus, a comprehensive analysis of the site specific magnetic moments as revealed by XMCD is necessary.

5.3.1 Calculated Properties of $Co_2Cr_{1-x}Fe_xAl$.

The electronic structure of the pure and doped alloys will be discussed in the following. First, the electronic structure of the ordered alloys are presented followed by the results for disordered alloys. Both include a more specific discussion of the magnetic properties by means of measured and calculated magnetic moments. A band structure in the usual definition has no meaning for alloys with random disorder, due to the lack of periodicity. Therefore, only the integrated quantities will be discussed here. Indeed, the magnetic moments depend more directly on the DOS rather than on the particular form of the dispersion of the electronic bands.
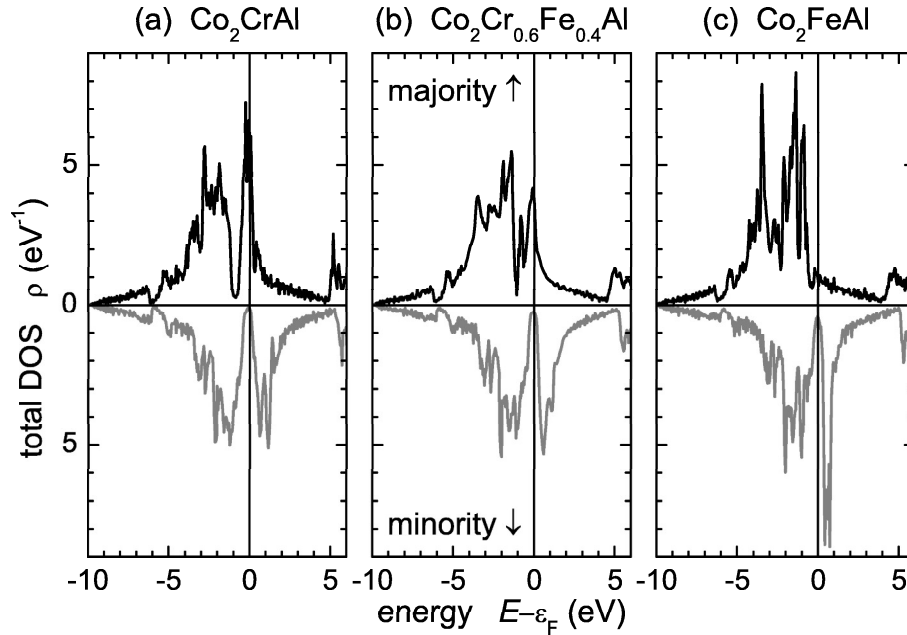
Figure 5.12: Density of states of $Co_2Cr_{1-x}Fe_xAl$ ($x = 0, 0.4, 1$).
(Note that the minority states are shown on a negative scale.)

Electronic and Magnetic Structure of $L2_1$ Ordered Alloys.

First, the electronic structure for the $L2_1$ ordered ternary compounds was calculated. The resulting density of states (DOS) of Co_2CrAl and Co_2FeAl is shown in Fig.5.12(a,c). These are the end members of the quaternary series of alloys. In the next step the electronic structure for the $L2_1$ ordered alloys $Co_2Cr_{1-x}Fe_xAl$ was calculated and the result for $x = 0.4$ is compared exemplarily in Figure 5.12(b) to the pure compounds.

The low lying s-bands are visible at about 6 eV to 10 eV below ϵ_F. The d-bands start at about 5.5 eV below ϵ_F. The gap between s- and d-bands is less pronounced compared to non relativistic calculations (see [123]). The majority DOS at the Fermi energy decreases with increasing iron concentration x. The DOS of majority electrons at ϵ_F is a crucial point for spectroscopic methods investigating the spin polarisation, like spin-resolved photoemission. The small, non vanishing DOS in the half-metallic gap of the minority states at ϵ_F emerges mainly from the imaginary part added to the energy when calculating the DOS by means of the Greens function. However, a coupling between majority and minority states is always expected in the full relativistic calculations thus that a pure spin up state is not possible in general. Mavropoulos *et al.* [124, 125] for example discussed the relativistic effects and their influence on the half-metallic gap.

Figure 5.12 reveals that the Fermi energy (ϵ_F) is pinned in the minimum of the density
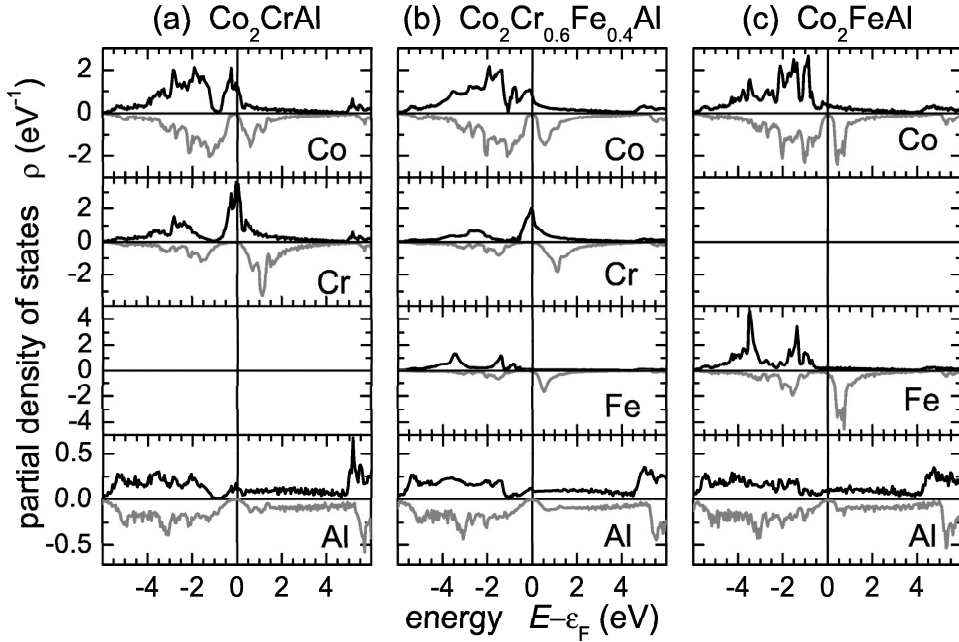
Figure 5.13: Spin resolved partial density of states of Co$_2$Cr$_{1-x}$Fe$_x$Al.
(Note the different scales at the partial DOS, the minority states are shown on a negative scale.)

of the minority states. Further, it is seen that the majority density is shifted with increasing Fe concentration and thus with increasing number of valence electrons. Both together have finally the result that the magnetic moments increase with the number of valence electrons (see below). This is typical for Slater-Pauling behaviour in the case of materials with localised magnetic moments [126, 36, 56, 22]. It is also seen that the majority density is shifted with increasing Fe concentration and thus with increasing number of valence electrons. Both together have finally the result that the magnetic moments increase with the number of valence electrons (see below).

The spin resolved partial DOS (PDOS) is displayed in Figure 5.13. Shown are the partial (site specific) densities for the majority and minority states of Co$_2$Cr$_{1-x}$Fe$_x$Al for $x = 0, 0.4, 1$. In particular, the gap in the minority DOS is better resolved. From the behaviour of the different PDOS depending on the Fe concentration x, it is clear that the electronic structure does not follow a rigid band like model. In particular it can be seen that the Cr PDOS decreases with increasing iron content keeping its shape rather unchanged. In the same way the Fe PDOS increases with x. However, the maxima of the density at the Co sites are clearly shifted away from ϵ_F. The Al PDOS stays rather independent of the Fe content.

From Figure 5.13 it is seen that the high majority DOS at ϵ_F emerges from Cr. Both,

Co and Fe, exhibit only a small majority PDOS at and above ϵ_F. Overall, the change of the majority DOS of $Co_2Cr_{1-x}Fe_xAl$ around ϵ_F can be clearly attributed to the increasing amount of Fe with respect to Cr. The minimum in the minority DOS around ϵ_F is mainly restricted by the shape of the Co PDOS. This indicates that the half-metallic ferromagnetic-like behaviour is mainly characterised by Co. The steep increase of the minority PDOS of Cr and Fe is mainly located in the unoccupied part above ϵ_F.

Doping with Fe does not only change the total DOS but also the PDOS of Co and, in a much less pronounced manner, the one of Cr. In particular, a very small shift of the Cr PDOS causes an additional decrease of majority states at ϵ_F. This shift increases with increasing Fe concentration (as was found from the PDOS with variation of x, not shown here). The energy shift of the PDOS results in a change of the local magnetic moments in particular at the Co sites.

Figure 5.14 compares the measured and the calculated magnetic moments. The calculated total magnetic moment $m_{tot} = m_s + m_l$ depends linearly on the composition x and follows the Slater-Pauling rule [37, 56, 22]. The measured total moments as determined by SQUID magnetometry at 5 K are smaller compared to the calculated values in particular for low Fe (or equivalently high Cr) content. This behaviour will be discussed in the next section about disorder.

Site specific spin (m_s) and orbital (m_l) magnetic moments were determined for $x = 0, 0.4, 1$ from XMCD measurements at the $L_{3,2}$ edges of Cr, Fe, and Co. Details of the spectroscopy experiments are reported below. The values were found from a sum rule analysis neglecting the magnetic dipole term [38]. The calculated spin magnetic moments at the Co sites increase with increasing Fe concentration x as result of the shift of the majority PDOS of Co. The calculated spin moments at the Fe sites decrease slightly with increasing x. The principal dependence of the measured Co and Fe spin moments on x is the same as in the calculation. However, the changes in the measured moments are stronger. The calculated Al spin moment is negative and very small. It is induced by the surrounding polarised atoms. Obviously, the measured spin magnetic moments at the Cr sites are smaller compared to the calculated ones. This finally causes the too small total moment observed by SQUID magnetometry. The calculated orbital magnetic moments increase with x at the Co sites by a factor of 4 and are nearly constant at the Fe sites. The calculated Cr orbital moments are very small and change sign at $x = 1/2$. In contrast, the measured orbital moments are throughout larger. Both experiment and calculation exhibit, however, the same trend for m_l.

Most evidently, the calculated ratios between orbital m_l and spin m_s magnetic moments are much smaller than the experimental values. For Cr, a vanishing of the orbital momentum is expected, as observed in the calculation. On the other hand, the determination of the Cr moments at the $L_{3,2}$ edges is complicated due to the partial overlap of the lines, what may cause the observation (see spectra shown below in Figure 5.15). The too low values of m_l at Co and Fe sites cannot be explained that way. However, it is clear that the usual Hamiltonian used in LSDA contains a spin dependent coupling only. Thus the orbital part of the moment arises via spin-orbit interaction only, or in words of the full relativistic case from the coupling of the large and the small components of the wave functions. This already leads in the case of pure Co and Fe metal to
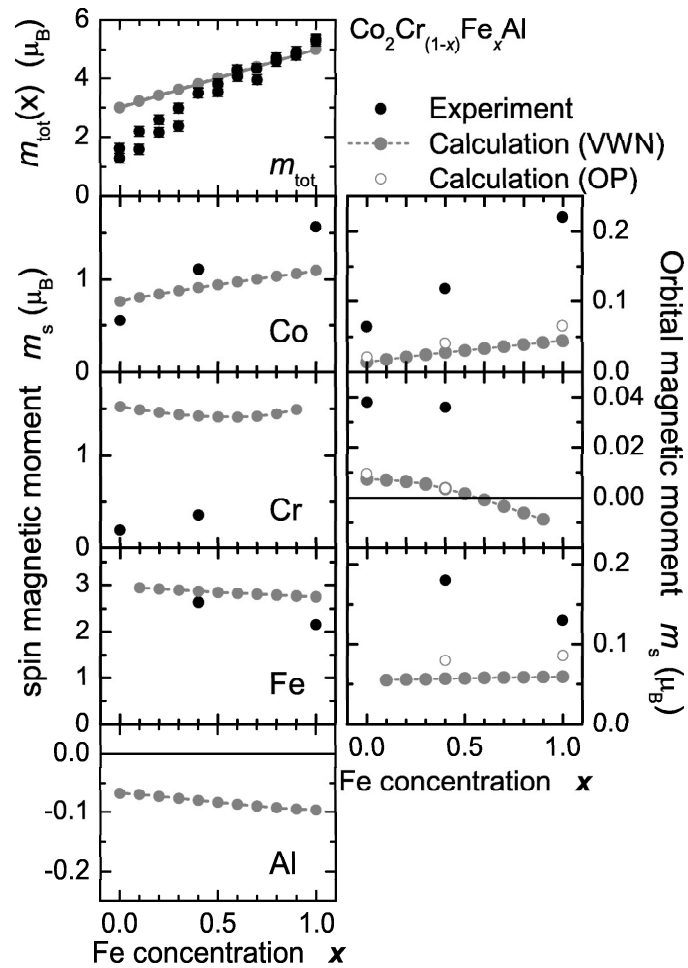
Figure 5.14: Magnetic moments in $Co_2Cr_{1-x}Fe_xAl$.
The experimental uncertainty for a single measurement is within the width of the symbols as assigned at m_{tot}.

Structure	$x = 0$			$x = 0.4$				$x = 1$		
	Co	Cr	tot	Co	Cr	Fe	tot	Co	Fe	tot
$L2_1$	0.77	1.53	3.01	0.94	1.42	2.92	3.82	1.14	2.81	5.00
$B2$	0.75	1.46	2.92	0.57	-1.12	2.95	1.61	1.07	2.91	4.95
$A2$	0.22	1.25	2.68	1.44	0.19	2.24	3.83	1.59	2.38	5.46
Exp.	0.55	0.19	1.3	1.11	0.36	2.64	3.49	1.57	2.15	5.29

Table 5.1: Magnetic moments in $Co_2Cr_{1-x}Fe_xAl$.
Given are the site specific moments per atom and the overall magnetic moment per unit cell, both in multiples of the Bohr magneton (μ_B). The overall magnetic moments for the disordered structures are converted to fit those of the $L2_1$ cell in number of atoms.

an underestimation of the orbital moments. One way to overcome that problem is the inclusion of the Brooks orbital polarisation [127] term (OP) in the Hamiltonian [128]. The use of the OP term increases the orbital moments slightly as shown in Figure 5.14, but evidently, the calculated values of the orbital magnetic moments are still smaller by a factor of up to 5 compared to the experimental values. The spin and total moments stayed in the same order as in pure LSDA. The observation of high orbital moments may point on additional orbital polarisation effects or correlation being not respected in LSDA.

The findings of the full relativistic calculations are throughout compatible to those made in non-relativistic calculations using ordered compounds [22]. Comparing the random alloy $Co_2Cr_{0.6}Fe_{0.4}Al$ and the nearly iso-electronic, ordered compound $Co_4CrFeAl_2$ [22], it is found that there are no major differences between CPA and supercell approximation calculations for the materials investigated here. The non rigid band like character of the electronic structure upon Fe doping is revealed in both methods. The band gaps in the minority densities are smaller here due to the additional splitting of bands caused by the spin-orbit interaction rather than by properties of the CPA scheme, as is seen from the pure compounds.

Random Alloys with Disorder.

Table 5.1 shows the results of the calculations for the magnetic moment in the well ordered ($L2_1$), partially disordered ($B2$), and completely disordered ($A2$) alloy $Co_2Cr_{1-x}Fe_xAl$ in comparison to the experimental values.

Co_2CrAl and Co_2FeAl exhibit a total moment of 3.0 μ_B and 5.0 μ_B in $L2_1$, respectively. These values correspond to those expected from the Slater-Pauling rule for the moment in the half-metallic ferromagnetic ground state. The magnetic moment of correctly ordered $Co_2Cr_{0.6}Fe_{0.4}Al$ is close to the value of 3.8 μ_B expected for a half-metallic ferromagnetic ground state. From the calculations it is expected that the total magnetic moment of the $B2$ disordered compounds is lower compared to the one in the $L2_1$ structure.

The calculations for $B2$ or $A2$ disorder are not able to explain the too low value of the magnetic moment found experimentally for Co_2CrAl. A reduction of the overall

		8c	4a	4b	mean
	Co	1.08	1.86	1.98	1.25
20%$A2$	Cr	-0.90	1.33	1.20	0.87
	Fe	0.96	2.79	2.87	2.43

Table 5.2: Magnetic moments in disordered $Co_2Cr_{0.6}Fe_{0.4}Al$.
All calculated values are in μ_B per atom. The mean value is weighted by the disorder site occupation factors.

moment caused by an anti-ferromagnetic order of the Cr atoms could not be verified by the calculations for these structure types. Therefore, calculations were also performed for other types of disorder. In the DO_3-type disordered alloy the Co and Cr atoms in 8c and 4b positions of the $L2_1$ structure are mixed. The calculations revealed an overall moment of 2.0 μ_B. The moment of the Co atoms at the two different sites are 0.86 μ_B and 1.51 μ_B. The moments of the Cr atoms are aligned anti-parallel with respect to each other and amount to -0.41 μ_B and $+0.44$ μ_B at 8c and 4b sites, respectively. Exchange of only one of the Co atoms with the Cr atom leads to the X structure [82]. In this case the calculations revealed an anti-parallel alignment of the Cr moments (-0.93 μ_B) with respect to the Co moments (0.8 μ_B and 1.11 μ_B) with a resulting overall moment of only 0.95 μ_B in the cell. From this approach, a tendency to ferrimagnetic order is concluded if Cr and Co atoms change sites resulting in a lower magnetic moment. It is worthwhile to note that disorder of this type closes the gap in the minority DOS and the half-metallic character is lost.

The measured overall magnetic moment of $Co_2Cr_{0.6}Fe_{0.4}Al$ is smaller compared to the calculated one for the ordered compound. Inspecting the site resolved moments one finds that the Co moment is slightly enhanced whereas the Cr and Fe moments are lowered compared to the $L2_1$ calculation. Such type of behaviour is also observed in the calculation for $A2$ disorder, but less pronounced. Thus, it is obvious to assume a partial disorder for this type of samples. It is interesting to note that the calculations revealed a ferrimagnetic ground state for $B2$ disordered $Co_2Cr_{0.6}Fe_{0.4}Al$, indeed, in contrast to the experiment where the Cr moment was small but aligned parallelly to the Co moment.

The results from a calculation for 20% disordered systems are compared in Tab.5.2. For (80%$L2_1$+20%$A2$), the Co and Fe moments are larger in the $4a$ and $4b$ positions compared to the $8c$ position. Most evidently, the Cr moment exhibits an anti-parallel alignment in the $8c$ position. The total magnetic moment in the cell is 3.96 μ_B and thus larger than the experimentally observed value.

In the experiment at Co_2FeAl, a larger total magnetic moment was observed in comparison to the expectation from the Slater-Pauling rule. At the same time the Co moment was enhanced and the Fe moment lowered compared to the calculations for $L2_1$. Comparing the values calculated for different type of disorder, one finds easily that the experimental values coincide with those expected for $A2$ type disorder. This means that the sample investigated by XMCD was to a large amount completely disordered.
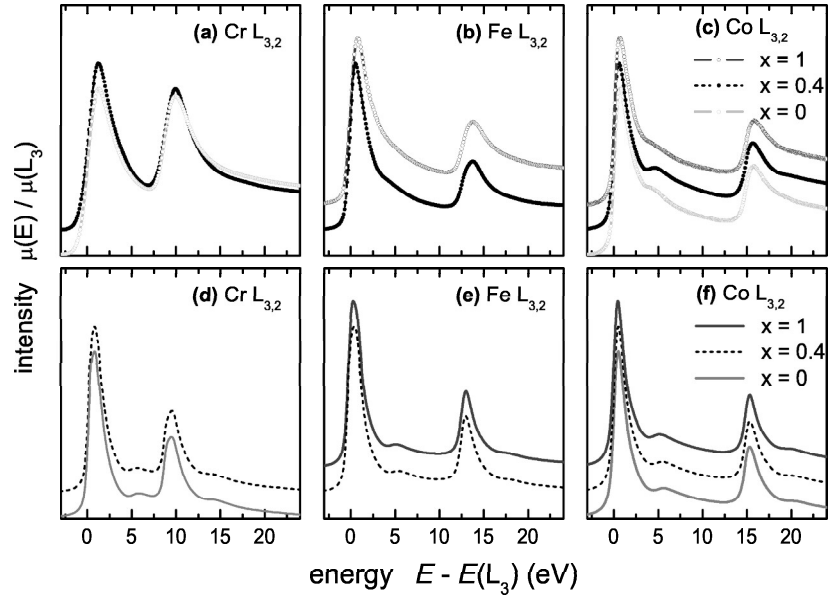
Figure 5.15: X-ray absorption spectra at the $L_{3,2}$ edges of Cr, Fe, and Co in
$Co_2Cr_{1-x}Fe_xAl$.
(a) to (c) show the experimental and (d) to (f) the calculated spectra for $x = 0, 0.4, 1$.
The energy scales of the spectra are shifted with respect to the steepest point of the
spectra (maximum of the derivative). The intensity scales are normalised to the maxima
at the L_3 edges and shifted for sake of clarity.

5.3.2 Spectroscopic Properties of $Co_2Cr_{0.6}Fe_{0.4}Al.$

In the following, results from spectroscopic experiments will be presented and compared
to the calculated properties. The discussion in the two subsections about photoabsorp-
tion and photoemission will be focused on the mixed compound $Co_2Cr_{0.6}Fe_{0.4}Al$.

Photoabsorption and XMCD.

X-ray absorption spectroscopy probes the unoccupied density of states above the Fermi
energy. For the resonant excitation of the $2p$-states of the $3d$ transition metals the
transition probability is proportional to the density of final states resulting from the $3d$
and $4s$ holes. The spectra, consisting mainly of the L_3 ($2p_{3/2}$) and L_2 ($2p_{1/2}$) white
lines (see Figure 5.15), reflect the high density of unoccupied states resulting from the
$3d$ electrons.

Figure 5.15 compares measured and calculated absorption spectra at the $L_{3,2}$ edges
of Cr, Fe, and Co in $Co_2Cr_{1-x}Fe_xAl$. The monochromator resolution was set to 50 meV
for the spectra in (a)-(c). The spectra (d)-(f) were calculated for $L2_1$ structures using
a lifetime broadening of 136 meV. The measured white lines at both Cr edges are con-
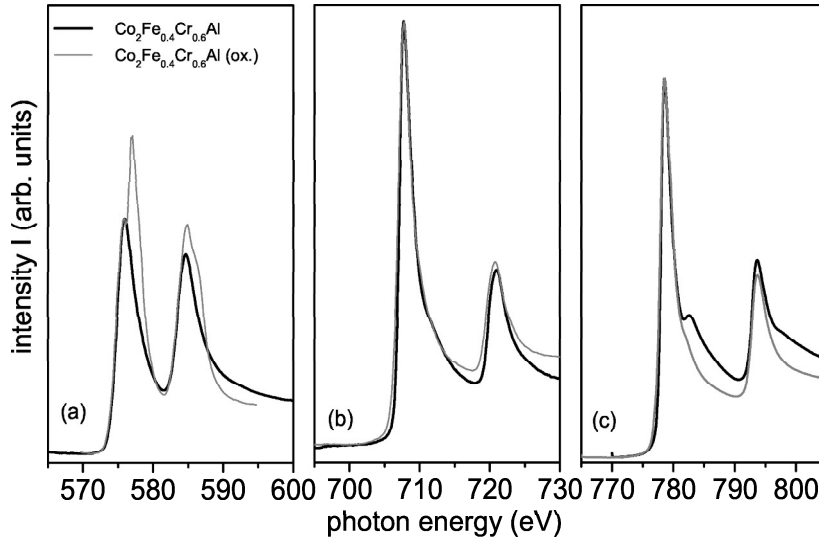
Figure 5.16: XAS spectra for Cr (a), Fe (b), and Co (c) in $Co_2Cr_{0.6}Fe_{0.4}Al$.
XAS spectra for the quenched (black line) sample measured after in-situ cleaning of the surface is compared to XAS spectra obtained for the quenched sample after exposure to air (grey line). Prominent extra peaks at the L_3 and L_2 absorption edges for the exposed sample indicate oxidation. In particular the Cr edge shows strong oxidation.

siderably wider compared to the calculated spectra whereas the width of the Fe and Co white lines are comparable. This points on a shorter lifetime of the holes at the Cr sites. Similarly, the measured L_2 lines of Co and Fe hint on a slightly larger lifetime broadening compared to the L_3 edges. Overall, it is found that the spectra are governed by the lifetime broadening rather the experimental resolution.

The experimental spectrum exhibits a prominent feature at the Co L_3 line for $Co_2Cr_{0.6}Fe_{0.4}Al$, in particular, that is shifted by about 4 eV with respect to the white line. This feature is only weakly revealed for $x = 0$ and $x = 1$ and appears only as weak shoulder in the Fe ($x = 0.4$) spectrum. It is not revealed in the measured Cr spectra what may be partially attributed to the higher lifetime broadening. The same structure occurs in the simulated absorption spectra and can be related to the structural properties. A similar feature is observed for example in fcc Ni but not in bcc Fe or hcp Co. It reflects the onset of the high lying s-bands (see also Figures 5.12, 5.13). Here, its occurrence is characteristic for the highly ordered Heusler compounds. It vanishes for annealed and presumably disordered samples [38] as well as for oxidised samples.

In addition, prominent extra peaks at the L_3 and L_2 absorption edges for the exposed sample indicate oxidation. A clear difference is observed in particular for the Cr XAS (see Figure 5.16(a)) before and after removing the oxide layer. The XAS spectra of the cleaned sample look similar to spectra obtained from metallic Cr samples. Resonant absorption lines are obtained at 575.9 eV and 584.6 eV for the L_3 and L_2 edge, respectively,

with a full width at half maximum (FWHM) of ≈ 3.5 eV, which is characteristic for Cr in the metallic state [129]. Contrarily, the Cr XAS spectrum of the oxidised surface shows two distinct peaks at the L_3 edge (575.9 eV and 577.0 eV) and the peak at the L_2 edge is accompanied by a shoulder. The peak positions and relative intensities are characteristic for the XAS spectrum obtained from Cr_2O_3 [130]. However, no particular features giving advice on half-metallic ferromagnetism are found in the absorption spectra due to the relatively high width of the lines.

Figure 5.16(b) shows the XAS spectra at the Fe $L_{3,2}$ edge for the same set of samples. Both spectra show the resonant absorption lines at 707.7 eV and 721 eV for the L_3 and L_2 edge, respectively, with a FWHM of ≈ 2 eV, similar to the XAS spectra of metallic Fe [131]. In particular, the oxidised sample does not show an additional peak at the L_3 edge, which could be expected at a photon energy shifted by 2 eV to a higher binding energy [132]. A weak shoulder at the L_3 edge at 712 eV ($\Delta\varepsilon \approx 4$ eV) may be recognized for the quenched sample, which is absent for the oxidised sample.

As in the case of Fe, the XAS spectra at the Co $L_{3,2}$ edge (Figure 5.17) shows two prominent resonant peaks corresponding to the L_3 and L_2 component at 778.6 eV and 793.8 eV, similar to XAS spectra observed for metallic Co [131]. The FWHM is approximately 2 eV. No additional peaks can be recognized for the oxidised sample. In particular, no multiple peak structures in the L_3 region were observed as in the case of the Sn-based Heusler alloys Co_2YSn (Y=Ti, Zr, and Nb) [52]. The lack of these many-peak structures cannot be attributed to a limited energy resolution as can be concluded from the steep increase at 778 eV. Instead, it must be explained by a different DOS which indicates a more metallic character of the Co d-band compared to the Co_2YSn alloys. For the quenched sample we observed a pronounced shoulder at the L_3 peak shifted by 4 eV with respect to the maximum to a higher photon energy. A similar structure should be observed in the L_2 region. A less pronounced shoulder can indeed be observed at the L_2 peak. Less sharp structures in the L_2 region can be ascribed to a lifetime broadening effect because the lifetime of the $2p_{1/2}$ core hole is much shorter than the $2p_{3/2}$ core hole due to the Coster-Kronig decay [52].

From the comparison of the XAS spectra of oxidised samples with clean surfaces it is obvious that the 3 elements Cr, Fe and Co react differently when exposed to air. This can be expected, because the metal - oxygen bond enthalpy is larger for Cr (430 kJ/mol) than for Fe (400 kJ/mol) and Co (385 kJ/mol). The strong selectivity, however, is surprising. Cr is selectively oxidised whereas the majority of Co and Fe remains in a metallic state. The information depth of XAS involves a surface layer of $1-2$ nm thickness, i.e. $2-4$ unit cells. Therefore, the selective oxidation of Cr involves a surface segregation process, which at least partially destroys the stoichiometry of the Heusler compound in the surface region. Taking this into account, one may conclude that the near surface region of about $1-2$ nm consists of metallic FeCo alloy mixed by Cr oxide, after exposure to air. From its chemical reactivity (Al-O bond enthalpy 511 kJ/mol) one might assume that Al is oxidised as well. Nevertheless, XPS measurements revealed no oxidation of the Al atoms.

Figure 5.17 compares measured and calculated XMCD spectra for Cr, Fe, and Co in $Co_2Cr_{0.6}Fe_{0.4}Al$. The experimental spectra shown in (a)-(c) were taken at 300K by
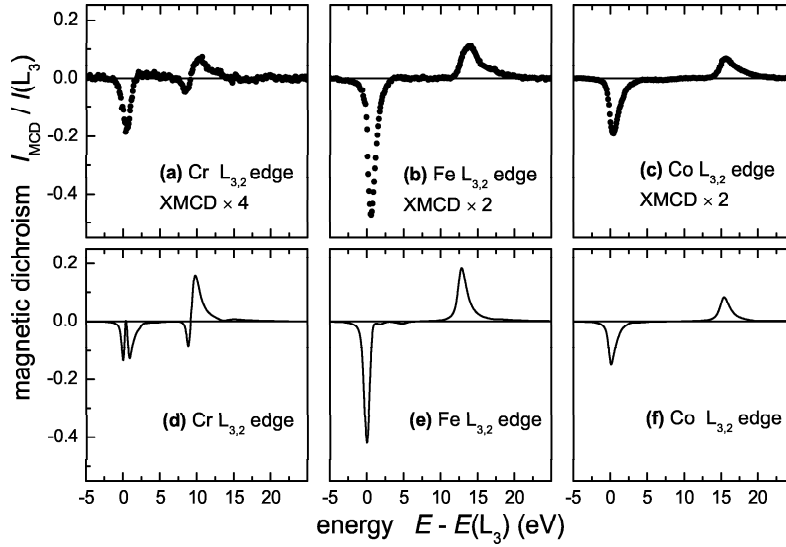
Figure 5.17: XMCD spectra at the $L_{3,2}$ edges of Cr, Fe, and Co in $Co_2Cr_{0.6}Fe_{0.4}Al$.
(a) to (c) show the experimental and (d) to (f) the calculated spectra. The XMCD signal $I_{MCD} = \mu^+ - \mu^-$ is normalised by the maximum intensity at the L_3 edges. For better comparison, the experimental values are multiplied by a factor 2 and both signals at the Cr edges are multiplied by an additional factor 2.

switching a constant induction field of $B_0 = \pm 0.73$ T (for field dependent measurements see [39, 40]). The angle of photon incidence was 70° with a degree of circular polarisation of 85%. The spectra (d)-(f) are calculated for parallel and anti-parallel orientation between magnetisation and photon spin.

The size and shape of the XMCD agree well at the Fe and Co edges comparing experiment (b,c) and calculation (e,f). It is clearly seen from the spectra at the Co edges (c,f) that the structural feature does not contribute to the XMCD signal. The calculated Cr XMCD (d) exhibits a splitting at the L_3 edge that is not resolved in the experimental spectra. However, the change of sign close to the L_2 edge is clearly visible in experimental as well as theoretical spectra. Both, splitting and change of sign, are due to the high density of majority states directly at the Fermi energy and the energetically shifted high density of the minority d-states above the half-metallic gap (compare Figure 5.13).

Figure 5.18 shows the energy dependence of the spin (s_z) and orbital (l_z) densities (polarisation) in $Co_2Cr_{0.6}Fe_{0.4}Al$ as derived from the XMCD and absorption spectra using the sum rules [67]:

$$\frac{d}{dE} \langle s_z \rangle + 7\frac{d}{dE} \langle T_z \rangle \quad \propto 3(\Delta\mu_{L_3} - 2\Delta\mu_{L_2}), \quad (5.1)$$

	m_s	m_l	$7\,T_z$	n_d
Co	0.86	0.042	0.0063	7.62
Cr	1.47	0.005	0.0009	4.68
Fe	2.59	0.082	0.0018	6.51
Al	-0.07	0	0	0.4
$Co_2Cr_{0.6}Fe_{0.4}Al$	3.56	0.12	-	21

Table 5.3: Magnetic moments and dipole operator in $Co_2Cr_{0.6}Fe_{0.4}Al$.
All calculated values are in μ_B per atom. The last column gives the number of occupied d-states per atom that are necessary to calculate the magnetic moments from the sum rule analysis.

$$\frac{d}{dE}\langle l_z\rangle \quad \propto 2(\Delta\mu_{L_3} + \Delta\mu_{L_2}). \tag{5.2}$$

T_z is the z component of the magnetic dipole operator. $\Delta\mu_{L_{3,2}}$ assigns the difference of the absorption signal (μ) for parallel and anti-parallel alignment of photon spin and magnetisation at the L_3 and L_2 edges.

The calculated values for the magnetic dipole operator are given in Table 5.3 and compared to the magnetic moments. All values in Table 5.3 were calculated using the OP scheme. The magnetic dipole term $7T_z$ is in all cases small compared to the spin magnetic moment and thus can safely be neglected in the data analysis.

The experimental polarisation spectra are compared with calculated spectra in Figure 5.18. The Cr XMCD spectrum is particularly interesting because in the disordered areas of the sample the Cr moments may be aligned partially anti-parallel to each other and the magnetic signal cancels out. Therefore, the remaining Cr XMCD contains information from the ordered regions, only. While the agreement between theory and experiment is only moderately well for the XMCD (Figure 5.18(a,d)), the spin and orbital moment densities (Figure 5.17(a,d)) are described remarkably well. The prominent maximum in the spin density at about 1eV above the L_3 edge is clearly revealed. The change of sign close to the Fermi edge is indicative for the large exchange splitting of the Cr $3d$ states. The orbital densities exhibit a change of sign for all elements leading finally to the small orbital moment after integration. The experimental spectra are throughout wider than the calculated ones resulting in higher experimental values for the orbital moments [123]. However, the width of the spin densities fits that of the calculated spectra.

Photoemission.

Using photoemission spectroscopy one obtains information about the occupied electronic states. The dispersion of the bands may be studied by spin and angular resolved UPS. This needs, however, well ordered surfaces of single crystals. For the interpretation one has to take into account that usually the kinetic energy of the photo emitted electrons
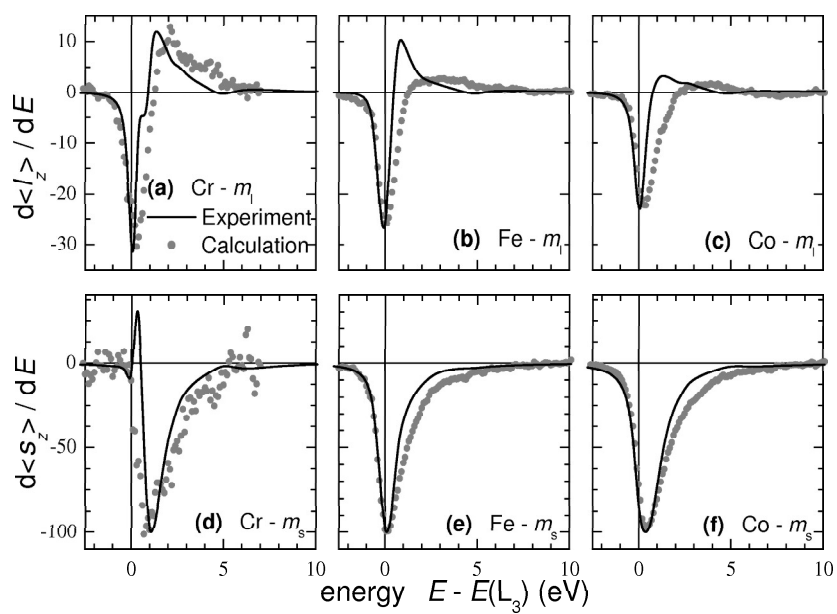
Figure 5.18: Orbital and spin polarisation in $Co_2Cr_{0.6}Fe_{0.4}Al$.
The measured dependencies were scaled to the minima for better comparison with the calculated data.

is in a range where the mean free path is only a few Å and the method therefore mainly shows electronic bands very close to the surface layer.

Using higher photon energy for excitation (and thus kinetic energies of the electrons), it is possible to study the density of states, in particular for polycrystalline samples. Making use of resonant excitation one expects to become more bulk sensitive [133] and may be able to distinguish the site specific contributions.

Figure 5.19 shows the energy dependence of the valence band photoemission spectra taken with photon energies close to the Cr $L_{3,2}$ and Fe L_3 edges. The spectra are normalised to the photon flux. The given photon energies correspond to the un-calibrated monochromator readings. Therefore, the onset and maxima of the white lines as found from the maximum of the energy derivatives of the absorption spectra are marked. The spectra excited close to the Cr $L_{3,2}$ edges show a 2 eV wide feature close to the Fermi energy (see Figure 5.19(a)). No particular enhancement of the intensity is observed if the photon energy is crossing the Cr L_3 white line of the absorption spectrum. The L_3VV Auger electron emission is observed just when the onset of the Cr L_3 absorption edge is reached. It can be clearly identified from its linear energy dependence assigned by a straight line in Figure 5.19(a). On a kinetic energy scale it stays fixed. The off-resonant spectra (560 eV, 605 eV) are very similar in the valence band region (-10 eV...0 eV). No particular features are detectable if crossing the L_2 edge.

Figure 5.19(b) shows the valence band spectra taken with photon energies close to the Fe L_3 absorption edge. The intensities at the Fermi energy are enhanced by a factor of ≈ 1.6 in the photon energy range of 706 eV to 707 eV compared to excitation before the edge at 702 eV. As for Cr, the evaluation of the L_3VV Auger electron emission is clearly visible.

The spectra observed here at the Cr and Fe L_3 resonance are obviously different from those reported by Hüfner *et al.* [134] for elemental metals, even if accounting for the higher analyser resolution used in that work. (The present overall resolution was about 100 meV.) In particular, the L_3VV Auger emission is less pronounced. An Auger signal with varying kinetic energy was not detectable. The differences in the resonant behaviour as well as the Auger emission are clearly related to the differences between the materials that is an alloy here compared to pure metals in [134].

Figure 5.20 shows the photon energy dependence of the valence band photoemission spectra taken with photon energies close to the Co L_3 edge. The spectra exhibited a strong variation of the intensity with the photon energy. Therefore, they were normalised to their maxima for better comparison. Above the onset of the L_3 white line, the intensity at ϵ_F is enhanced by a factor $5...3.5$ with increasing photon energy. Again, the constant-kinetic-energy L_3VV Auger electron emission is clearly observed if the onset of the L_3 absorption edge is reached. Moreover, at energies before the edge an additional dispersionless feature (note the larger energy steps for lower photon energies) becomes visible at 4.5 eV binding energy. Its maximum at 776.6 eV excitation energy is about $35\times$ more intense than the intensity at 774 eV photon energy. Part of this very high intensity is, however, due to the intense underlying L_3VV Auger electron emission. This type of feature was previously assigned as two-hole satellite [134] with varying two-hole correlation energy.
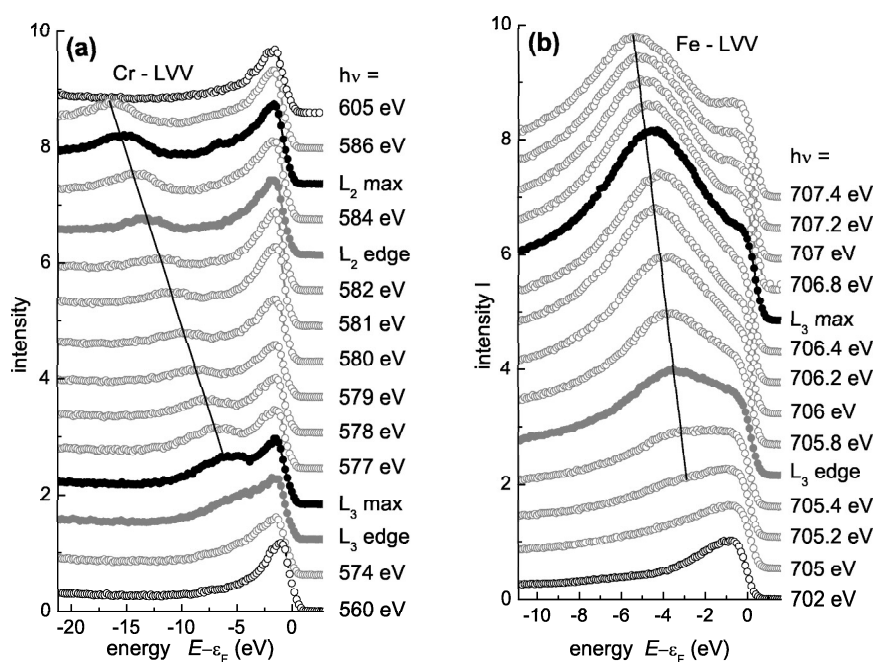
Figure 5.19: Valence band-XPS of $Co_2Cr_{0.6}Fe_{0.4}Al$.
Photoemission spectra excited by photon energies close to the Cr $L_{3,2}$ (a) and close to the Fe L_3 (b) absorption edges. The lines along the L_3VV Auger transitions are drawn to guide the eye. Photon energies are un-calibrated monochromator readings and the onset and maxima of the white lines are marked.
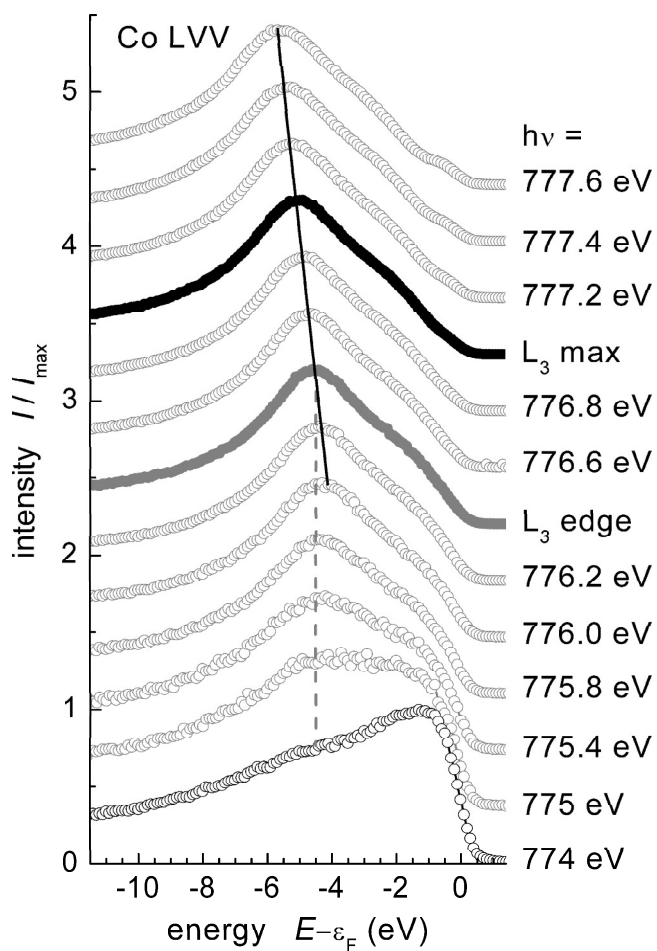
Figure 5.20: Resonant Co-valence band-XPS of $Co_2Cr_{0.6}Fe_{0.4}Al$.
Resonant photoemission spectra excited by photon energies close to the Co L_3 absorption edge. The energies corresponding to the onset and the maximum of the white line are marked. The spectra are normalised to the maximum intensity (see text). The full line along the L_3VV Auger transition is drawn to guide the eye. The dashed line assigns a dispersionless feature.
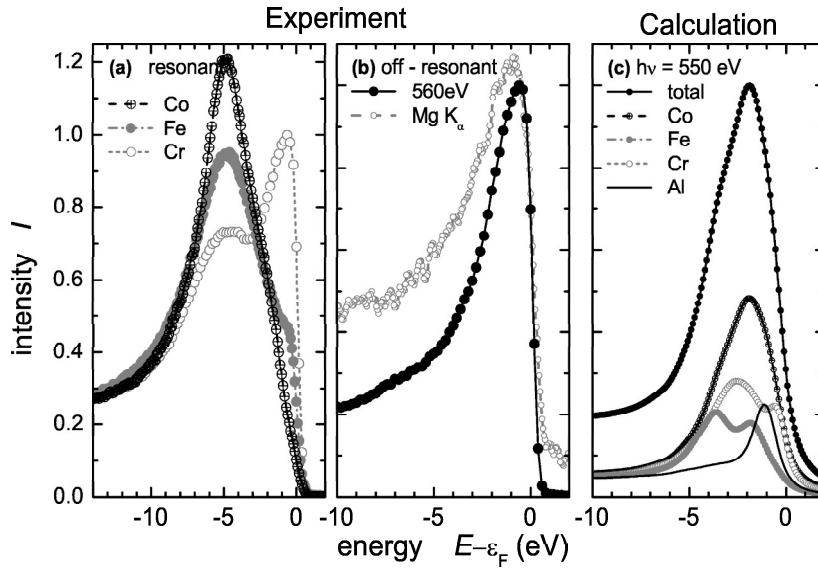
Figure 5.21: Soft X-ray excited XPS of $Co_2Cr_{0.6}Fe_{0.4}Al$.
Shown are the resonant (a) and the off-resonant (b) photoemission spectra in comparison
to calculated site-specific spectra (c) [123]. (Note the slightly different energy scale in
(a), for normalisation of the spectra see text.)

Other than at the Cr and Fe edges, a clear resonance like behaviour is observed in
the valence band spectra when crossing the Co L_3 absorption edge, especially at the
Fermi energy. This may be due to the particularly higher order of the Co atoms in
the compound. Already when neglecting any $B2$ type disorder, Fe and Cr are randomly
distributed on the regular sites of the $L2_1$ structure of the Heusler compounds leading to
an alloy like behaviour. The small enhancement of intensity at the Fe edge presumably
reflects a higher order of those atoms compared to Cr.

Figure 5.21 compares measured and calculated photoemission spectra for polycrys-
talline
$Co_2Cr_{0.6}Fe_{0.4}Al$. Shown are the resonantly excited spectra (a), the off-resonant spectra
(b) and the calculated spectra (c). The on-resonance spectra are taken at the maxima
of the L_3 absorption edges of Co, Cr, and Fe. They were normalised to the intensity at
15 eV binding energy for better comparison. The off-resonance spectrum was taken at
560 eV, that is well below the onset of the Cr L_3 edge. The spectrum excited by Mg
K_α radiation is shown for comparison in Figure 5.21(b). The calculated spectrum in
Figure 5.21(c) shows the total intensity for 550 eV photon energy together with the site
resolved spectra for Co, Cr, Fe, and Al. These spectra were calculated using a 0.1 Ry
Cauchy-Lorentz broadening without accounting for energy dependent hole lifetimes.

The resonantly excited spectra at the absorption edges of the elements in
$Co_2Cr_{0.6}Fe_{0.4}Al$ are governed by the L_3VV Auger lines and thus do not allow an element

specific discrimination of the density of states, unfortunately. This is not a matter of resolution but explained by the high intrinsic width of the Auger lines. It is clearly seen that the ratio between the Auger line and the intensity at the Fermi energy depends strongly on the element. It is highest for Co (> 10) but only very small for Cr (< 1). Fe lies in between and the intense emission close to the Fermi energy is still visible. The off-resonance spectrum exhibits a sharp onset at the Fermi energy with a maximum of intensity at 0.7 eV binding energy. The low lying s-bands contribute only weakly to the intensity at binding energies between 5 eV and 10 eV. The calculated spectrum exhibits a high intense peak at 1.9 eV binding energy that can clearly be attributed to emission from states located at the Co sites. In comparison, a light enhancement of the intensities at energies between 3.5 eV and 7 eV below ϵ_F is observed in the spectrum excited by Mg K_α radiation.

The discrepancy between the intensity maxima observed in the experiment compared to the calculated one may be explained as follows. The calculated spectrum is a true bulk spectrum with the surface neglected completely whereas the experimental spectrum at 550 eV photon energy is still dominated by surface effects as the electron mean free path is in the order of 10 Å and thus less than the height of two cubic $L2_1$ cells. From the calculated spectrum one expects high emission from Cr and Al sites at 0.6 eV and 1.0 eV binding energy, respectively. Thus the comparison between experiment and calculation indicates that Cr and Al may have segregated to the surface to some extent, or equivalently, it points on a loss of Co and Fe in the region close to the surface. In addition, the measured high intensity close to the Fermi energy is partially due to the high lifetime of holes at ϵ_F that is not directly accounted in the calculation.

High energy photoemission was performed using monochromised X-rays of about 3.5 keV energy. The energy scale was calibrated at the Fermi energy of the Au valence band and $4f$ spectra (not shown here). The overall resolution (optics plus analyser) was determined from the Au valence band spectrum to be better than 55 meV at 3.5 keV under the same conditions used for the spectra discussed in the following.

Figure 5.22 shows the valence band spectrum of $Co_2Cr_{0.6}Fe_{0.4}Al$ excited by hard X-rays. A broad feature of about 2 eV width appears close to the Fermi energy. In addition, another broad feature becomes visible between 4 eV and 7 eV below the Fermi energy that is also revealed in the low resolution spectrum (see inset in Figure 5.22). Subtracting a Shirley type background (compare Figure 5.23(b)) reveals an overall width of the valence band of about 10 eV. Other than in the low energy spectra, there is no pronounced overshooting of the intensity close to the Fermi energy. This results in better agreement with the DOS showing its maximum at 1.5 eV below ϵ_F. The low energy spectra are governed by the high lifetime of the holes close to the Fermi energy. At high energy excitation (3.5 keV) the electrons are faster by a factor of about 2.2 (compared to 700 eV) thus the interaction of the outgoing electron with the remaining $N-1$ electron state of the solid becomes weaker. This observation gives clear evidence that one has to work at much higher energies in order to come close to the limit of sudden approximation.

Figure 5.23 compares the measured photoemission spectra for polycrystalline $Co_2Cr_{0.6}Fe_{0.4}Al$ with the calculated total DOS. For better comparison, a Shirley type
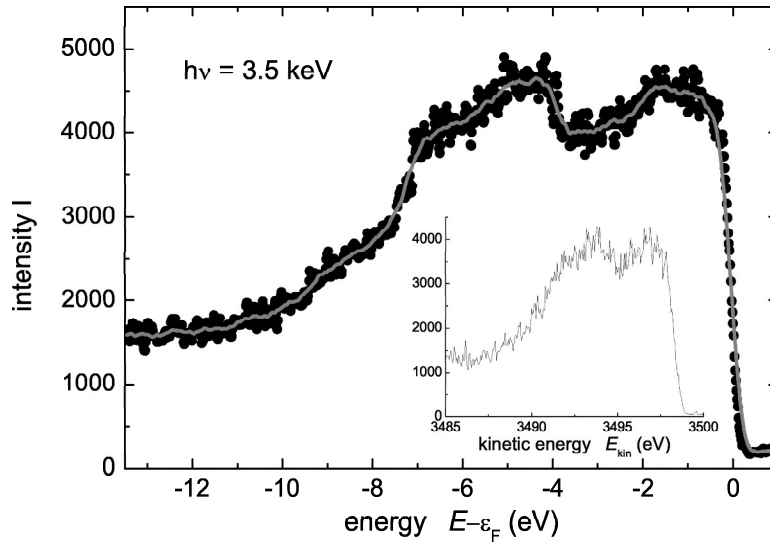
Figure 5.22: High resolution - high energy VB-XPS of $Co_2Cr_{0.6}Fe_{0.4}Al$.
The photoemission spectra are excited by hard X-rays of 3.5 keV energy. The inset shows a spectrum taken with lower resolution plotted versus kinetic energy.

background was subtracted from all photo emission spectra and the spectra were normalised to their maxima. The low energy spectra (a) are shifted additionally in intensity by an offset of 0.15 with respect to each other. For better comparison, the high energy spectra (b) taken with a lower but equal resolution are shown and also shifted with respect to each other. The total density of states (c) was convoluted by a Fermi distribution for 300 K after averaging over both spin components. The $L2_1$ curve is shifted by 2 eV for better comparison.

The DOS for the $L2_1$ structure can be distinguished in two regions: first, the low lying sp-band between 6 eV and 10 eV binding energy and second, the d-bands ranging from about 5.5 eV up to the Fermi energy. The DOS for the $B2$ structure is similar, but the low lying gap between sp and d bands is not longer revealed. The off-resonant, low energy, spectra are governed in the excitation energy range from 560 eV to 1.2 keV by a high intensity close to the Fermi energy. The low lying sp-band or the Heusler gap between sp and d-bands are hardly detectable in those spectra. The measured high resolution - high energy spectrum exhibits a width of the d-bands of about 7 eV with a clear minimum at about 3 eV binding energy as well as the low lying sp-band extended up to 10 eV binding energy. The differences in the d-band emission and the total DOS are obvious. The maximum of the DOS at about 1.5 eV below ϵ_F is less pronounced in the HE-spectra and absent at low excitation energies. Suppose that electron correlation can not be neglected even though the d-states are de-localised without doubt. In that case
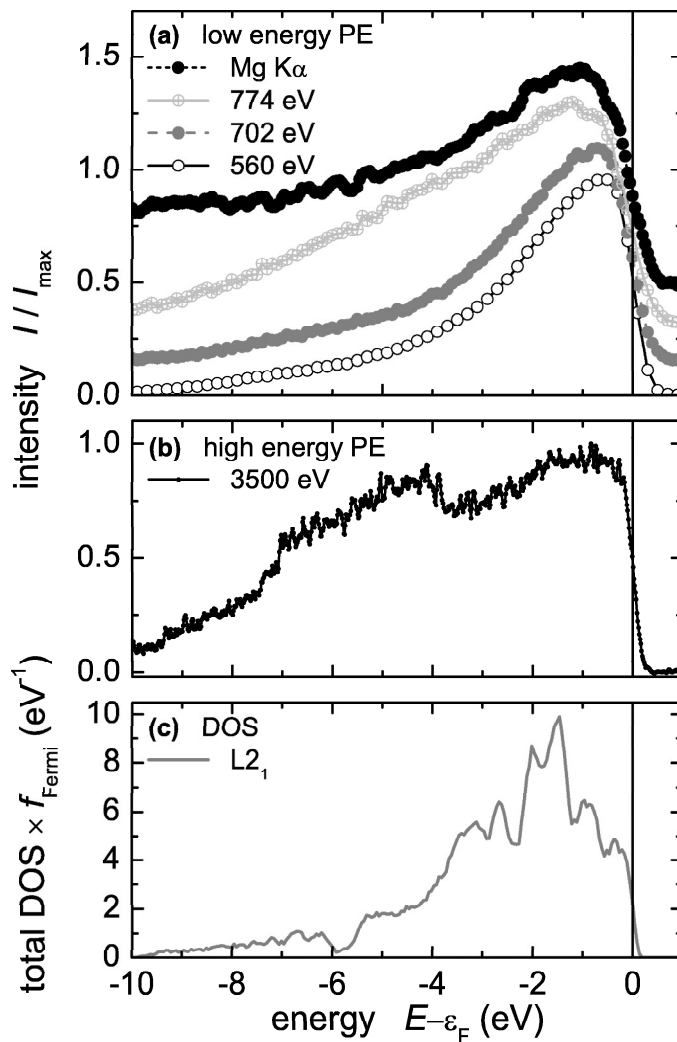
Figure 5.23: PE spectra and DOS.
    Compared are the valence band spectra of $Co_2Cr_{0.6}Fe_{0.4}Al$ excited by low (a) and high
    (b) photon energies to the calculated, spin averaged, total density of states (c). (For
    applied data manipulation see text.)

one will expect a splitting of the d-bands increasing its width that is not reproduced by pure LSDA calculations. It is worthwhile to note that the off-resonant spectra exhibit an enhancement at energies of approximately 4 eV to 7 eV below ϵ_F for excitation energies above 750 eV. Both high energy spectra, taken at 3.5 keV and 8 keV, reveal a high intensity at about $(-4 \ldots -7)$ eV binding energy where the LSDA calculations predict the gap between the low lying sp band and the d bands. Moreover, the high intensity feature at about 4.5 eV binding energy is not only observed in the high energy spectra. It corresponds roughly to the dispersionless feature revealed by the resonantly enhanced low energy spectra (seen at the Co L_3 edge). There is, however, no according high density observed in the DOS, neither in total nor partially for Co. From this point of view, the high energy spectra give evidence that electron-electron or electron-hole correlation may play an important role in Heusler compounds, at least for those being Co_2 based like the one investigated here. The new feature seen by bulk sensitive photo emission corresponds to a band-complex between 2.2 eV and 5.5 eV below ϵ_F. It cannot be explained by disorder but may point on some deficiencies of the local spin density approximation.

Overall, the photo emission experiments show that the material has a high density of states close to the ϵ_F. This has to be seen as an advantage of $Co_2Cr_{0.6}Fe_{0.4}Al$ compared to other predicted half-metallic ferromagnets like the high moment compounds NiMnSb or Co_2MnSi. In the latter compounds with above $1\mu_B$ per atom, the density of majority states at ϵ_F is arising from few strongly dispersing d bands crossing the Fermi energy. This results in a low majority density of states at ϵ_F. Any even small perturbation of the minority gap in such systems will lead to a strong decrease of the spin polarisation and thus causes a strong reduction of effects in spin dependent transport properties. The large majority density at ϵ_F explains also why the spin polarisation stays rather high in partially $B2$ disordered $Co_2Cr_{1-x}Fe_xAl$ in agreement to Miura et al. [23, 24].

In conclusion, it was shown that full relativistic SPRKKR calculations are very useful to explain spectroscopic experiments. The KKR method with CPA was successfully used to explain experimental spectra including random disorder in the investigated samples. The use of a full relativistic scheme allows the correct determination of transition matrix elements needed to calculate spectroscopic quantities, in particular if the photon or electron spin plays a role.

5.4 Summary for $Co_2Cr_{1-x}Fe_xAl$.

In summary, the structural and chemical properties of the compound $Co_2Cr_{1-x}Fe_xAl$ were investigated. XRD as well as EXFAS and ^{57}Fe Mößbauer spectroscopy indicate different structures in bulk and surface for the Heusler compounds $Co_2Cr_{1-x}Fe_xAl$. The bulk is $B2$ ordered, while the surface shows preferred orientation in combination with oxidation. This oxidation seems to be selective on Cr and Al. Thus thin film devices to built magnetic tunnel junctions have to be prepared in Ultra high vacuum to ensure the designated structure and thus the predicted spin polarisation.

Results from various experiments (XMCD, soft and hard X-ray valence band pho-

toemission) for the quaternary Heusler alloys $Co_2Cr_{1-x}Fe_xAl$ wwere analysed in the light of ab-initio calculations. Special attention was focused on $Co_2Cr_{0.6}Fe_{0.4}Al$. The measured overall and site specific magnetic moments are in accordance with the calculations, if disorder is assumed. In particular, it was shown that Co-Cr disorder leads to the low magnetic moment observed in Co_2CrAl. It points on ferrimagnetic order with an anti-parallel alignment of part of the Cr moments in disordered alloys.

It was found by resonant and high energy photo emission that there is a discrepancy between the experimentally observed and the theoretically calculated density of states in $Co_2Cr_{0.6}Fe_{0.4}Al$. This observation suggests the presence of correlation in Heusler compounds being not accounted for by local spin density approximation in its current form. Moreover, strong differences in surface and bulk photo emission spectra (excited at photon energies from 500 eV to 8 keV) reveal the loss of the bulk signature if emission takes mainly place from the surface layer.

6 The Heusler Compound Co$_2$CrIn.

6.1 Introduction.

A comprehensive characterisation of Cr containing Heusler compounds is necessary in order to understand the mechanism of the reduced magnetic moment of Cr in the Co$_2$Cr$_{1-x}$Fe$_x$Al compounds in contrast to the Co$_2$Cr$_{1-x}$Fe$_x$Ga compounds. Co$_2$YZ Heusler compounds with Z = Al, Ga are already known, the next compound with an element of the series of main group elements is a Co$_2$YZ Heusler compound with Z = In. This compound has not been reported up to now. Therefore, Co$_2$CrIn was synthesised and characterised in this work.

6.2 Structural Properties.

Figure 6.1 shows the diffractogram of Co$_2$CrIn. There are 4 formular units per unit cell leading to an overall composition of $Co_8Cr_4In_4$. The background was refined using 9 terms of a Legendre Polynom and the 2θ-range of 15° - 22° was excluded from the refinement. Within the fitting procedure, the peak form was assumed to have a Lorentz-shape with L$_x$ = 8.2(5) and L$_y$ = 21.5(13). The lattice constant is determined with this refinement parameter to be 6.0596(2) Å. The positional and atomic displacement factors U$_{iso}$ are small with U$_{iso}$ (Co) = 0.019(2), U$_{iso}$ (Cr) = 0.027(2) and U$_{iso}$ (In) = 0.007(2). The cell volume is 222.506(8) Å^3 and the calculated density amounts to 8.495(3) g/cm^3. The quality of the fit was denoted in the values of R = 3.59, R$_{wobs}$ = 1.5 and R_{wall} = 1.54. In addition, the diffractogramm of Co$_2$CrIn exhibits additional reflections due to a small amount of an unidentified phase.

The refinement of Co$_2$CrIn revealed no large disorder effects and in particular no $B2$ like disorder in contrast to Co$_2$CrAl. A high degree of disorder arising from the Co and Cr positions (DO$_3$ disorder) could be excluded from the refinement. Any disorder influences the intensities of the (111) and (200) reflection. Thus the ratio of the intensities of the (111) and (200) reflection might be used as an indicator of disorder effects in this class of compounds. In Co$_2$CrIn, the cross sections of Co or Cr and In are of different orders of magnitude. Thus the ratio of the intensities of of the (111) and (200) reflections of Co$_2$CrIn is more significant in Co$_2$CrIn than in Co$_2$CrGa and Co$_2$CrAl and disorder effects are more apparent.

Figure 6.2 shows the the XAS spectrum taken at the $L_{3,2}$ absorption edges of Cr and Co. The sample was cleaned in UHV by scratching the surface of the sample with a diamond file. After removing the surface, the sample reveals no oxidation at the Co edge and in particular not at the Cr edge.
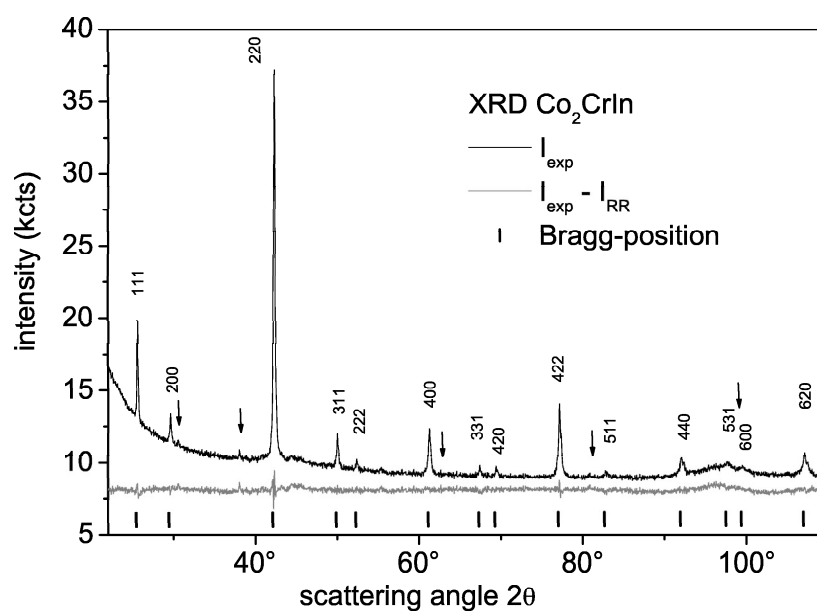
Figure 6.1: Diffraction pattern and difference plot of the Rietveld refinement of Co₂CrIn.
Shown are the measured intensity (I_{exp}) and the difference compared to the Rietveld
refinement (I_{RR}). Vertical bars indicate the Bragg positions of the expected diffraction
peaks. Reflections of a secondary phase, which could not be identified, are marked with
arrows.
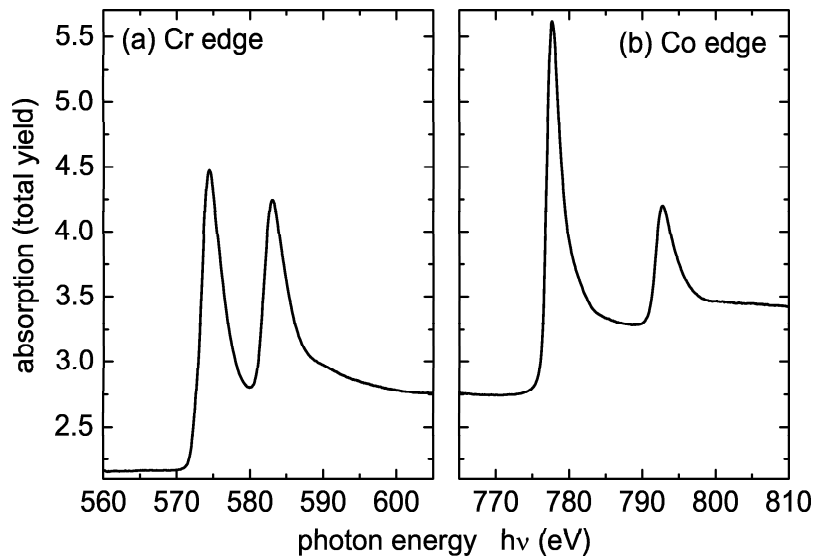
Figure 6.2: XAS spectrum of Co_2CrIn taken at the Cr and the Co edge.
The spectrum reveals no oxidation.

6.3 Magnetic Properties.

The magnetic properties were measured by means of SQUID magnetometry. Figure 6.3 shows the hysteresis curves of Co_2CrIn measured at 5 K and 300 K. The magnetic moment in saturation is 1.18 μ_B at 5 K and 1.1 μ_B at 300 K. Co_2CrIn turns out to be soft magnetic with a small remanence and a small coercive field.

Many Co_2YZ Heusler compounds follow the Slater-Pauling curve [35, 36], as described by Kübler [37]. An application of this *valence electron rule* on Co_2CrIn leads to a magnetic moment of 3 μ_B. This is the expected magnetic moment for all Co_2CrZ compound with Z being a third main group element, if the compound is predicted to be a half-metallic ferromagnet. Thus, the measurement reveals a reduced magnetic moment and no half-metallic ferromagnet. The structural refinement showed no large amount of disorder. Thus the reduced magnetic moment is not due to disorder effects and may arise from an antiferromagnetic coupling of some atoms.

6.4 Summary for Co_2CrIn.

In summary, this work presents the synthesis and characterisation of the Heusler compound Co_2CrIn. The compound is $L2_1$ ordered and shows no antisite disorder effects. Co_2CrIn turns out to be a ferrimagnet with a magnetic moment of 1.18 μ_B at 5 K. In addition, the hysterisis curve reveals a soft magnetic behaviour. A measurement of the
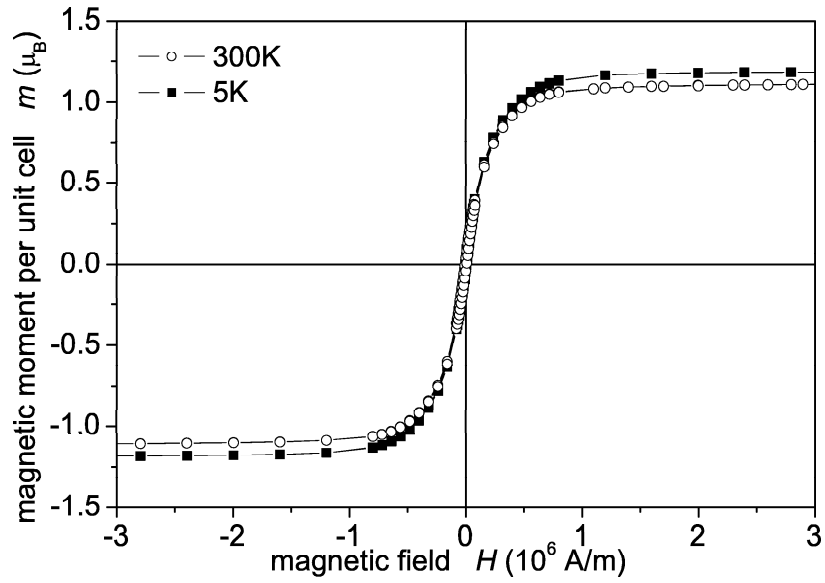
Figure 6.3: Magnetic hysteresis curve of Co_2CrIn at 5 K and 300 K, respectively.

site specific magnetic moments is highly desirable as it might lead to a deeper under-
standing of the magnetic properties of Co_2CrIn. Furthermore, the measured magnetic
moment is not an integer number, as expected for a half-metallic ferromagnet. Thus,
Co_2CrIn can not be a half-metallic ferromagnet, as most of the other Co_2YZ Heusler
compounds.

7 Half-Metallic Completely Compensated-Ferrimagnets.

7.1 Introduction.

In 1991, de Groot [53] predicted the Heusler compound MnCrSb to exhibit ferrimagnetic coupling with compensating magnetic moments and 100 % spin polarisation at ϵ_F. This class of material was, unfortunately, called half-metallic antiferromagnets. Two cases of this rather unusual antiferromagnetism may occur in cubic systems under investigation in Ref. [53] and here. In $C1_b$ compounds, the moments of two different atoms with the same site symmetry in the paramagnetic state (T_d) compensate, like the moments of Mn and Cr in MnCrSb. In DO_3 compounds, the moments of the same type of atoms with different site symmetry in the paramagnetic state $(T_d$ and $O_h)$ compensate, like in Mn_3Ga as reported below. Accordingly, in $L2_1$ compounds the kind of atom and local site symmetry are both different. However, all those materials do principally not fulfil the symmetry requirements needed to be an antiferromagnet. In usual antiferromagnets, the compensating magnetic moments originate from the same kind of atom. A distinct symmetry element (combined with time inversion operation) relates the magnetic moments on the different sites with oppositely oriented moments. Such a symmetry is absent for the materials discussed in this work. In the materials under investigation, the magnetic moments on crystallographically different lattice sites compensate at a particular band filling (Note the absence of a symmetry element linking these sets of atomic positions to one another - even in the paramagnetic state). This is the configuration encountered for ferrimagnetic materials at the compensation point and is entirely different from an antiferromagnet. The only common property between this type of ferrimagnets and the regular antiferromagnets is the vanishing overall magnetic moment in the ground state and some related physical properties.

In regular compensated ferrimagnets, the compensation is not a ground state property but a thermally excited state. Therefore, the class of ferrimagnetic materials with complete spin polarisation at ϵ_F and a ground state with compensated magnetic moments will be called in the following: half-metallic completely compensated-ferrimagnets (HMCCF).

Unfortunately, the as HMCCF suggested material MnCrSb does not crystallise in the required C_{1b} structure [135]. As presented by van Leuken and de Groot [54], another possible material is $Fe_8MnV_7Sb_7In$, a Heusler type quintinary compound. Quintinary compounds are difficult to synthesise in their stoichiometric form. This means that MnCrSb as well as $Fe_8MnV_7Sb_7In$ are mainly interesting from a theoretical point of view [136]. Other half-metallic materials with compensated moments have been expected in the class of double perovskites [136, 137, 138] as well as the class of thiospinels [139]. However, experiments have shown that, due to disorder, the predicted material $LaAVMoO_6$ (A = Ca, Sr, Ba) is a normal metallic ferrimagnet [140].

7.2 Presentation of the Rule for Prediciton of HMCCF Materials.

Many of the Heusler compounds fulfil the Slater-Pauling rule [35, 36], which states that the magnetic moment is determined by the mean number of valence electrons per atom [35, 36, 2, 98]. This rule can be specified for ordered compounds [2, 98] such, that the magnetic moment (m, in μ_B) can be calculated by subtracting 18 for the $C1_b$ or 24 for the Heusler compounds from the accumulated number of valence electrons (N_V) in the unit cell. It follows immediately that $C1_b$ compounds with 18 valence electrons and Heusler compounds with 24 valence electrons are not ferromagnetic. The prototypes for non-ferromagnetic compounds are CoTiSb [141] ($N_V = 18$) and Fe$_2$VAl [142] ($N_V = 24$). Both compounds are semiconductors [141, 142]. Another prototype for a non-ferromagnetic Heusler compound with 24 valence electrons may be considered. Mn$_2$VAl is a half-metallic ferromagnet with 22 valence electrons [143]. In this compound, Mn occupies the X position. Substituting half of the Mn by Co (on the X position!) also results in a non-ferromagnetic compound ((Mn$_{0.5}$Co$_{0.5}$)$_2$VAl) with 24 electrons [144]. This implies that mixed Heusler compounds with 24 valence electrons also follow the Slater-Pauling rule.

Besides the Slater-Pauling rule, another rule, as described by Kübler et al. [2], states that the properties of Mn on the Y position in the Heusler compounds must be included. This rule states that Mn on the Y position in Heusler compounds tends to have a high, localised magnetic moment [2, 27, 143]. According to electronic structure calculations, in the $C1_b$ compounds, Mn on the Y position has a magnetic moment of approximately 4 μ_B. Mn may be formally described as Mn^{3+}, with a d^4 configuration. In accordance with the itinerant character of the 3d transition metals, one will find a lower magnetic moment, even if there is a partial localisation of the d electrons.

As an example, the Slater-Pauling rule can be applied to NiMnSb [3], which has 22 valence electrons and a total magnetic moment of 4.0 μ_B. Suga et al. [145] reported a local magnetic moment of 3.62 μ_B at the Mn site, while Ni and Sb have small magnetic moments. Large magnetic moments of Mn on the Y position in the Heusler compounds X_2YZ have also been found [2, 27, 143]. A detailed list of magnetic moments located at the Mn Y site in Heusler compounds is given in reference [2]. As already mentioned above, the Heusler compound (Mn$_{0.5}$Co$_{0.5}$)$_2$VAl, with 24 valence electrons and Mn on the X position, is not ferromagnetic, indicating the importance of the role of the atom on the Y position for half-metallic completely compensated-ferrimagnetic character.

A combination of the Slater-Pauling rule [35, 36] and the Kübler rule [2] given above will be introduced in this work, leading to a rule for the prediction of half-metallic completely compensated-ferrimagnetism in Heusler compounds with 24 valence electrons and with Mn on the Y position. In this compounds, the two atoms on the X site have to compensate the magnetic moment of the Mn at the Y site. This rule is in agreement with the approach of de Groot in reference [53]. In [53], the above mentioned rule was implicitly applied in the case of MnCrSb, resulting in the prediction of the completely compensated magnetic moments in MnCrSb. For convenience, the Mn on the Y position

(4b) with the cubic environment will be referred to as MnI and the atom on the X position (8c) with tetrahedral environment will be indicated by the numeral II.

Potential half-metallic completely compensated-ferrimagnets were considered. Mn has to be the more electropositive transition metal in order to occupy the Y position. Possible transition metals to occupy the X position are the more electronegative elements Fe, Co, Ni, Cu, and Zn as well as Mn itself. All those transition metals have seven (Mn) or more valence electrons. The accumulated number of electrons is limited to 24 to result in a zero net moment. This condition allows only few possible models, namely the binary Mn_2MnZ compounds, with Z being a IIIa element. Thus, the binary (Heusler [1]) compounds Mn_3Z are the simplest possible models (Z = Al or Tl are not yet reported, Z = In [146, 147], and Z = Ga [148, 47, 149]). They may be the most practical candidates for checking the HMCCF state because they consist of only two different kinds of atoms.

7.3 Application of the Rule for Prediciton of HMCCF Materials.

To check the validity of the rule for predition of HMCCF materials found semi-empirically, self-consistent field calculations were performed using the full potential linear augmented plane wave (FLAPW) method as provided by WIEN2K [69]. For comparison, the linear muffin tin orbital (LMTO) method [97] and the Korringha-Kohn-Rostocker (KKR) method [67] were used. In most cases, it was found that the results did not depend upon a particular method for the electronic structure calculations, however, the methods with spherical potentials seem to underestimate the gap in the minority states. In some cases only a pseudo gap was found when using spherical potentials.

Mn_3Ga is the only one of the four binary compounds given above that is reported to order in the same space group ($Fm\overline{3}m$) like Heusler compounds [148, 47, 149]. First of all, a structural optimisation was performed for Mn_3Ga by minimising the total energy as a function of the volume. The optimised lattice parameter is $a = 5.8232$ Å (see Figure 7.1). For this lattice parameter, the calculation reveals a nearly complete compensation of the magnetic moments and a HMCCF character. A change of the lattice parameter up to ± 3 % only changes the local magnetic moments on the two different Mn sites. As shown in the lower panel of Figure 7.1, an overall increase of the lattice parameter slightly increases the magnetic moment of the MnII position and decreases the magnetic moment on the MnI position. The total magnetic moment of zero, as a sum of the site specific Mn moments, remains unaffected. This result is expected because the magnetic moment is very stable in the range of the gap and similar behaviour is observed during the lattice parameter optimisation of the Heusler compound Co_2FeSi [58, 59, 150].

The optimised lattice parameter was used to calculate the details of the electronic structure of Mn_3Ga (Figure 7.2). The obtained minority DOS clearly shows a gap at the Fermi energy (ϵ_F), while the majority DOS exhibits states at ϵ_F [2]. As shown by

---

[1] The ternary X_3Z compounds resulting from $Y = X$ are known as DO_3 compounds. They are usually not included in the class of Heusler compounds.

[2] In Mn_3Ga, there are 12 electrons in both spin channels so it is not possible to define the majority and
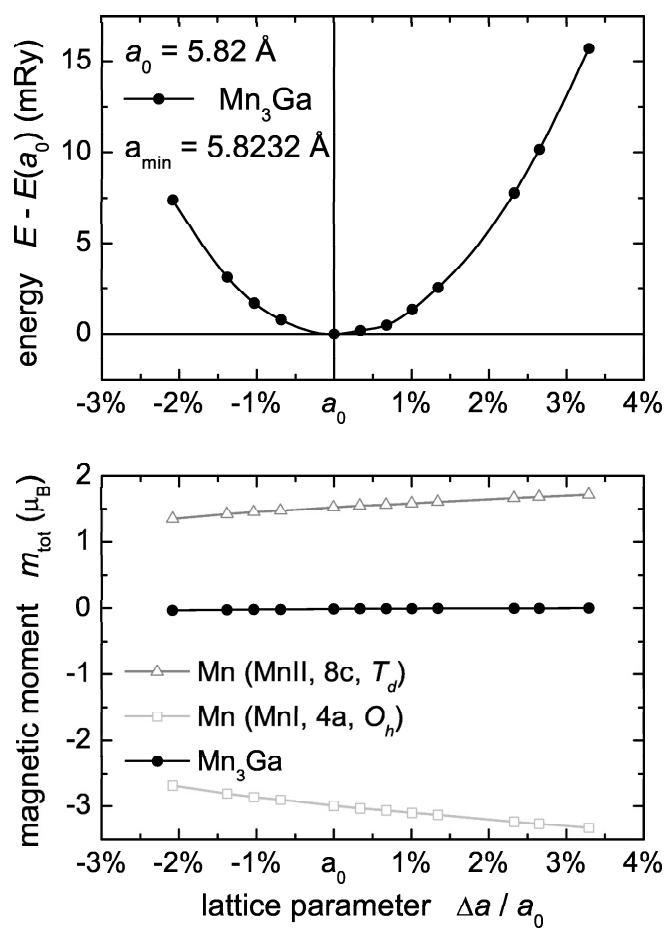
Figure 7.1: Structural optimisation for Mn₃Ga.
The optimised lattice constant (upper panel) and the magnetic moment (lower panel) are shown as functions of the lattice parameter.
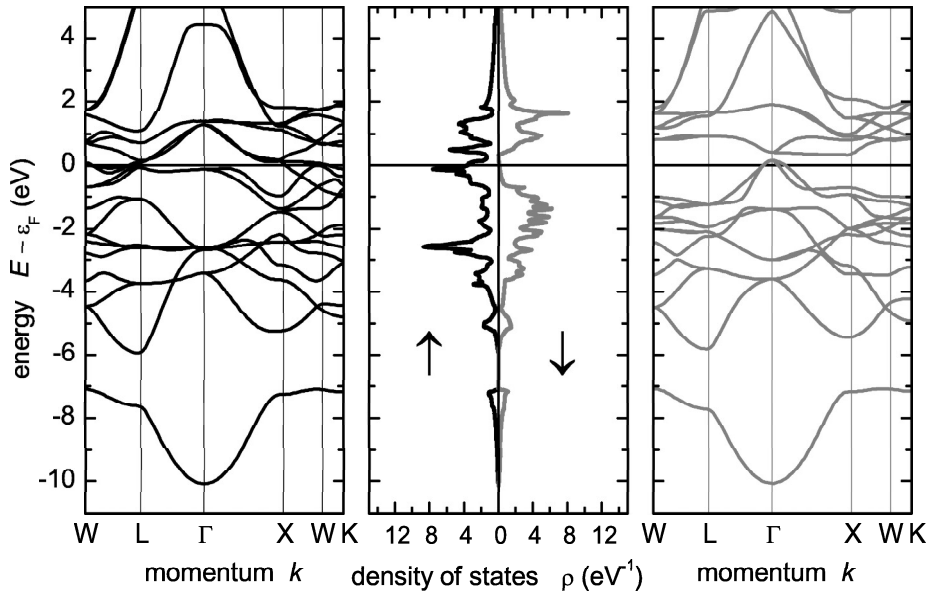
Figure 7.2: Band structure (right and left panel) and DOS (middle panel) of Mn_3Ga.
The band structure, as well as the DOS, clearly exhibits 100 % spin polarisation at ϵ_F.

Pickett in [55], the DOS follows the idealised DOS for a half-metallic state. The majority DOS shows a very narrow peak at -2.6 eV. These highly localised electrons also show up in the majority channel of the band structure as very flat bands through all high symmetry points in the Brillouin zone. In addition, the band structure indicates that the gap in the minority channel is a real gap and not a pseudogap.

Figure 7.3 shows the integrated DOS (number of states, NOS) of Mn_3Ga. Both spin channels contain 12 electrons. Up to -4.5 eV, the NOS is symmetric for both spin channels. This is the range of the low lying sp bands. At higher energies, the DOS for both spin channels starts to differ. The most interesting difference occurs near ϵ_F. As a result of the gap, the minority channel exhibits a plateau at approximately 0.75 eV around ϵ_F. In the range of this plateau, the number of electrons is constant.

The calculated magnetic moments of Mn_3Ga are $m_I = 3.03\ \mu_B$ for the Mn on the Y position (MnI), and $m_{II} = -1.54\ \mu_B$ for each Mn on the X position (MnII). The remaining part is found at the Ga atoms and in the interstitial.

Figure 7.4 shows the partial DOS of Mn_3Ga. The Mn on the X position mainly dominates the minority channel below ϵ_F and the majority channel near and, in particular, above ϵ_F. For MnI, there are no states at ϵ_F in the majority channel. The main contributions of the MnI lie in the majority channel below ϵ_F and in the minority channel above ϵ_F. As expected, MnI contributes to the parts of the DOS that are exactly the

minority spin channels by the number of electrons.
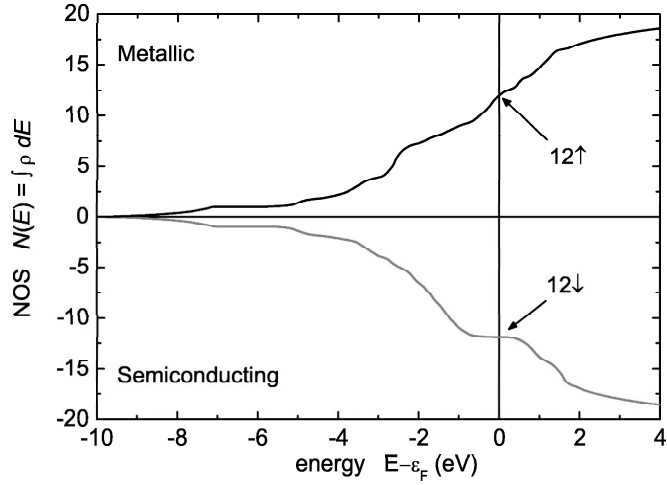
Figure 7.3: Integrated DOS of Mn_3Ga (NOS).The minority channel exhibits a plateau at ϵ_F.

opposite of the parts to which Mn atoms on the X position contribute. In particular, the DOS of MnII is rather widely spread, while the DOS of MnI has a narrow peak in the e_g orbitals at -2.6 eV. This narrow peak results in a localised magnetic moment. The MnI as well as the MnII show narrow peaks approximately 0.2 eV below ϵ_F in the t_{2g} states in the majority channel. These states form the MnI - MnII bond, which corresponds to the flat band in the $\Gamma - L$ direction at 0.2 eV below ϵ_F.

Figure 7.5 shows the distribution of the magnetic moment as function of energy. The black line represents the total distribution of the magnetic moment of Mn_3Ga. The light grey line shows the distribution of the magnetic moment of the MnI site and the dark grey line represents the distribution of the magnetic moment at the MnII site. Because of compensating magnetic moments, the magnetic moment is zero at the nodes of the magnetic moment distribution curve. Each of these orbitals carries a number that indicates the band that contributes to the partial DOS (see also Figure 7.4). The first contributing orbitals are the t_{2g} majority orbitals of the MnI t_{2g} at approximately -3.8 eV. The maximum of this peak is at -3.5 eV. At this energy, MnII starts to compensate this magnetic moment with the t_{2g} minority orbitals. These magnetic moments exactly compensate each other at -2.97 eV. The next magnetic contribution arises from the MnI e_g majority orbitals. The electrons in this orbital are highly localised and the magnetic moment in this orbital is approximately 2 μ_B. At -2.4 eV, the e_g minority orbitals of MnII start to contribute, cancelling the magnetic moment of the MnI e_g orbitals at -1.67 eV. The magnetic moment at MnII arises from t_{2g} minority electrons and is exactly compensated at ϵ_F by t_{2g} majority electrons located at MnI, leading to a magnetic moment of zero at ϵ_F. The magnetic moment at the MnI on the Y position sums up to about 3 μ_B, while each of the two MnII at the X position have a magnetic moment
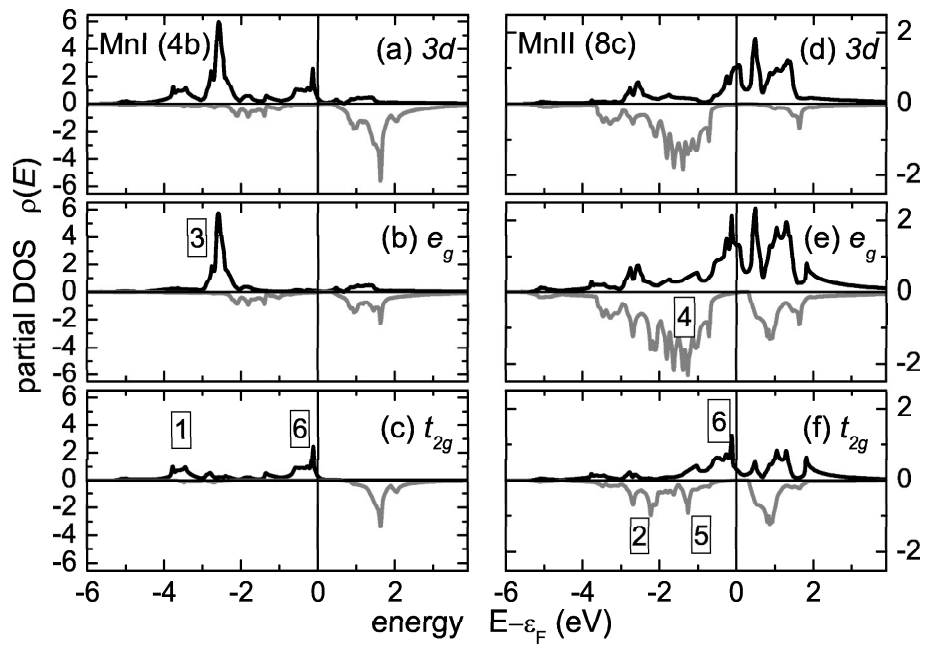
Figure 7.4: Partial DOS of Mn$_3$Ga.
The DOS of Mn on the X position (MnII) (panels a-c) and the DOS of Mn on the Y position (MnI) (panels b-f) are shown. Panels a and d show the Mn $3d$ DOS. The Mn d orbitals are split in e_g (panels b and e) and in t_{2g} (panels c and f). The low lying sp bands mainly belong to the Ga atoms (not shown here). The numbers indicate the corresponding states shown in Figure 7.5.
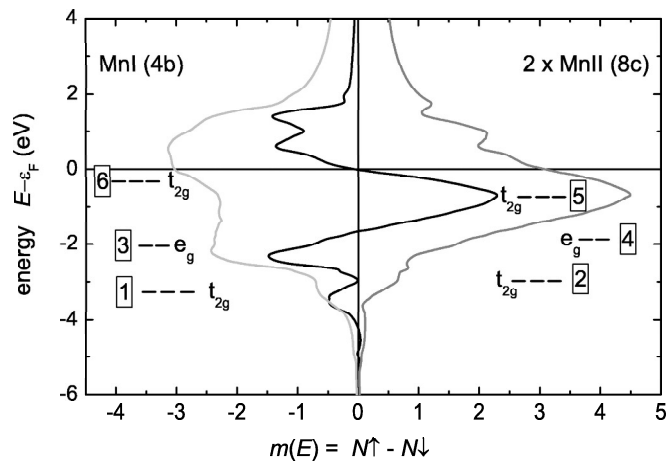
Figure 7.5: Magnetic moment as a function of energy, with indicated orbitals.
The light grey curve represents the magnetic contribution of MnI and the dark grey shows the MnII contribution. The black line corresponds to the magnetic distribution, which originates from the total DOS. The numbers indicate the corresponding states as given in Figure 7.4.

of -1.5 μ_B. As mentioned above, the highly localised electrons at -2.6 eV in the MnI e_g orbital comprehend a local magnetic moment of 2 μ_B. The remaining 1 μ_B of MnI is delocalised in the MnI t_{2g} orbitals, and the magnetic moment on the MnII site is considerably delocalised.

In the next section, the rule for the prediction of half-metallic completely compensated-ferrimagnetism is applied to ternary and quaternary compounds. These have the advantage of being constructed from already known existing Heusler compounds. In addition, the chances for an experimental realisation of a practicable HMCCF material are improved if the end members of the doped compounds exist like in the cases given below.

The $Mn_{3-x}V_xSi$ system was found to be a potential candidate for half-metallic ferrimagnetism with completely compensated magnetic moments. Mn_3Si has 25 valence electrons, which, according to the Slater-Pauling rule, results in an expected magnetic moment of about 1 μ_B. Mn_3Si is reported to be an antiferromagnet [151, 152, 153]. Mn_2VSi has 23 valence electrons and therefore it has also a predicted magnetic moment of 1 μ_B, but with a gap in the majority DOS. For further details regarding the calculated local moments, see Table 7.1.

A mixture of 50 % Mn_3Si (25 valence electrons) and 50 % Mn_2VSi (23 valence electrons) results in $Mn_2(Mn_{0.5}V_{0.5})Si$. The X site is completely occupied by MnII, while MnI and V share the Y site. The accumulated number of valence electrons is 24. This compound is also used as a test case whether a partial occupation of the Y position by Mn already leads to a localised magnetic moment and to a HMCCF state.

A supercell with an overall stoichiometry given by Mn_4MnVSi_2 in a tetragonal primitive cell was used to model the structure of $Mn_2(Mn_{0.5}V_{0.5})Si$. The spacegroup is

Compound	N_V	m_{tot}	m_X	m_Y
Mn_3Al	24	0.00	-1.42	2.84
Mn_3Ga	24	-0.01	-1.54	3.03
Mn_2VSi	23	0.97	-0.70	0.39
Mn_3Si	25	1.00	-0.88	2.69
$Mn_2(Mn_{0.5}V_{0.5})Si$	24	0.00	MnII: -0.88	MnI: 2.84; V: 0.52
Mn_2VAl	22	2.00	-1.52	0.95
Fe_2MnAl	26	2.00	-0.31	2.62
$(MnFe)(Mn_{0.5}V_{0.5})Al$	24	0.00	MnII: -1.53; Fe:-0.18	MnI: 2.79 ; V: 0.56

Table 7.1: Magnetic moments in proposed HMCCF compounds.
Total spin magnetic moments m_{tot} are given per unit cell. m_X and m_Y are the element specific magnetic moments on X and Y sites, respectively. All magnetic moments are given in μ_B. Note that a small part of the magnetic moment may also be localised outside the muffin-tin spheres and thus cannot be attributed to one of the atoms.

$P/4mmm$ with a lattice parameter ratio of $c/a = \sqrt{2}$. The lattice parameters are $a = 4.115$ Å and $c = a_c = 5.82$ Å, where a_c is the lattice parameter of the initially cubic $L2_1$ cell. The Mn related to the X position occupies the $(\frac{1}{2}\ 0\ \frac{1}{4})$ position in the supercell, the Mn dedicated to the Y position is now on $(\frac{1}{2}\ \frac{1}{2}\ \frac{1}{2})$, and V is placed on $(0\ 0\ 0)$. In this supercell, the Si atoms occupy two different positions being located at $(\frac{1}{2}\ \frac{1}{2}\ 0)$ and $(0\ 0\ \frac{1}{2})$.

The result of the electronic structure calculation is a HMCCF (see also Tables 7.1 and 7.2). Figure 7.6 shows the band structure and the DOS of $Mn_2(MnV)_{0.5}Si$, which fits the DOS for a HMCCF, as shown in [55]. The local magnetic moments compensate each other so that the total magnetic moment of $Mn_2(Mn_{0.5}V_{0.5})Si$ vanishes. The constituent magnetic moments for the referred compounds are listed in Table 7.1. Apparently, a partial occupation of the Y position by Mn is sufficient to enforce a localised magnetic moment and therefore results in a HMCCF. The minority bands exhibit a clear gap in the vicinity of the Fermi energy. The density of states and band structure of the supercell are, however, too complicated to be analysed in detail as for the example of Mn_3Ga given above.

In the next step, the quaternary system $Mn_{2-x}Fe_xMn_{1-x}V_xAl$ was analysed to verify the new rule. Mn_2VAl is a half-metallic ferromagnet with 22 valence electrons [143]. Assisted by calculations, the rule gives a magnetic moment of 2 μ_B for Mn_2VAl. This result is in agreement with the result obtained by Weht and Pickett [143]. Measurements in [3] and [154] confirm this value. In agreement with the Slater-Pauling rule, Fe_2MnAl is also a half-metallic ferromagnet with 26 valence electrons and a calculated magnetic moment of 2 μ_B. A 1:1 mixture of both compounds again results in a compound with 24 valence electrons, an expected total magnetic moment of zero, and with anti-parallelly coupled local magnetic moments (see Tables 7.1 and 7.2).

The $(MnFe)(Mn_{0.5}V_{0.5})Al$ structure was modelled using a orthorombic supercell ($P\ mmm$) with $a = b = c/\sqrt{2}$ using $c = a_c = 5.829$ Å and an overall stoichiometry
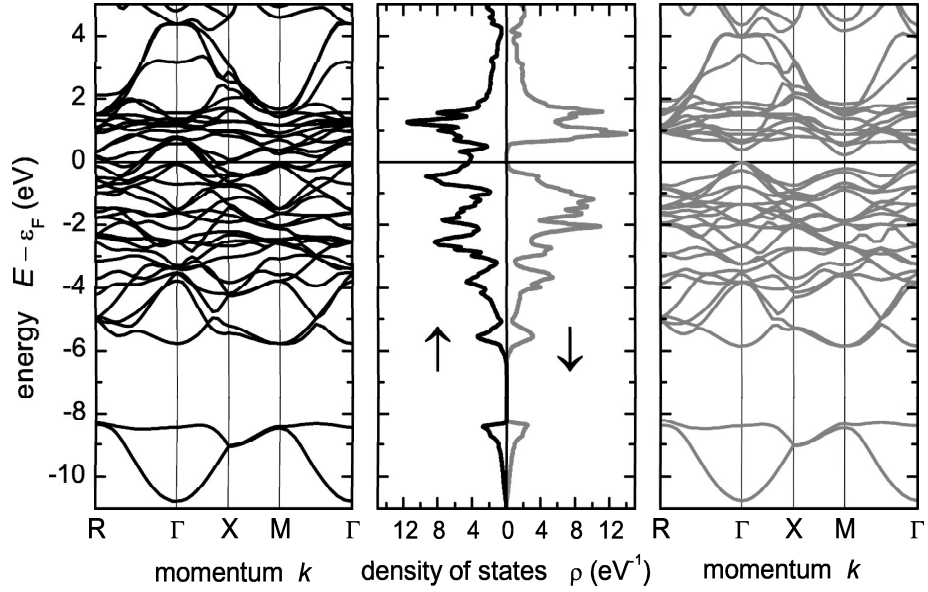
Figure 7.6: Spin resolved density of states and band structure of $Mn_2(Mn_{0.5}V_{0.5})Si$.
The calculations were performed for a tetragonal cell.

of $Mn_3Fe_2VAl_2$. As can be seen from the calculated electronic structure (shown in Figure 7.7),

$(MnFe)(Mn_{0.5}V_{0.5})Al$ is 100 % spin polarised at ϵ_F. The calculated magnetic moments (see Table 7.1) reveal an anti-parallel coupling of the moments on Y and X positions. Again, a partial occupation of Mn is sufficient to enforce a localised magnetic moment on the Y position leading to half-metallic completely compensated-ferrimagnetism.

Table 7.2 summarises the properties of the minority gaps of the investigated materials. Given are the extremal energies of the bands involving the gap and its resulting size. Mn_3Al shows a relatively large minority gap of 540 meV. The gap is reduced in the iso-valent compound Mn_3Ga to 180 meV and vanishes for Mn_3In. Such a reduction of the gap in compounds with the main group elements of the 5. or 6. period is observed very often in Heusler compounds.

In pure LSDA calculations at the optimised lattice parameter, the top of the Mn_3Ga minority valence band is slightly above ϵ_F (see also Figure 7.2). This is probably due to the van Hove singularity at ϵ_F in the majority states that may lead to numerical problems while integrating the total charge. An increase of the volume by 5 % reduces the size of the gap to $\Delta E = 30$ meV and it vanishes completely for larger lattice parameters. The lattice parameters of the Heusler compounds are usually determined by the main group element. This is finally the reason, why the gap vanishes in Mn_3In with a larger lattice parameter. The gap of Mn_3Al is considerably larger due to the smaller lattice parameter. It involves clearly the Fermi energy as is also observed for the mixed compounds.
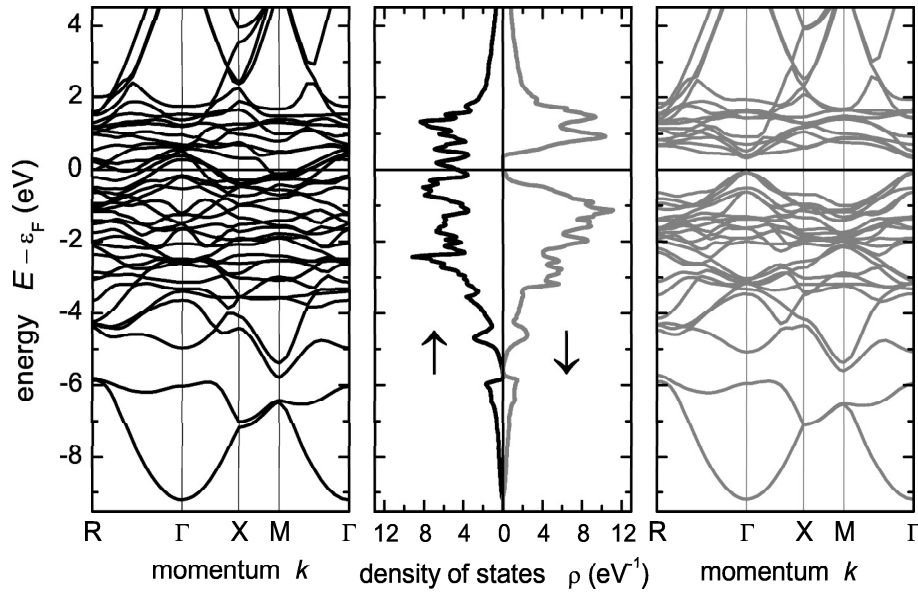
Figure 7.7: Electronic structure of $(MnFe)(Mn_{0.5}V_{0.5})Al$.
The calculations were performed for a orthorhombic cell.

Compound	a [Å]	E_{VBmax} [eV]	E_{CBmin} [eV]	ΔE [meV]
Mn_3Al	5.804	-0.12	0.42	540
Mn_3Ga	5.823	0.14	0.32	180
$Mn_2(Mn_{0.5}V_{0.5})Si$	5.82	-0.01	0.22	230
$(MnFe)(Mn_{0.5}V_{0.5})Al$	5.829	-0.06	0.32	380

Table 7.2: Minority band gaps.
E_{VBmax} and E_{CBmin} are the extremal energies of the lower and upper bands defining the position of the gap with respect to the Fermi energy. ΔE is the size of the gap in the minority states. a is the lattice parameter used for the calculations. For the mixed compounds, the corresponding lattice parameter a_c is given.

As already mentioned above, half-metallic materials with completely compensated moments are also found among double perovskites as well as thiospinels. Similar rules for predicting HMCCF compounds may also exist within these classes of materials. For the double perovskites, a sequence of numbers (12, 14, 16) appears that leads to a total magnetic moment of zero. In addition, these materials contain two strongly localised magnetic moments with fixed valences. This apparently results in different conditions for the occurrence of half-metallic compensated-ferrimagnetism in double perovskites. The number of valence electrons required to form a non-magnetic ground state is 10 for the thiospinels.

7.4 Summary.

In summary, a rule for predicting half-metallic completely compensated-ferrimagnetic behaviour is presented. This new rule is a combination of two well known rules. The first of these, which is the Slater-Pauling rule, determines the total magnetic moment from the mean number of valence electrons. According to this rule, the half-metallic system of interest must have 24 valence electrons. The Kübler rule, which is the second of these rules, states that Mn in Heusler compounds always carries a high local magnetic moment at the Y site. A combination of these rules results in an easy concept for finding new compounds with half-metallic type behaviour and completely compensated moments. Furthermore, it was found, that even a partial occupation of the Y position by Mn is sufficient to enforce a local magnetic moment on this site. The next step will be the synthesis and characterisation of the above mentioned compounds. The verification of their HMCCF type character by the performance of appropriate experiments will follow later.

8 Summary and Outlook.

This work encompasses a wide range of spin polarised Heusler compounds under various aspects.

In the fourth chapter, it was shown how simple rules may be used to estimate the properties of magnetic materials, in particular for those Heusler compounds exhibiting half-metallic ferromagnetism.

As practical application of these simple rules, it was found that the Heusler compound Co_2FeSi is a half-metallic ferromagnet exhibiting the highest Curie temperature and magnetic moment. In particular, a magnetic moment of $6\mu_B$ and a Curie temperature of 1100K were found in $L2_1$ ordered samples with a lattice parameter of 5.64Å.

The experimental findings are well supported by electronic structure calculations [57]. The comparison between experiment and calculations gives clear advice that electron-electron correlation plays an important role in Heusler compounds.

Regarding the high Curie temperatures in Heusler compounds, the present work leaves, however, some important questions open. There is still no convincing theory that explains why the dependence of T_C on the magnetic moment should be linear over such a wide range. For some alloys a linear dependence is indeed found, but never over such a wide range like for the Co_2YZ half-metallic Heusler compounds. An experimental challenge will be to find compounds with magnetic moments of above $6\mu_B$ to prove whether it is possible to find even higher Curie temperatures in this class of materials. Co_3Si, as an example, should exhibit $7\mu_B$, if following the *valence electron rule* as shown in chapter 5. Unfortunately, the compound crystallises in a hexagonal but not in the required Heusler structure.

The sixth chapter refers to the experimental results (XMCD, soft and hard X-ray valence band photoemission) for the quaternary Heusler alloys $Co_2Cr_{1-x}Fe_xAl$, analysed in the light of ab-initio calculations, with a focus on $Co_2Cr_{0.6}Fe_{0.4}Al$. The measured overall and site specific magnetic moments are in accordance with the calculations, if disorder is assumed. In particular, it was shown that Co-Cr disorder leads to the low magnetic moment observed in Co_2CrAl. It indicates ferrimagnetic order with an anti-parallel alignment of part of the Cr moments in disordered alloys.

It was found by resonant and high energy photoemission that there is a discrepancy between the experimentally observed and the theoretically calculated density of states in $Co_2Cr_{0.6}Fe_{0.4}Al$. This observation suggests the presence of electron correlation in Heusler compounds being not accounted for by local (spin) density approximation in its current form. Moreover, strong differences in surface and bulk photoemission spectra (excited at photon energies at 700 eV and 3.6 keV, respectively) reveal the loss of the bulk and structure signature within the surface layer. The dispersions of the bands may be studied by spin and angular resolved UPS. This requires however well ordered surfaces of single crystals.

Nevertheless, the difference in bulk and surface properties of $Co_2Cr_{1-x}Fe_xAl$ was

further investigated. XRD as well as EXFAS and ^{57}Fe Mößbauer spectroscopy indicate different structures in bulk and surface for the Heusler compounds $Co_2Cr_{1-x}Fe_xAl$. The bulk is $B2$ ordered, while the surface shows preferred orientation in combination with oxidation. This oxidation seems to be selective on Cr and Al. Thus thin film devices to built magnetic tunnel junctions have to be prepared in ultra high vacuum to ensure the designated structure and thus the predicted spin polarisation.

The seventh chapter introduces the magnetic Heusler compound Co_2CrIn. Its geometrical structure is presented in detail. The magnetic measurements reveal, that Co_2CrIn is a ferrimagnet with a magnetic moment of 1.18 μ_B at 5 K and a soft magnetic behaviour. Co_2CrIn is no half-metallic ferromagnet, which can be derived from measurements of the magnetic moment. The magnetic moment is supposed to be an integer number in case of a half-metallic ferromagnet. Thus the varying properties of the Co_2CrZ compounds still needs further investigation.

In the eighth chapter a rule for predicting half-metallic completely compensated-ferrimagnetic behaviour is presented. This new rule is a combination of two well known rules. The first of these, which is the Slater-Pauling rule, determines the total magnetic moment from the mean number of valence electrons. According to this rule, the half-metallic system of interest must have 24 valence electrons. The Kübler rule, which is the second of these rules, states that Mn in Heusler compounds always carries a high local magnetic moment at the Y site. A combination of these rules results in an easy concept for finding new compounds with half-metallic type behaviour and completely compensated moments. Furthermore, it was found, that even a partial occupation of the Y position by Mn is sufficient to enforce a local magnetic moment on this site. The next step will be the synthesis and characterisation of the above mentioned compounds. The verification of their HMCCF type character by appropriate experiments will follow later.

In summary, this works presents three main aspects in the search of new materials for spintronics: The presentation of some new results regarding the properties of some long known Heusler compounds (Co_2FeSi and $Co_2Cr_{1-x}Fe_xAl$), the characterisation of the new discovered Heusler compound Co_2CrIn and the introduction of a rule to predict half-metallic completely compensated-ferrimagnetic behaviour in Heusler compounds. Nevertheless, there are still some tasks regarding the search for the optimal spin polarised compound to be accomplished.

List of Figures

List of Tables

Bibliography

[1] Fr. Heusler. *Verh. Dtsch. Phys. Ges.*, 12:219, 1903.

[2] J. Kübler, A. R. Williams, and C. B. Sommers. *Phys. Rev. B*, 28:1745, 1983.

[3] R. A. de Groot, F. M. Müller, P. G. van Engen, and K. H. J. Buschow. *Phys. Rev. Lett.*, 50:2024, 1983.

[4] K. E. H. M. Hanssen and P. E. Mijnarends. *Phys. Rev. B*, 34:5009, 1986.

[5] D. Ristoiu, J. P. Nozieres, C. N. Borca, B. Borca, and P. A. Dowben. *Appl. Phys. Lett.*, 76:2349, 2000.

[6] D. Ristoiu, J. P. Nozieres, C. N. Borca, T. Komesu, H.-K. Jeong, and P. A. Dowben. *Eur. Phys. Lett.*, 49:624, 2000.

[7] W. Zhu, B. Sinkovic, E. Vescovo, C. Tanaka, and J. S. Moodera. *Phys. Rev. B*, 64:R060403, 2001.

[8] R. J. Soulen, J. M. Byers, M. S. Osofsky, B. Nadgorny, T. Ambrose, S. F. Cheng, P. R. Broussard, C. T. Tanaka, J. Nowak, J. S. Moodera, and A. Barry. *Science*, 282:85, 1998.

[9] P. J. Webster and K. R. A. Ziebeck. Heusler alloys. In H. P. J. Wijn, editor, *Alloys and Compounds of d-Elements with Main Group Elements. Part 2*, volume 19C of *Landolt-Börnstein - Group III Condensed Matter*, pages 104 – 185. Springer-Verlag, Heidelberg, 1988.

[10] K. R. A. Ziebeck and K.-U. Neumann. Heusler alloys. In H. P. J. Wijn, editor, *Alloys and Compounds of d-Elements with Main Group Elements. Part 2*, volume 32C of *Landolt-Börnstein - Group III Condensed Matter*, pages 64 – 314. Springer-Verlag, Heidelberg, 2001.

[11] S. Ishida, S. Fujii, S. Kashiwagi, and S. Asano. *J. Phys. Soc. Jap.*, 64:2152, 1995.

[12] S. Kämmerer, A. Thomas, A. Hütten, and G. Reiss. *Appl. Phys. Lett.*, 85:79, 2004.

[13] X. Y. Dong, C. Adelmann, J. Q. Xie, C. J. Palmstrom, X. Lou, J. Strand, P. A. Crowell, J.-P. Barnes, and A. K. Petford-Long. *Appl. Phys. Lett.*, 86:102107, 2005.

[14] J. M. D. Coey, M. Venkatesan, and M. A. Bari. Half-Metallic Ferromagnets. In C. Berthier, L. P. Levy, and G. Martinez, editors, *Lecture Notes in Physics*, volume 595, pages 377 – 396. Springer-Verlag, Heidelberg, 2002.

[15] I. Zutic, J. Fabian, and S. Das Sarma. *Rev. Mod. Phys.*, 76:323, 2004.

[16] G. A. Prinz. *Science*, 282:1660, 1998.

[17] M. N. Baibich, J. M. Brote, A. Fert, N. Nyugen Van Dau, F. Petroff, P. Eitenne, G. Creuzet, A. Friederich, and J. Chazelas. *Phys. Rev. Lett.*, 61:2472, 1988.

[18] G. Binasch, P. Grünberg, F. Saurenbach, and W. Zinn. *Phys. Rev. B*, 39:4828, 1989.

[19] J. Pierre, R. V. Skolozdra, J. Tobola, S. Kaprzyk, C. Hordequin, M. A. Kouacou, I. Karla, R. Currat, and E. Lelievre-Berna. *J. All. Comp.*, 262-263:101, 1997.

[20] G. H. Fecher, H.-J. Elmers, G. Schönhense, S. Wurmehl, H. C. Kandpal, and C. Felser. *submitted to Phys. Rev. B*, 2003.

[21] S. Wurmehl, G. H. Fecher, K. Kroth, F. Kronast, H. A. Dürr, Y. Takeda, Y. Saitoh, K. Kobayashi, H.-J. Lin, and G. Schönhense. *J. Phys. D: Appl. Phys.*, 39:803, 2006.

[22] G. H. Fecher, H. C. Kandpal, S. Wurmehl, G. Schönhense, and C. Felser. *J. Appl. Phys.*, 17:7237, 2005.

[23] Y. Miura, K. Nagao, and M. Shirai. *Phys. Rev. B*, 69:144413, 2004.

[24] Y. Miura, K. Nagao, and M. Shirai. *J. Appl. Phys.*, 95:7225, 2004.

[25] R. Y. Umetsu, K. Kobayashi, R. Kainuma, A. Fujita, K. Fukamichi, K. Ishida, and A. Sakuma. *Appl. Phys. Lett.*, 85:2011, 2004.

[26] M. Zhang, A. L. Wolf, L. Zhang, O. Tegus, E. Brück, G. Wu, and F. R. de Boer. *J. Appl. Phys.*, 97:10C301, 2005.

[27] K. H. J. Buschow and P. G. van Engen. *J. Magn. Magn. Mater.*, 25:90, 1981.

[28] C. Felser, B. Heitkamp, F. Kronast, D. Schmitz, S. Cramm, H. Dürr, H.-J. Elmers, G. H. Fecher, S. Wurmehl, T. Block, D. Valdaitsev, A. Nepijko, A. Gloskovskii, G. Jakob, G. Schoenhense, and W. Eberhardt. *J. Phys.: Condens. Matter*, 15:7019, 2003.

[29] T. Block, C. Felser, G. Jakob, J. Ensling, B. Mühling, P. Gütlich, V. Beaumont, F. Studer, and R. J. Cava. *J. Solid State Chem.*, 176:646, 2003.

[30] I. Galanakis. *J. Phys.: Condens. Matter*, 16:3089, 2004.

[31] K. Inomata, S. Okamura, R. Goto, and N. Tezuka. *Jpn. J. Appl. Phys.*, 42:L419, 2003.

[32] K. Inomata, N. Tezuka, S. Okamura, H. Kurebayashi, and A. Hirohata. *J. Appl. Phys.*, 95:7234, 2004.

[33] K. Inomata, S. Okamura, and N. Tezuka. *J. Magn. Magn. Mater.*, 282:269, 2004.

[34] T. Marukame, T. Kasahara, K.-I. Matsuda, T. Uemura, and M. Yamamoto. *IEEE Trans. Magn.*, 41:2603, 2005.

[35] J. C. Slater. *Phys. Rev.*, 49:931, 1936.

[36] L. Pauling. *Phys. Rev.*, 54:899, 1938.

[37] J. Kübler. *Physica*, 127B:257, 1984.

[38] H.-J. Elmers, G. H. Fecher, D. Valdaitsev, S. A. Nepijko, A. Gloskovskii, G. Jakob, G. Schönhense, S. Wurmehl, T. Block, C. Felser, P.-C. Hsu, W.-L. Tsai, and S. Cramm. *Phys. Rev. B*, 67:104412, 2003.

[39] H.-J. Elmers, S. Wurmehl, G. H. Fecher, G. Jakob, C. Felser, and G. Schönhense. *Appl. Phys. A*, 79:557, 2004.

[40] H. J. Elmers, S. Wurmehl, G. H. Fecher, G. Jakob, C. Felser, and G. Schönhense. *J. Magn. Magn. Mater.*, 272-276:758, 2004.

[41] T. Marukame, T. Kasahara, K. Matsuda, T. Uemura, and M. Yamamoto. *Jap. J. Appl. Phys., Part 2:Letters and Express Letters*, 44:L521, 2005.

[42] R. Y. Umetsu, K. Kobayashi, A. Fujita, K. Oikawa, R. Kainuma, K. Ishida, N. Endo, K. Fukamichi, and A. Sakuma. *Phys. Rev. B*, 72:214412, 2005.

[43] K. Kobayashi, R. Y. Umetsu, A. Fujita, K. Oikawa, R. Kainuma, K. Fukamichi, and K. Ishida, 2005.

[44] I. Galanakis. *J. Phys.:Condens. Matter*, 14:6329, 2002.

[45] P. J. Webster. *J. Phys. Chem. Solids*, 32:1221, 1971.

[46] J. Pierre, S. Kaprzyk, and J. Tobola. *Eur. Phys. Jour. B*, 18:247, 2000.

[47] K. H. J. Bushow, P. G. van Engen, and R. Jongebreur. *J. Magn. Magn. Mater.*, 38:1, 1983.

[48] V. Niculescu, T. J. Burch, K. Rai, and J. I. Budnick. *J. Magn. Magn. Mater.*, 5:60, 1977.

[49] K. R. A. Ziebeck and P. J. Webster. *J. Phys. Chem. Solids*, 35:1, 1974.

[50] A. Jezierski. *J. Magn. Magn. Mater.*, 164:381, 1996.

[51] P. J. Brown, K.-U. Neumann, P. J. Webster, and K. R. A. Ziebeck. *J. Phys.: Condens. Matter*, 12:1827, 2000.

[52] A. Yamasaki, S. Imada, R. Arai, H. Utsunomiya, S. Suga, T. Muro, Y. Saito, T. Kanomata, and S. Ishida. *Phys. Rev. B*, 65:104410, 2002.

[53] R. A. de Groot. *Physica*, 172B:45, 1991.

[54] H. van Leuken and R. A. de Groot. *Phys. Rev. Lett.*, 74:7, 1995.

[55] W. E. Pickett. *Phys. Rev. Lett.*, 77:3185, 1996.

[56] A. P. Malozemoff, A. R. Williams, and V. L. Moruzzi. *Phys. Rev. B*, 29:1620, 1984.

[57] H. C. Kandpal. *Thesis*. PhD thesis, Johannes Gutenberg-Universität, Mainz, 2006.

[58] S. Wurmehl, G. H. Fecher, H. C. Kandpal, V. Ksenofontov, C. Felser, H.-J. Lin, and J. Morais. *Phys. Rev. B*, 72:184434, 2005.

[59] S. Wurmehl, G. H. Fecher, H. C. Kandpal, V. Ksenofontov, C. Felser, and H.-J. Lin. *Appl. Phys. Lett.*, 88:032503, 2006.

[60] S. Wurmehl, G. H. Fecher, V. Ksenofontov, F. Casper, U. Stumm, C. Felser, H.-J. Lin, and Y. Hwu. *J. Appl. Phys.*, 99:accepted, 2006.

[61] G. H. Fecher, H. C. Kandpal, S. Wurmehl, C. Felser, and G. Schönhense. *J. Appl. Phys.*, 99:accepted, 2006.

[62] S. Wurmehl, G. H. Fecher, C. Felser, J. Morais, and M. C. M. Alves. *LNLS Annual Report 2004*, 2005.

[63] S. Wurmehl, J. Fecher, G. H.and Morais, M. C. M. Alves, and C. Felser. *Zeitschrift für allgemeine und anorganische Chemie*, 630:1770, 2004.

[64] S. Wurmehl, J. Morais, M. C. M. Alves, S. Teixeira, G. H. Fecher, and C. Felser. *Journal of Alloys and Compounds*, accepted, 2006.

[65] S. Wurmehl, G. H. Fecher, and C. Felser. *Zeitschrift für Naturforschung B*, 61b:accepted, 2006.

[66] H. Akai and P. P. Dederichs. *J. Phys. C*, 18:2455, 1985.

[67] H. Ebert. Fully relativistic band structure calculations for magnetic solids formalism and application. In H. Dreysee, editor, *Electronic Structure and Physical Properties of Solids. The Use of the LMTO Method*, volume 535 of *Lecture Notes in Physics*, pages 191 – 246. Springer-Verlag, Berlin, Heidelberg, 1999.

[68] H. Ebert, J. Minar, and V. Popescu. Magnetic dichroism in electron spectroscopy. In K. Baberschke, M. Donath, and W. Nolting, editors, *Band-Ferromagnetism*, volume 580 of *Lecture Notes in Physics*, pages 371 – 385. Springer-Verlag, Berlin, Heidelberg, 2001.

[69] P. Blaha, K. Schwarz, G. K. H. Madsen, D. Kvasnicka, and J. Luitz. *WIEN2k, An Augmented Plane Wave + Local Orbitals Program for Calculating Crystal Properties*. Karlheinz Schwarz, Techn. Universität Wien, Wien, Austria, 2001.

[70] O. K. Andersen and O. Jepsen. *The Stuttgart Tight-Binding LMTO-ASA program Version 4.7*. Andersen, O. K., Max-Planck-Institut für Festkörperforschung, Stuttgart, Germany, 1998.

[71] V. L. Moruzzi, J. F. Janak, and A. R. Williams. *Calculated Properties of Metals*. Pergamon Press, New York, 1978.

[72] U. v. Barth and L. Hedin. *J. Phys. C: Solid State Phys.*, 5:1629, 1972.

[73] L. Wilk and S. H. Vosko. *Phys. Rev. A*, 15:1839, 1977.

[74] S. H. Vosko, L. Wilk, and M. Nussair. *Can. J. Phys.*, 58:1200, 1980.

[75] S. H. Vosko and L. Wilk. *Phys. Rev. B*, 22:3812, 1980.

[76] J. P. Perdew, J. A. Chevary, S. H. Vosko, K. A. Jackson, M. R. Pederson, D. J. Singh, and C. Fiolhais. *Phys. Rev. B*, 46:6671, 1992.

[77] J. P. Perdev. *Phys. Rev. B*, 33:8822, 1986.

[78] J. P. Perdev and W. Yue. *Phys. Rev. B*, 33:8800, 1986.

[79] P. Mlynarski and D. R. Salahub. *Phys. Rev. B*, 43:1399, 1991.

[80] E. Engel and S. H. Vosko. *Phys. Rev. B*, 47:13164, 1993.

[81] V. I. Anisimov, F. Aryasetiawan, and A. I. Lichtenstein. *J. Phys. Condens. Matter*, 9:767, 1997.

[82] G. E. Bacon and J. S. Plant. *J. Phys. F: Metal Phys.*, 1:524, 1971.

[83] J. Rodrìguez-Carvajal. *Physica B*, 192:55, 1993.

[84] V. Petricek, M. Dusek, and L. Palatinus. *Jana2000, Structure Determination Software Programs*. Petricek, V. and Dusek, M. and Palatinus L., Institute of Physics, Praha, Czech Republic., 2000.

[85] M. Newville, P. Līviņš, Y. Yacoby, J. J. Rehr, and E. A. Stern. *Phys. Rev. B*, 47:14126, 1993.

[86] J. Ravel. *J. Synchrotron Rad.*, 8:314, 2001.

[87] S. I. Zabinsky, J. J. Rehr, A. Ankudinov, R. C. Albers, and M. J. Eller. *Phys. Rev. B*, 52:2995, 1995.

[88] M. Newville. *J. Synchrotron Rad.*, 8:322, 2001.

[89] M. Newville, B. Ravel, D. Haskel, J. J. Rehr, E. A. Stern, and Y. Yacoby. *Physica B*, 208:154, 1995.

[90] K. Lagarec and D. G. Rancourt. *Nucl. Instrum. Meth. Phys. Res. B*, 129:266, 1997.

[91] C. T. Chen. *Nucl. Instrum. Methods Phys. Res. Sect. A*, 256:595, 1987.

[92] C. T. Chen and F. Sette. *Rev. Sci. Instrum.*, 60:1616, 1989.

[93] E. Göring, S. Gold, A. Bayer, and G. Schütz. *J. Synchr.Rad.*, 8:434, 2001.

[94] K. Kobayashi, M. Yabashi, Y. Takata, T. Tokushima, S. Shin, K. Tamasaku, D. Miwa, T. Ishikawa, H. Nohira, T. Hattori, Y. Sugita, O. Nakatsuka, A. Sakai, and S. Zaima. *Appl. Phys. Lett.*, 83:1005, 2003.

[95] Y. Takata, K. Tamasaku, Y. Nishino, D. Miwa, M. Yabashi, E. Ikenaga, K. Horiba, M. Arita, K. Shimada, H. Namatame, H. Nohira, T. Hattori, S. Södergren, B. Wannberg, M. Taniguchi, S. Shin, T. Ishikawa, and K. Kobayashi. *J. Electron Spectrosc. Relat. Phenom.*, 144-147:1063, 2005.

[96] K. H. J. Buschow. Magneto-optical properties of alloys and intermetallic compounds. In E. P. Wolfarth and K. H. J. Buschow, editors, *Handbook of Magnetic Materials*, volume 4, page 493. North-Holland, Amsterdam, London, New York, Tokyo, 1988.

[97] O. Jepsen and O. K. Andersen. *The Stuttgart TB-LMTO-ASA Program version 47*. MPI für Festkörperforschung, Stuttgart, Germany, 2000.

[98] I. Galanakis, P. H. Dederichs, and N. Papanikolaou. *Phys. Rev. B*, 66:174429, 2002.

[99] I. V. Solovyev and M. Imada. *Phys. Rev. B*, 71:045103, 2005.

[100] V. Niculescu, J. I. Budnick, W. A. Hines, K. Rajt, S. Pickart, and S. Skalski. *Phys. Rev. B*, 19:452, 1979.

[101] B. T. Thole, P. Carra, F. Sette, and G. van der Laan. *Phys. Rev. Lett.*, 68:1943, 1992.

[102] P. Carra, B. T. Thole, M. Altarelli, and X. Wang. *Phys. Rev. Lett.*, 70:694, 1993.

[103] B. Balke, G. H. Fecher, H. C. Kandpal, and C. Felser. *submitted to Phys. Rev. B*, 2006.

[104] D. R. Lid, editor. *CRC Handbook of Chemistry and Pysics*. CRC Press, Inc, Boca Raton, Florida, 82th edition, 2001.

[105] R. Kelekar and B. M. Clemens. *J. Appl. Phys.*, 96:540, 2004.

[106] A. Hirohata, M. Kikuchi, N. Tezuka, K. Inomata, J. S. Claydon, and Y. B. Xu. *J. Appl. Phys.*, 97:10C308, 2005.

[107] A. Hirohata, H. Kurebayashi, S. Okamura, M. Kikuchi, T. Masaki, T. Nozaki, N. Tezuka, and K. Inomata. *J. Appl. Phys.*, 97:103714, 2005.

[108] G. Jakob, F. Casper, V. Beaumont, S. Falka, N. Auth, H.-J. Elmers, C. Felser, and H. Adrian. *J. Magn. Magn. Mat.*, 290-291:1104, 2005.

[109] N. Auth, G. Jakob, T. Block, and C. Felser. *Phys. Rev. B*, 024403:68, 2003.

[110] A. Conca, S. Falk, G. Jakob, M. Jourdan, and H. Adrian. *J. Magn. Magn. Mater.*, 290:1127, 2005.

[111] E. Clifford, M. Venkatesan, R. Gunning, and J. M. D. Coey. *Solid State Comm.*, 131:61, 2004.

[112] A. Slebarski, M. Neumann, and B. Schneider. *J. Phys.: Condens. Matter*, 13:5515, 2001.

[113] C. T. Shen, Y. U. Idzerda, H.-J. Lin, N. V. Smith, G. Meigs, E. Chaban, G. H. Ho, E. Pellegrin, and F. Sette. *Phys. Rev. Lett.*, 75:152, 1995.

[114] S. Tanuma, C. J. Powell, and D. R. Penn. *Surf. Interf. Anal.*, 21:165, 1993.

[115] W. Meisel. *Hyperfine Interact.*, 45:73, 1989.

[116] Z. Kajcsos, W. Meisel, P. Griesbach, and P. Gütlich. *Surf. Interface Anal.*, 20:544, 1993.

[117] A. Sekiyama and S. Suga. *J. Electron Spectrosc. Relat. Phenom.*, 137-140:681, 2004.

[118] S. Thiess, C. Kunz, B. C. C. Cowie, T.-L. Lee, M. Reniera, and J. Zegenhagen. *Solid State Comm.*, 132:589, 2004.

[119] K. Kobayashi. *Nucl. Instrum. Methods Phys. Res., Sect. A*, 547:98, 2005.

[120] G. Panaccione, G. Cautero, M. Cautero, A. Fondacaro, M. Grioni, P. Lacovig, G. Monaco, F. Offi, G. Paolicelli, M. Sacchi, N. Stojic, G. Stefani, R. Tommasini, and P. Torelli. *J. Phys.: Condens. Matter*, 17:2671, 2005.

[121] P. Torelli, M. Sacchi, G. Cautero, M. Cautero, B. Krastanov, P. Lacovig, P. Pittana, R. Sergo, R. Tommasini, A. Fondacaro, F. Offi, G. Paolicelli, G. Stefani, M. Grioni, R. Verbeni, G. Monaco, and G. Panaccione. *Rev. Sci. Instrum.*, 76:023909, 2005.

[122] A. Hubert and R. Schäfer. Magnetic domains. page 532. Springer-Verlag, Berlin, Heidelberg, New York, 1998.

[123] C. Felser, H.-J. Elmers, and G. H. Fecher. The properties of $Co_2Cr_{1-x}Fe_xAl$ Heusler compounds. In I. Galanakis and P. Dederichs, editors, *Halfmetallic alloys*, volume 676 of *Lecture Notes in Physics*. Springer-Verlag, Berlin, Heidelberg, 2005.

[124] Ph. Mavropoulos, I. Galanakis, V. Popescu, and P. H. Dederichs. *J. Phys.: Condens. Matter*, 16:S5759, 2004.

[125] Ph. Mavropoulos, K. Sato, R. Zeller, P. H. Dederichs, V. Popescu, and H. Ebert. *Phys. Rev. B*, 69:054424, 2004.

[126] J. C. Slater. *Phys. Rev.*, 49:537, 1936.

[127] O. Eriksson, B. Johansson, and M. S. S. Brooks. *J. Phys.: Condens. Matter*, 1:4005, 1989.

[128] H. Ebert and M. Battocletti. *Solid State Comm.*, 98:785, 1996.

[129] M. A. Tomaz, W. J. Antel, W. L. OBrien, and G. R. Harp. *Phys. Rev. B*, 55:3716, 1997.

[130] C. Theil, J. van Elp, and F. Folkmann. *Phys. Rev. B*, 59:7931, 1999.

[131] C. T. Chen, Y. U. Idzerda, H.-J. Lin, N. V. Smith, G. Meigs, E. Chaban, G. H. Ho, E. Pellegrin, and F. Sette. *Phys. Rev. Lett.*, 75:152, 1995.

[132] J. F. Hochepied, Ph. Sainctavit, and M. P. Pileni. *J. Magn. Magn. Mater.*, 231:315, 2001.

[133] A. Sekiyama, T. Iwasaki, K. Matsuda, Y. Saitoh, Y. Onuki, and S. Suga. *Nature*, 403:396, 2000.

[134] S. Hüfner, S.-H. Yang, B. S. Mun, C. S. Fadley, J. Schäfer, E. Rotenberg, and S. D. Kevan. *Phys. Rev. B*, 61:12582, 2000.

[135] J. H. Wjngaard, C. Haas, and R. A. de Groot. *Phys. Rev. B*, 45:5395, 1992.

[136] W. E. Pickett. *Phys. Rev. B*, 57:10613, 1998.

[137] J. H. Park, S. K. Kwon, and B. I. Min. *Phys. Rev. B*, 65:174401, 2002.

[138] B. I. Min and J. H. Park, M. S.and Park. *J. Phys.: Condens. Matter*, 16:S5509, 2004.

[139] J. H. Park, S. K. Kwon, and B. I. Min. *Phys. Rev. B*, 64:100403, 2001.

[140] J. H. Park and B. I. Min. *Phys. Rev. B*, 71:052405, 2005.

[141] M. A. Kouacou, J. Pierre, and R V Skolozdra. *J. Phys.: Condens. Matter*, 7:7373, 1995.

[142] M. Kato, Y. Nishino, U. Mizutani, and S. Asano. *J. Phys.: Condens. Matter*, 12:1796, 2000.

[143] R. Weht and W. E. Pickett. *Phys. Rev.*, 60:13006, 1999.

[144] I. Galanakis and P. H. Dederichs. Half-metallicity and slater-pauling behaviour. In I. Galanakis and P. Dederichs, editors, *Halfmetallic alloys*, volume 676 of *Lecture Notes in Physics*. Springer-Verlag, Berlin, Heidelberg, 2005.

[145] S. Suga and S. Imada. *J. Electron Spectrosc. Relat. Phenom.*, 92:1 – 9, 1998.

[146] J. D. Browne, N. J. Hance, G. B. Johnston, and C. F. Sampson. *Physica Status Solidi A*, 49:K177, 1978.

[147] H. Okamoto. *Bulletin of alloy phase diagram*, 11:303, 1990.

[148] H.-G. Meissner and K. Schubert. *Zeitschrift für Naturkunde*, 56:523, 1965.

[149] H. Niida, T. Hori, H. Onodera, Y. Yamaguchi, and Y. Nakagawa. *J. Appl. Phys.*, 79:5946, 1996.

[150] H. C. Kandpal, G. H. Fecher, C. Felser, and G. Schönhense. *Phys. Rev. B*, 73:094422, 2006.

[151] C. Pfleiderer, J. Boeuf, and H. von Lohneysen. *Phys. Rev. B*, 65:172404, 2002.

[152] C. Pfleiderer. *Physica B*, 329:1085, 2003.

[153] J. Boeuf, A. Faisst, and C. Pfleiderer. *Acta Physica Polonica B*, 34:395, 2003.

[154] R. E. Rudd and W. E. Pickett. *Phys. Rev. B.*, 57:557, 1998.